Williamson, John Thomas Austin (2022) *APEX (A' Experiment): The search for a dark photon at Jefferson Lab.* PhD thesis.

APEX (A′ Experiment): The Search for a Dark Photon at Jefferson Lab

John Thomas Austin Williamson

Submitted in fulfilment of the requirements for the
Degree of Doctor of Philosophy

School of Physics and Astronomy
College of Science and Engineering
University of Glasgow

March 2022

Abstract

The A′ Experiment (APEX) in Hall A of Jefferson Lab is a search for a new vector gauge boson, A′. The A′, or dark photon, serves as the mediator of a dark sector, a model for dark matter. Kinetic mixing, characterised by the strength parameter ϵ^2, between the A′ and the Standard Model photon would allow for its experimental observation. For APEX the A′ production mechanism is dark bremsstrahlung in interactions of an electron beam with a high-Z target, which would be followed by decay to a lepton pair (the case of a visible dark photon). The High Resolution Spectrometers are set-up to record e^+e^- pairs, from which an invariant mass distribution can be obtained. A resonance search is then performed on this invariant mass spectrum, looking for the A′. A test run for APEX was performed in 2010 with a beam energy of 2.260 GeV, which established limits down to $\epsilon^2 \simeq 1 \times 10^{-6}$ in the mass range 175–250 MeV [1]. This generated wide interest and proved the viability of the experiment.

An APEX production run was carried out in 2019, with a beam energy of 2.138 GeV. This thesis presents the analysis and preliminary results from this 2019 run period. Multiple stages of analysis were conducted in order to obtain a final invariant mass spectrum and to optimise the invariant mass resolution. A blinded peak search was performed on 10% of the final invariant mass distribution, to select background parameters without biasing a full search. The blinded peak search did not find any evidence for the A′ in the mass range 130-220 MeV, and established limits down to $\epsilon^2 \simeq 6 \times 10^{-7}$.

Declaration

The work and content of this thesis are the result of my own research within the Nuclear and Hadron Physics Group at the University of Glasgow. Any exception to this is explicitly referenced or attributed, either in this declaration or in the main body of the thesis as appropriate.

The APEX 2019 production run was carried out by the APEX and Hall A collaborations of Jefferson Lab. I was stationed at Jefferson Lab before and during the experimental run period and contributed to the preparation for the experiment and the collection of data.

As described in section 4.3, the process of calibrating the beam position monitors was performed by Dr Jason Bane (University of Massachusetts Amherst). In section 4.5, the spectrometer magnetic optics optimisation is described. The calibration process was carried out for the Right High Resolution Spectrometer by Sean Jeffas (University of Virginia), whilst the equivalent process for the Left High Resolution Spectrometer was carried out by myself. The method used for calculating the radiative fraction is detailed in section 5.5.1. The MadGraph5 simulation referenced here was set up by Dr Vardan Khachatryan (Cornell University). The peak search code used for the resonance search in chapter 5 was created for the Heavy Photon Search experiment at Jefferson Lab [2].

No part of this work has been submitted for any other qualification at the University of Glasgow or elsewhere.

Acknowledgements

Over the course of my PhD I have received guidance and help from numerous sources. My supervisors, David Hamilton and Rachel Montgomery, have given me support throughout with their experience of Jefferson Lab analyses. As well as providing valuable feedback for reports, talks and of course this thesis.

The experimental run of APEX was a collaborative effort. The Hall A staff scientists and lab technicians provided needed support during the run period. Members of the Hall A collaboration, particularly graduate students working on the 'Tritium' set of experiments that proceeded APEX in the hall, were helpful in explaining the various Hall A and HRS systems and corresponding standard analysis techniques. APEX itself would not be possible without the previous work performed for APEX proposals and the test run in 2010. Sean Jeffas helped with the HRS optics optimisation, working on the RHRS in parallel with my own efforts on the LHRS. Cameron Bravo, of the HPS collaboration, gave guidance and support for the use of the HPS peak search code.

The wider Nuclear and Hadron Physics Group at Glasgow also provided assistance from use of farm and computing resources to knowledge and experience from a broader range of experimental analyses. The welcoming atmosphere of the group as a whole made the process of completing a PhD more bearable. Particularly the PhD students who were always willing to answer my many silly questions, and share a crowd wisdom in general analysis. Beyond this, trips to the pub and elsewhere with fellow PhD students in the group gave much needed relief from analysis or writing work. When based at Jefferson Lab, regular bowling and pub quizzes with Stuart Fegan (previously a member of the group) and other postdocs at the lab served a similar function.

Finally, I would like to thank my friends, family and especially my girlfriend for all of the support throughout the years. May they never hear of dark photons again.

Contents

Chapter 1

Introduction

The Standard Model (SM), developed the during twentieth century, remains the established framework for describing visible matter and its interactions (excluding gravity). It has provided many successful predictions for the existence of particles as well as having precise agreement with experimental results. The W, Z gauge bosons, gluons, top quark and Higgs boson were all theorised by the Standard Model and have since been experimentally discovered. Precise agreement with experimental measurements, such as the running of the electromagnetic fine structure constant, α, [3,4] and the electron magnetic moment [5], has also been confirmed. The model, however, faces several challenges including the existence of 'dark matter'.

Dark matter was first hypothesised in 1931, based on observations of the velocity dispersion of the Comma cluster. The velocity dispersion of the cluster was calculated using the virial theorem with the mass of the galaxy cluster estimated based on the number of observable galaxies and an assumed average galaxy mass. The calculated value of 80 kms^{-1} was compared to the observed velocity dispersion of 1000 kms^{-1} [6]. One explanation offered for this discrepancy was the presence of unobserved 'dark matter', which would make up the majority of the mass of the cluster. Since then, the existence of dark matter has become well-established, with evidence from observations from a wide range of sources and cosmological scales.

The rotational curve of galaxies, plots of the rotational velocities of visible objects in a galaxy versus the radial distance from the galactic centre, are one source of observations supporting the presence of dark matter. These are usually calculated from observations of the Doppler shift of the well-known 21 cm spectral line from hydrogen. Simple Newtonian dynamics can derive an expression for the rotational velocities, $v(r)$, as a function of radial distance: $v(r) = \sqrt{GM(r)/r}$. Where G is is the gravitational constant, r the radial distance and $M(r)$ the mass as a function of radial distance. From the visible matter observed in galaxies this relationship should lead to a $1/\sqrt{r}$ drop-off in orbital velocities, moving outward from the galactic centre beyond the optical disc. Instead, as illustrated in figure 1.1, the rotational curves of galaxies were found to have a flat component as the radius increased (including the Milky Way [7]). This can be explained by the presence of a dark matter halo, with $M(r) \propto r$.

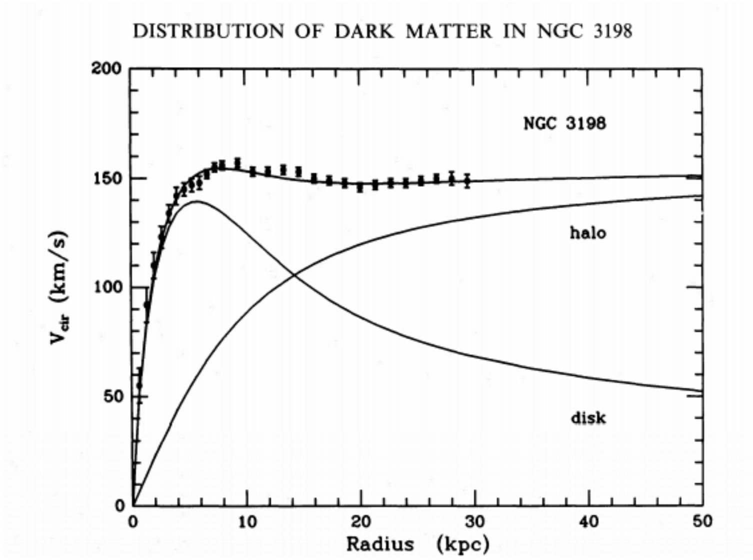

Figure 1.1: Rotation curve for galaxy NGC 3198, showing the orbital speed of observed matter as a function of radial distance from the galaxy centre. The observation data is fitted with a model containing SM matter (disk) and dark matter (halo) contributions that are labelled. The halo contribution is needed in order to explain the observed behaviour of the orbital velocity as a function of radial distance. Figure taken from [8].

Gravitational lensing provides another source of observational evidence for dark matter. The deflection of light by the presence of mass can be used to map the distribution and density of mass, which can then be contrasted with mapping of visible matter from EM (Electromagnetic) sources. The stellar, plasma and dark matter components in a cluster typically follow a similar spatial distribution, following from the gravitational potential of the system. During the mergers of clusters, however, galaxies and dark matter can become spatially decoupled from the intracluster plasma due to 'ram pressure stipping'. Ram pressure, P_r, is a drag force experienced by objects moving through the intracluster plasma and for a galaxy is given as $P_r \approx \rho_e v_{gal}^2$, where ρ_e is the density of the intracluster plasma and v_{gal} is the speed of the galaxy relative to the plasma [9]. Ram pressure stripping occurs when the ram pressure is greater than the gravitational force binding the intracluster plasma: $P_r > F_{g,IP}$. One observation of the decoupling of galaxies and dark matter from the intracluster plasma comes from the Bullet cluster (1E 0657-56), consisting of two colliding galaxy clusters. The mapping of x-ray emissions from the Chandra observatory [10, 11] (emanating from the plasma: hot gas which forms the majority of baryonic matter in the system) was compared to that from gravitational lensing [12]. This can be seen in figure 1.2, where the x-ray image is displayed in pink showing the distribution of the hot, x-ray emitting gas and is clearly separated from the mass distribution as derived from gravitational lensing shown in blue (there is a spatial offset of 8 σ between the total centre of mass and visible baryonic centre of mass [12]). This separation of mass from visible and gravitational lensing observations represents strong observational evidence for dark matter.

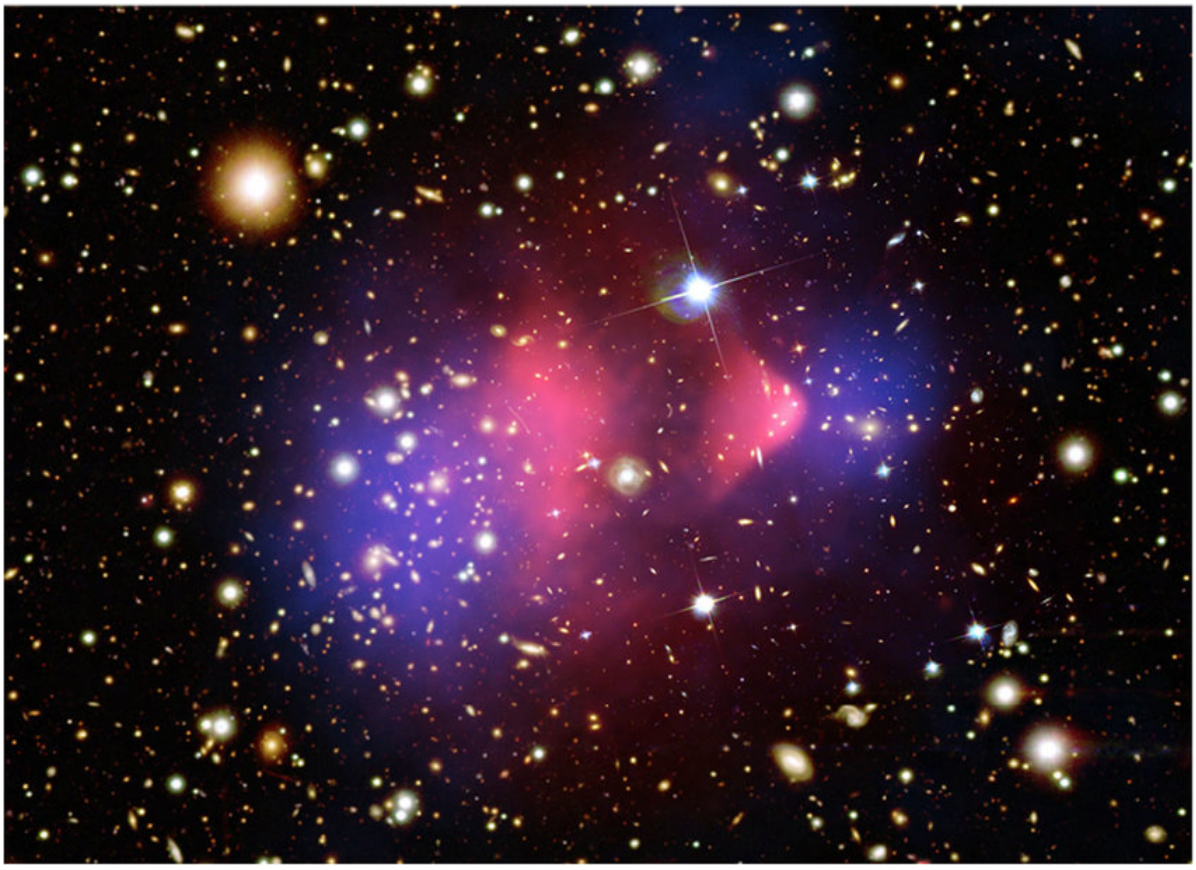

Figure 1.2: Composite image of the Bullet (1E 0657-56), formed from the collision of two galaxy clusters. The Blue region represent the mass distribution from gravitational lensing and the pink region represents the mass distribution from x-ray observations. They are overlayed on an optical image from Magellan and the Hubble Space Telescope, which displays galaxies in white and orange. Figure taken from [13].
Credit:
X-ray: NASA/CXC/CfA/M.Markevitch et al.;
Optical: NASA/STScI; Magellan/U.Arizona/D.Clowe et al.;
Lensing Map: NASA/STScI; ESO WFI; Magellan/U.Arizona/D.Clowe et al.

Evidence for dark matter can also be seen in the Cosmic Microwave Background (CMB), the remnant radiation from the early, hot phase of the universe. The CMB is known to be isotropic to the level of 10^{-5}, and the analysis of CMB anisotropies is used to test cosmological models and constrain parameters. Analysis of the CMB power spectrum, obtained from cosmological surveys from satellite observatories WMAP [14] and Plank [15], can be used to estimate the proportion of SM and dark matter in the universe. A combined analysis, also including data from baryon acoustic oscillations, results in a matter composition of the universe of $\sim$85% dark matter, $\sim$15% SM matter [16].

The existing evidence for dark matter can all be explained by the concordance model of cosmology, the Lambda Cold Dark Matter (λCDM) model. This model proposes that the energy density of the universe is comprised of 4% SM particles, 22% ‘cold’ dark matter and 74% dark energy. This model does not require any interaction between dark matter and SM particles beyond gravity to exist, though proposed interactions could help explain the ‘relic’ abundance of dark matter observed today. In ’freeze-out’ models, during the period of the extremely hot and dense early universe, dark matter particles would annihilate and create SM particles and vice versa. As the thermal energy of SM particles decreased it became insufficient to create DM particles, while DM annihilation continued. The density of dark matter eventually decreased until the probability for annihilation became relatively small and the density would ‘freeze-out’ [17]. If the dark matter particles interacted via the electro-weak force and had masses on the scale of 10 GeV to 10 TeV, the resulting relic abundance of dark matter would match the observed value. This is known as the ’WIMP miracle’ (where WIMP is Weakly Interacting Massive Particle). The correct relic abundance can be reproduced by an alternative theory: that of a ’dark’ or ’hidden’ sector that interacts with SM matter through a new force with a gauge boson of mass 50 MeV - 1 GeV.

Many different theories have been proposed to account for the observed existence of dark matter. One proposal is the existence of a dark sector of particles which are not charged directly under the SM. The particles in this dark sector must interact gravitationally with SM matter (if they are to serve as a dark matter candidate) and are theorised to potentially also interact with SM matter through different forms of ‘portal’ interactions. The nature of the portal is dependent on the spin and parity of the mediators in the dark sector [18]. If the mediator of the dark sector is a vector boson, then the portal is described as a ‘vector portal’. An additional U(1) symmetry was first proposed in 1981 [19], and is a common feature of extensions to the Standard Model with a range of motivations. The gauge boson of this addition U(1) symmetry is denoted as a 'dark photon', 'hidden photon' or A' (amongst other names). The A' would 'kinetically mix' with the SM photon and couple to the electromagnetic current of the SM. The effective gauge coupling of the A' to electric charge is suppressed by a dimensionless coupling constant ϵ, the kinetic mixing parameter. This additional U(1) symmetry is a possible representation of a dark sector with a vector gauge boson, the A', which kinetically mixes with SM matter.

The primary motivation for searching for the A' is as the vector portal to the dark sector, which is a compelling model for dark matter. This supports exploring as wide a parameter space, $P(m_{A'}, \epsilon^2)$ in $m_{A'}$ and ϵ^2 , that is possible through experiment. Certain values of ϵ can be further motivated through theory (as discussed in chapter 2), though previous motivations as explanations of other SM anomalies have been mainly ruled out. The size of the parameter space enables a range of experiment types, and production mechanisms, to form complementary searches for the A'.

APEX is based in experimental Hall A of Jefferson Lab. The electron beam of the facility was used with a stationary, high-Z target. The production mechanism for dark photons is through 'dark bremsstrahlung', analogous to EM bremsstrahlung. The final state is e^+e^- (through the decay of the dark photon), which is recorded by the High Resolution Spectrometers (HRSs) in Hall A. A successful test tun was carried out in 2010 with a single Tantalum target, setting in limits down to $\epsilon^2 \simeq 1 \times 10^{-6}$ in a mass range of 175 MeV $< m_{A'} <$ 250 MeV [1]. A segmented tungsten target was used for the 2019 run. Chapter 3 describes in detail the experimental apparatus used for APEX: electron beam, target, detectors and DAQ. The analysis of the collected data involved several stages: calibration of the various detectors systems, optimisation of the timing analysis, Particle Identification (PID) and spectrometer optics as well modification of the tracking algorithms. This was necessary to optimise the invariant mass resolution achieved and minimise the portion of background events. This stage of the analysis is described in chapter 4. Ultimately the A' is searched for as a peak in the invariant mass spectrum obtained from e^+e^- pairs. Careful consideration has to be given to the method used to model the background in the invariant mass spectrum and to how the test statistics for discovery and exclusion are formed in order to maximise the sensitivity of the measurement. This process and the results of a blinded resonance search (performed on 10% of the obtained data), are described in chapter 5. Finally, preliminary conclusions and future steps for the analysis are discussed in chapter 6.

Chapter 2

Motivation

APEX searched for a dark photon, the proposed mediator of a dark sector and vector portal between SM and dark sectors. The theoretical basis for such an extension to the Standard Model, an additional U(1) symmetry, is considered: how this results in kinetic mixing between the A' and SM photon which allows for the observation of the A'. The properties and production mechanisms for the A' are examined focusing on APEX but also in conjunction with an overview of dark photon searches which places APEX in the wider context of the field. The kinematics of fixed target A' experiments, along with the QED backgrounds present, are detailed to motivate the experimental set-up used for APEX.

2.1 Background Theory

Among several dark-matter candidates and theories is the presence of a 'dark' or 'hidden' sector. This sector, which does not interact with the SM strong or electroweak forces, need only posses one single additional U(1) symmetry. The resulting 'dark force' would be mediated by a vector boson, the A' or dark photon. The A' is capable of kinetic mixing with the SM photon [19], coupling to SM matter through a 'vector portal'. There are frameworks for a dark sector with different mediators which define different portal interactions: a 'Higgs portal' for a scalar mediator, an 'axion portal' for a pseduoscalar mediator and a 'neutrino portal' for a fermion mediator [18]. The vector portal, A', was the case that APEX searched for.

A simple model of the dark sector with an additional U(1) symmetry and vector portal to SM matter can be described as an addition to the SM Lagrangian:

$$\mathcal{L} = \mathcal{L}_{SM} + \epsilon_Y F^{Y,\mu\nu} F'_{\mu\nu} + \frac{1}{4} F'^{\mu\nu} F'_{\mu\nu} + m^2_{A'} A'^{\mu} A'_{\mu}, \tag{2.1}$$

where $\mathcal{L}_{SM}$ is the Standard Model Lagrangian, $F'_{\mu\nu} = \partial_\mu A'_\nu - \partial_\nu A'_\mu$ is the field strength tensor related to the dark photon field, A'^μ, $F^Y_{\mu\nu} = \partial_\mu A_\nu - \partial_\nu A_\mu$ is the equivalent for the SM electromagnetic field and $m_{A'}$ is the mass of the dark photon [20]. The second term in equation 2.1 represents kinetic mixing. For low-energy interactions kinetic mixing is equivalent to a redefinition of A^μ [21]:

$$A^\mu \to A^\mu + \epsilon A'^\mu. \tag{2.2}$$

This generates a coupling of the dark photon, A′, to electrically charged particles with $\epsilon e A'_\mu J^\mu_{EM}$, where $\epsilon \equiv \epsilon_Y \cos(\theta_W)$ is the dimensionless kinetic mixing parameter and θ_W is the weak mixing angle [20]. In other words, SM particles with an EM charge of q_i acquire a coupling of $\epsilon e q_i$ to the dark photon. The kinetic mixing parameter can also be expressed as a ratio of the dark photon field and electromagnetic fine structure constants: $\epsilon^2 = \frac{\alpha'}{\alpha}$. Two parameters, ϵ and $m_{A'}$, thus characterise the dark photon and the parameter space in which it is searched for.

Kinetic mixing is illustrated in figure 2.1. If there exists heavy multiplets, χ, that couples to both the SM γ and the A′ then one loop level interactions between γ and A′ can occur. This results in values of $\epsilon \sim 10^{-3} - 10^{-2}$ or $(\frac{\alpha'}{\alpha} \sim 10^{-6} - 10^{-4})$ [22]. Additional loop processes, motivated by certain grand unified theories of physics, suppress the kinetic mixing of γ and A′ described by equation 2.1 resulting in values of $\epsilon \sim 10^{-5} - 10^{-3}$ or $(\frac{\alpha'}{\alpha} \sim 10^{-8} - 10^{-6})$ [22]. Smaller values of ϵ, down to $\epsilon \sim 10^{-12}$ can be motivated from String theory models [23,24].

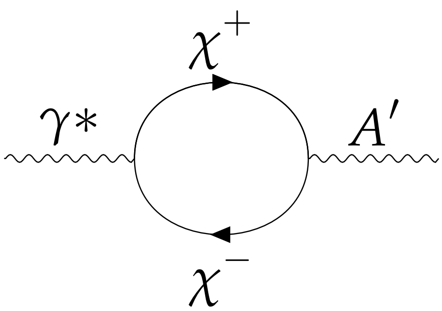

Figure 2.1: kinetic mixing of SM photon with A′ at one loop level, where χ is a massive particle that possesses EM and dark charge.

For experimental searches consideration has to be given to the nature of the A′ decay. If the dark photon has a large enough mass to decay into lepton pairs ($m_{A'} > 2m_l$)

then its partial decay width is given by [25]:

$$\Gamma_{A'\to l^+l^-} = \frac{1}{3}\alpha\epsilon^2 m_{A'}\sqrt{1-\frac{4m_l^2}{m_{A'}^2}}\left(1+\frac{2m_l^2}{m_{A'}^2}\right). \tag{2.3}$$

Equivalently if the A′ mass is large enough to decay into hadrons ($m_{A'} > 2m_h$), the partial decay width is given by [26]:

$$\Gamma_{A'\to \mathrm{hadrons}} = \frac{1}{3}\alpha\epsilon^2 m_{A'}\sqrt{1-\frac{4m_\mu^2}{m_{A'}^2}}\left(1+\frac{2m_\mu^2}{m_{A'}^2}\right)\frac{\sigma(e^+e^-\to \mathrm{hadrons})}{\sigma(e^+e^-\to\mu^+\mu^-)}(E=m_{A'}). \tag{2.4}$$

From equation 2.3 (and also equation 2.4, though the ($m_{A'} > 2m_h$) regime is not relevant for APEX) it can be seen that the partial decay width is proportional to ϵ^2. At the low values of ϵ^2 probed by APEX this means that the A′ should appear as a sharp resonance in an invariant mass spectrum, with the width defined by experimental resolution. The branching ratios ($BR_{A'}$) of the A′ follow from the decay widths and are illustrated in figure 2.2.

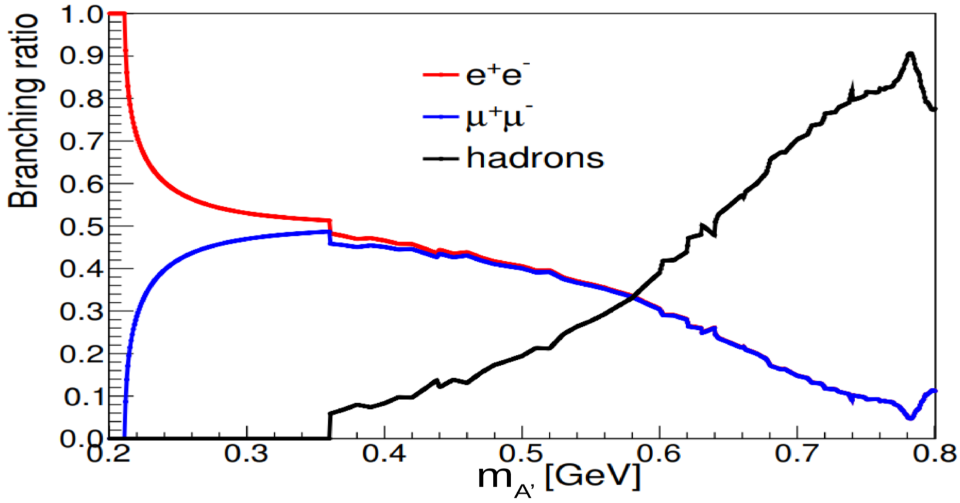

Figure 2.2: Branching ratios for A′ versus $m_{A'}$, for masses of up to ~ 0.8 GeV. From [27] (with only x-axis label altered).

For APEX the experimental signature searched for is e^+e^-, resulting from the prompt decay of an A′. The proper lifetime of the A′ is related to the decay width:

$$c\tau = \frac{1}{\Gamma} \simeq \frac{3}{N_{eff}\alpha\epsilon^2 m_{A'}}. \tag{2.5}$$

This is a re-expression of equations 2.3 and 2.4, where N_{eff} is the number of decay channels and is equal to:

$$N_{eff} = \begin{cases} 1 & m_{A'} \lesssim 2m_{\mu}, \\ 2 + R(m_{A'}) & m_{A'} \geq 2m_{\mu}. \end{cases} \tag{2.6}$$

$R(m_{A'})$ is the ratio $\frac{\sigma(e^+e^- \to \text{hadrons})}{\sigma(e^+e^- \to \mu^+\mu^-)}$ which is energy dependent [28]. For APEX the relationship between the proper lifetime and the vertex displacement can be expressed as [20]:

$$l_0 \equiv \gamma c \tau \simeq \frac{0.8\text{cm}}{N_{eff}} \left(\frac{E_0}{10\text{GeV}}\right) \left(\frac{10^{-4}}{\epsilon}\right)^2 \left(\frac{100\text{MeV}}{m_{A'}}\right)^2, \tag{2.7}$$

where E_0 is the beam energy. For the range of ϵ probed for APEX, the path length is negligible and the decay of A′ considered prompt. In this context looking for a peak in the invariant mass spectrum from e^+e^- is an appropriate search strategy, and was used for APEX. In contrast some experiments probe smaller values of ϵ by looking for 'detached' vertices where l_0 must be accounted for.

APEX looks for the case of 'visible' dark photons, where the dark photons decay into visible, SM products. It is possible for the dark sector to contain states with mass, m_χ, such that $2m_\chi < m_{A'}$ and the dark photon can decay into 'invisible' dark matter states. If the decay is exclusively into dark matter states then the A′ is an 'invisible' dark photon, and if the decay features both SM and dark matter it is labelled as a 'partially visible' dark photon.

2.2 Dark Photon Searches

Ultimately each dark photon search probes a parameter space, $P(m_{A'}, \epsilon^2)$, determined by various aspects of the experiment. Broad categories of A′ searches can be made according to the production mechanism, the experimental facility and the detection signature, which all affect the parameter space searched.

The common detection signatures are:

- An invariant mass resonance from the decay products (AKA a 'bump hunt'), as is the case for APEX. This is done for the case of prompt, visible A′ decays.
- Displaced vertices. This can be used to probe smaller values of ϵ, for the case where the A′ has an appreciable lifetime.

- Missing Mass. This is used in the case of invisible, or partially visible, dark photons.

For APEX the proposed production mechanism is through 'dark bremsstrahlung' ($e^-Z \to e^-ZA'$), which is described in more detail in section 2.3. Other common production mechanisms are e^+e^- annihilation ($e^+e^- \to \gamma A'$), Drell-Yan ($q\bar{q} \to \gamma A'$) and meson decay (e.g. $\pi^0 \to \gamma A'$).

The different production mechanisms and detection signatures motivate the different categories of experimental facilities that are used for A' searches. A small overview is given here, though this is not exhaustive. The main categories of experimental facilities are thin fixed target experiments, colliders and beam dumps.

2.2.1 Thin Fixed Target Experiments

An electron beam used with a fixed target will generate dark photons through the dark bremsstrahlung mechanism. APEX is a prime example of this categorisation. The A1 spectrometer at the Mainz Microtron was used for a search with an electron beam based on dark bremsstrahlung with decay to e^+e^- [29]. The HPS (Heavy Photon Search) experiment in Hall B of JLab uses an electron beam and fixed target and searches for a resonance in the e^+e^- mass spectrum and displaced vertices [30], both from a dark bremsstrahlung mechanism. Planned searches with an electron beam and fixed target are Darklight at JLab [31] and MAGIX at MESA (Mainz) [32]. Proton beams can also be used with a fixed target. The HADES experiment at GSI used a proton beam with stationary hydrogen and niobium targets, to measure e^+e^- final states from meson decays [33]. The NA48/2 experiment at SPS (CERN) used a proton beam with a stationary beryllium target [34]. The Kaons produced would then decay to pions which decay to produce an e^+e^- invariant mass spectrum (meson decay mechanism, $K^\pm \to \pi^\pm\pi^0; \pi \to A'$). Positron beams can be used with fixed targets through the e^+e^- annihilation mechanism. These are missing mass measurements of dark photons with monophoton final states: $e^+e^- \to \gamma A' \to \gamma, \chi\chi*$. VEPP-3 at the Budker Institute at Novosibirsk [35] and PADME at INFN Frascati [36] are proposed measurements of this kind.

2.2.2 Collider Experiments

Dark photon searches at colliders are possible through meson decay, e^+e^- annihilation and Drell-Yan production modes. Collider searches are often complementary to those of fixed target experiments. Generally fixed target experiments can achieve higher luminosities and thus reach lower values of ϵ, while collider experiments can reach higher energies and thus larger values of $m_{A'}$. Several searches have taken place at e^+e^- colliders: KLOE, KLOE-II, BaBar and Belle-II. KLOE and KLOE-II at DAΦNE performed resonance searches on e^+e^- and $\mu^+\mu^-$ produced by ϕ meson and dipion decays [37,38]. BaBar at SLAC, performed a resonance search on a $\mu^+\mu^-$ mass spectrum using the production mechanism $\Upsilon \to \gamma A'; A' \to \mu^+\mu^-$, and also looked at invisible decays [39]. Belle-II looks at invisible decays, and is expected to improve on the equivalent result from BaBar [40,41]. Proton collision experiments at the LHC (CERN) can perform searches through meson decays and reach high energies, and thus high $m_{A'}$. Above the dimuon threshold, $m_{A'} > 2m_\mu$ the LHCb experiment search for both prompt decays $A' \to \mu^+\mu^-$ and displaced vertices with $\eta \to \gamma A'; A' \to \mu^+\mu^-$. Below this threshold LHCb looks for prompt decays via: $D* \to D^0 A'$ [42–45]. ATLAS and CMS at the LHC have also performed dark photon searches [46,47]. The PHENIX experiment at RHIC (Brookhaven) used proton collisions and deuterium - gold nuclei (d+Au) collisions in dark photon searches. Both interactions produce neutral mesons which promptly decay into dark photons ($\pi^0, \eta \to \gamma e^+e^-$) [48].

2.2.3 Beam Dump Experiments

Electron or proton beam dumps are a natural place to look for dark photons with small ϵ as this will correspond to greater vertex displacement (as in equation 2.7). In this scenario long-lived A's will traverse the beam dump (designed to absorb SM particles) and be detected downstream of the dump (after decaying). Typically beam dump experiments have high luminosities, carried out with high beam intensities and thick targets. At electron beam facilities previous experiments that were carried out and interpreted as searches for Higgs-like or axion-like particles were reinterpreted as dark photon searches: E774 at FermiLab [49], E137 and E141 at SLAC [50] and an experiment at Orsay [51]. The NA64 experiment (CERN), performed a missing energy search with an electron beam and electromagnetic calorimeter as an 'active dump' [52]. Several experiments are planned for proton beam dumps including: COHERENT at Oak Ridge [53], SHiP at CERN [54] and SeaQuest at FermiLab [55].

2.3 A′ fixed target kinematics

For the motivation, design and analysis of APEX the kinematics of A′ production with a fixed target and electron beam were considered. In fixed target experiments dark photons can be produced from a process analogous to ordinary, EM bremsstrahlung as shown in figure 2.3 (so-called dark bremsstrahlung). The A′ then decays into a lepton pair which provides the experimental signature. The cross-section for A′ production for an electron beam scattering on a fixed, high-Z target (such as tungsten for the 2019 run or tantalum for 2010 test run [1]) can be approximated as [22]:

$$\sigma_{A'} \sim 100\text{pb}\left(\frac{\epsilon}{10^{-4}}\right)^2\left(\frac{100\text{MeV}}{m_{A'}}\right)^2.$$

This cross-section is larger than the equivalent in colliding hadron and e^+e^- beam experiments by several orders of magnitude [56].

The kinematics of this interaction can be estimated using the Weizsäcker-Williams approximation [20,57–59] (modelling the target nucleus as an effective photon flux in the rest frame of the electron). The Weizsäcker-Williams effective photon flux, χ, is given as:

$$\chi \equiv \int_{t_{min}}^{t_{max}} dt \frac{t - t_{min}}{t^2} G_2(t), \tag{2.8}$$

where $t \equiv -q^2$ ($q = P_i - P_f$, where Pi and P_f are the initial and final four-momenta of the nucleus) and $G_2(t)$ is the general electric form factor [60].

For an electron with energy E_0, the differential cross-section for A′ production, with mass $m_{A'}$ and Energy $E_{A'} \equiv xE_0$ (where $0 < x < 1$) at angle $\theta_{A'}$ (defined in lab frame between incoming electron and outgoing A') can be approximated as [20,61]:

$$\frac{d\sigma}{dx d\cos(\theta_{A'})} \approx \frac{8Z^3\alpha^3\epsilon^2E_0^2x}{U^2}\tilde{\chi}\left[(1 - x + \frac{x^2}{2}) - \frac{x(1-x)m_{A'}^2(E_0^2x\theta_{A'}^2)}{U^2}\right]. \tag{2.9}$$

$\tilde{\chi} \equiv \frac{\chi}{Z^2}$ (0.1 - 10 in the APEX region of interest) is the reduced Weizsäcker-Williams effective photon flux which is dependent on $m_{A'}$, E_0 and the target nucleus [61], Z is the atomic number of the target and U is the virtuality of the intermediate electron in initial-state bremsstrahlung:

$$U(x,\theta_{A'}) = E_0^2 x \theta_{A'}^2 + \frac{(1-x)}{x} m_{A'}^2 + m_e^2 x, \tag{2.10}$$

where m_e is the electron mass. This approximation (equation 2.9) is valid for the case that $m_e \ll m_{A'} \ll E_0$ and $x\theta_{A'}^2 \ll 1$.

The assumption that $m_e \ll m_{A'}$ can be used to drop the term related to m_e in equation 2.10, and the angular integration of equation 2.9 thus yields:

$$\frac{d\sigma}{dx} \approx \frac{8Z^3\alpha^3\epsilon^2 x}{m_{A'}^2}\left(1 + \frac{x^2}{3(1-x)}\right)\tilde{\chi}. \tag{2.11}$$

From these cross-sections, several differences in the kinematics and rates of A′ production and Standard Model EM bremsstrahlung can be gleaned:

- A' production peaks at $x \sim 1$, which minimises $U(x,0)$, such that $E_{A'} \approx E_0$: the A' takes almost all of the beam energy.
- From equation 2.11 it can be seen that the production rate for A′ is proportional to $(\alpha^2\epsilon^2)/m_{A'}^2$ and that the production rate is thus suppressed by a factor of $\sim \epsilon(m_e^2/m_{A'}^2)$ compared to ordinary photon bremsstrahlung.
- Equation 2.9 shows that the emission of A′ is dominated at small angles where $U(x,\theta_{A'}) \lesssim 2U(x,0)$ after which emission falls off as $1/\theta_{A'}^4$. Near the median value of x the cutoff angle for A' emission is

  $$\theta_{A',max} \sim \max\left(\frac{\sqrt{m_{A'}m_{e^-}}}{E_0}, \frac{m_{A'}^{3/2}}{E_0^{3/2}}\right), \tag{2.12}$$

  which is parametrically smaller than the opening angle of the A' decay products ($\sim m_{A'}/E_0$). It can thus be approximated that the A′ is emitted in the beam (initial electron) direction.

These differences between A′ production and Standard Model EM bremsstrahlung were utilised in the design of the experiment. This is described in the following section, after close consideration of the main QED backgrounds present for APEX.

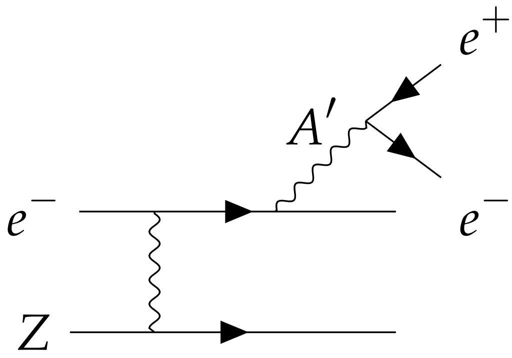

Figure 2.3: 'Dark bremsstrahlung': an incoming electron interacts with a target nucleus, with atomic number Z, to produce an A' from a process analogous to EM bremsstrahlung, which then decays to a lepton pair.

2.4 QED Background

The primary backgrounds in the e^+e^- invariant mass spectrum for APEX are Bethe-Heitler tridents, radiative tridents and e^+e^- pair photoproduction. The 'trident' processes are labelled as such because of the three-lepton final state: $e^-Z \to e^+e^-e^-Z$. Both have the same final state particles as A' production, of which the e^+e^- are detected by the experiment. The third background, e^+e^- pair photoproduction, comes from the interactions of the electron beam with the tungsten target. As the electron beam passes through the multiple target foils (described in section 3.7) photons are produced through bremsstrahlung and these photons then interact with the target to pair produce e^+e^-. The pair produced e^+e^- can then be recorded in detectors, giving the correct experimental signature. The trident backgrounds and e^+e^- photoproduction are considered separately.

Understanding the kinematics of trident reactions and their relation to A' production is key in the design of fixed-target experiments in search of dark photons. Diagrams of these reactions are shown in figure 2.4. For the Bethe-Heitler reaction both virtual photons are space-like, whereas for radiative tridents one virtual photon is time-like, the other space-like.

For radiative trident reactions the same kinematics govern the behaviour as for A' production for a small window around the invariant mass of the A'. The relative cross-sections of A' production and radiative trident reactions can be shown to be [20]:

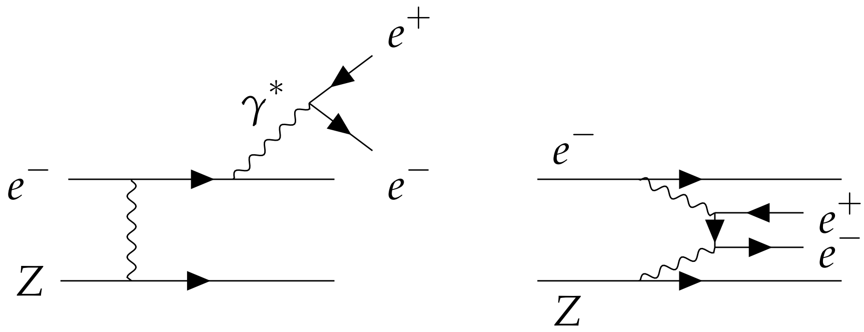

Figure 2.4: Feynman diagrams for trident reactions.
Left: Radiative trident reaction, Right: Bethe-Heitler trident reaction [22].

$$\frac{d\sigma(A')}{d\sigma(\gamma^*_{rad})} = \left(\frac{3\pi\epsilon^2}{2N_{eff}\alpha}\right)\left(\frac{m_{A'}}{\delta m}\right), \tag{2.13}$$

where $\sigma(A')$ is shorthand for $\sigma(e^-Z \to e^-Z(A' \to l^+l^-))$ the cross-section for A′ production, $\sigma(\gamma^*_{rad})$ is shorthand for $\sigma(e^-Z \to e^-Z(\gamma^* \to l^+l^-))$ the radiative trident cross-section and δm is the width of the invariant mass window (around $m_{A'}$). MC (Monte Carlo) simulations of both the A′ production and radiative trident processes were used to check the accuracy of equation 2.13 which was found to have almost perfect agreement with the MC results [20]. This means that radiative trident processes can be utilised in the consideration and analysis of A′ production: both the overall production rate and the sensitivity of an experiment to A' signals. The result from a peak search will establish upper limits in terms of the number of signal events, μ_{up} (as described in chapter 5). If the only background observed was from radiative tridents then equation 2.13 could be used to translate from an upper signal limit into a limit on ϵ^2, the desired final result. The background measured, however, will include other sources. For APEX the dominant contributions were from Bethe-Heitler and radiative tridents, e^+e^- photoproduction and accidental coincidence events (described in detail in section 5.5). To establish an upper limit in ϵ^2 the radiative fraction, a scaling factor labelled 'f', is used to translate from measured background to radiative tridents:

$$f(m) = \frac{\text{Number of radiative trident events}}{\text{Total events in mass spectrum}}. \tag{2.14}$$

The radiative fraction is labelled as '$f(m)$' here, as it varies with the invariant mass.

The upper limit in ϵ^2 can then be calculated as:

$$\epsilon^2 = \frac{1}{f}\frac{d\sigma(A')}{d\sigma(\gamma^*_{rad})}\left(\frac{\delta m}{m_{A'}}\right)\left(\frac{2N_{eff}\alpha}{3\pi}\right). \tag{2.15}$$

This motivates the importance of understanding and reducing the various sources of background as this directly affects the final exclusion zone in $P(m_{A'}, \epsilon^2)$ obtained by the measurement.

Bethe-Heitler trident processes, in contrast to radiative tridents, have significantly different kinematics compared to A′ production. The total cross-section for Bethe-Heitler processes is far larger than for A′ production and radiative processes but the difference in kinematics can be exploited to maximise the rate of A′ production compared to Bethe-Heitler background. For A′ production the kinematics result in a highly-boosted e^+e^- pair with the soft, recoiling electron scattering at a large angle. For Bethe-Heitler, in contrast, the process is unenhanced at greater pair energies. Bethe-Heitler also favours an asymmetric lepton pair where one lepton carries the majority of the pair's energy (and thus scatters at a different angle). This is illustrated in figure 2.5 displaying the results of a simulation [22], where a plot of the positron momentum versus electron momentum of the e^+e^- pairs shows Bethe-Heitler processes (black circles) and A′ events/ radiative trident processes (red crosses). As can be seen from the plot the Bethe-Heitler produced e^+e^- particles are focused along the axes in regions where one lepton takes most of the energy and A′ decays are focused in the region where $E_{e^+} + E_{e^-} \simeq E_0$. Where E_0 is the beam energy and E_{e^+} and E_{e^-} are the energies of the positron and electron respectively. The result of this is that the signal (A′ decay pairs) to background (Bethe-Heitler pairs) ratio is maximised in the region where both $E_{e^+} + E_{e^-} \simeq E_0$ and $E_{e^+} \simeq E_{e^-}$ (shown in the blue square on figure 2.5). For APEX this resulted in placing spectrometers used for detecting the e^+ and e^- at equal angles from the beamline.

e^+e^- photoproduction is a two-stage process: firstly bremsstrahlung through the interaction of the electron beam with the target, followed by interaction of the produced bremsstrahlung photon with the target to pair produce e^+e^-.The Feynman diagrams for both steps are shown in figure 2.6. The nature of this process results in a contribution to the background which depends on the target foil from which the pair originates. The intensity of bremsstrahlung photons increases as the electron beam passes through each foil, reaching a maximum at the tenth (furthest downstream) target foil. e^+e^- pair production from these bremsstrahlung photons increases correspondingly at each foil. This is best understood through simulation, taking into account the energy of the electron beam (2.138 GeV) and target material and thickness. This is described in more detail in section 5.5.

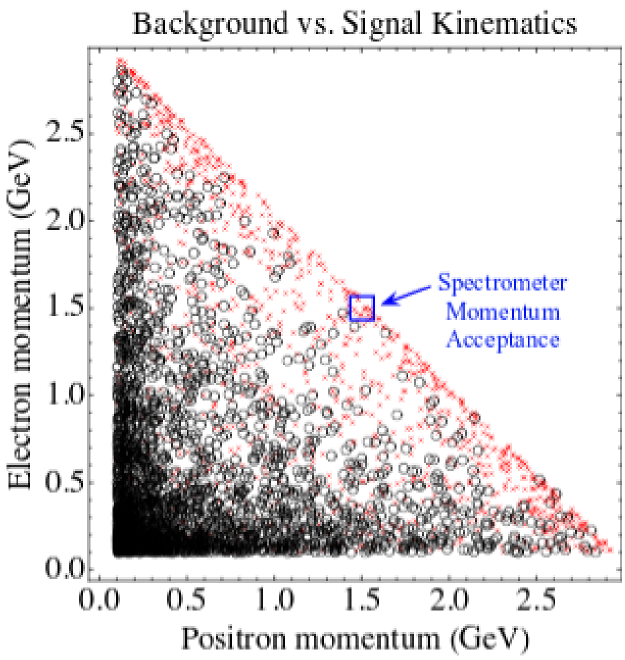

Figure 2.5: Electron momentum vs Positron momentum for simulated A' signal events (red crosses) and Bethe-Heitler background (black circles) with a 3 GeV beam. The area of optimised signal (A') to background (Bethe-Heitler) ratio is represented as a blue box [22].

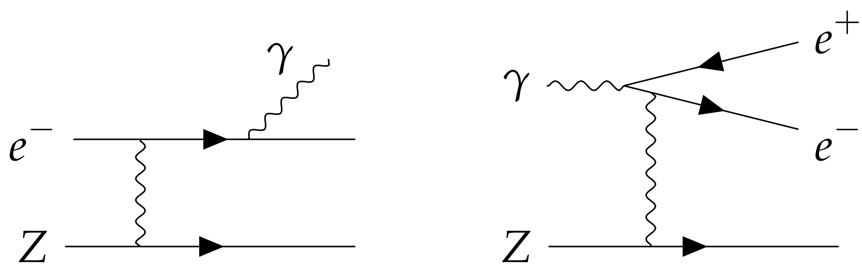

Figure 2.6: Feynman diagrams for e^+e^- photoproduction.
Left: bremsstrahlung, Right: e^+e^- pair production.

Chapter 3

APEX Experimental Set-up

In this chapter the experimental programme and set-up for APEX will be discussed. A 2010 test run was carried out with a beam energy of 2.260 GeV. In 2019, a production run was carried out with a beam energy of 2.138 GeV, motivated by the remaining uncovered parameter space in $P(m_{A'}, \epsilon^2)$. This chapter will describe the experimental set-up for the 2019 production run, though the principle, and majority of the set-up, was the same for both runs.

The experiment was housed in experimental Hall A of Jefferson Lab. The continuous electron beam at Jefferson Lab was used, with both the beam current and energy measured and monitored. The beam was rastered upstream of the target, with its position measured by Beam Position Monitors. This beam was collided with a fixed target of ten tungsten foils. Two spectrometer arms, the 'High Resolution Spectrometers', were set-up with polarities such that one recorded the e^+ and the other the e^- of an e^+e^- pair, with a septum magnet deployed to reach smaller angles. Both spectrometers were equipped with an array of detectors: a Cherenkov detector and calorimeters used for particle identification, a vertical drift chamber used to form particle tracks, and scintillators for timing. Combinations of the scintillators and Cherenkov detector were used for triggering. The Hall A data-acquisition system was used to process triggers and record information from detector and beamline systems. Retractable sieve slits were installed before the septum, and used in the process of optimising the spectrometer magnetic optics (see section 4.5). Also discussed are the different coordinate systems employed in analysis of data from the High Resolution Spectrometers.

3.1 APEX Experimental Programme

APEX carried out a test run in 2010, establishing a lower limit of $\epsilon^2 \simeq 10^{-6}$, using a single Tantalum foil target with thickness of $0.0032X_0$ (where X_0 is the radiation length) and a beam energy of 2.260 GeV. This demonstrated the viability of APEX as a dark photon search.

The APEX proposal planned for a production run at multiple beam energies, 6 days each at beam energies of 1.1 GeV, 2.2 GeV, 3.3 GeV and 12 days at 4.4 GeV. For each beam energy setting a total e^+e^- sample of $\mathcal{O}(10^8)$ events were expected. The achieved limits from the 2010 analysis, and projected limits from the proposal are shown in figure 3.1 [1,22]. It should be noted that the projected reach estimates from the proposal did not take into account e^+e^- pair photoproduction (as discussed in section 2.4). Including these events in the calculation of the radiative fraction (as detailed in section section 5.5.1) would reduce the sensitivity of the measurement and result in the projected limits in ϵ^2 being moved upwards. For the 2019 run (with a beam energy of 2.260 GeV) the effect of e^+e^- pair photoproduction on f and ϵ^2 was found to be mass dependent, varying from ∼10% to ∼30%. This effect of e^+e^- pair photoproduction on f and ϵ^2 is also dependent on the target set-up used.

The projected parameter space covered at beam energies of 3.3 GeV and 4.4 GeV has been ruled out by measurements from LHCb, as can be seen in figure 3.1 [44,45]. For this reason it was decided to run with a single beam energy of 2.138 GeV (close to the 2.2 GeV setting). The 2019 production run took place from the 14$^{\text{th}}$ of February until the 19$^{\text{th}}$ of March 2019, collecting a total charge of around 25 C on target and a final event sample of ∼52 million e^+e^- pairs (after all cuts) in an invariant mass range of ∼125-233 MeV. The production run used ten tungsten foil targets, each with a thickness of $0.0028X_0$. This thesis describes the 2019 production run, its set-up and analysis.

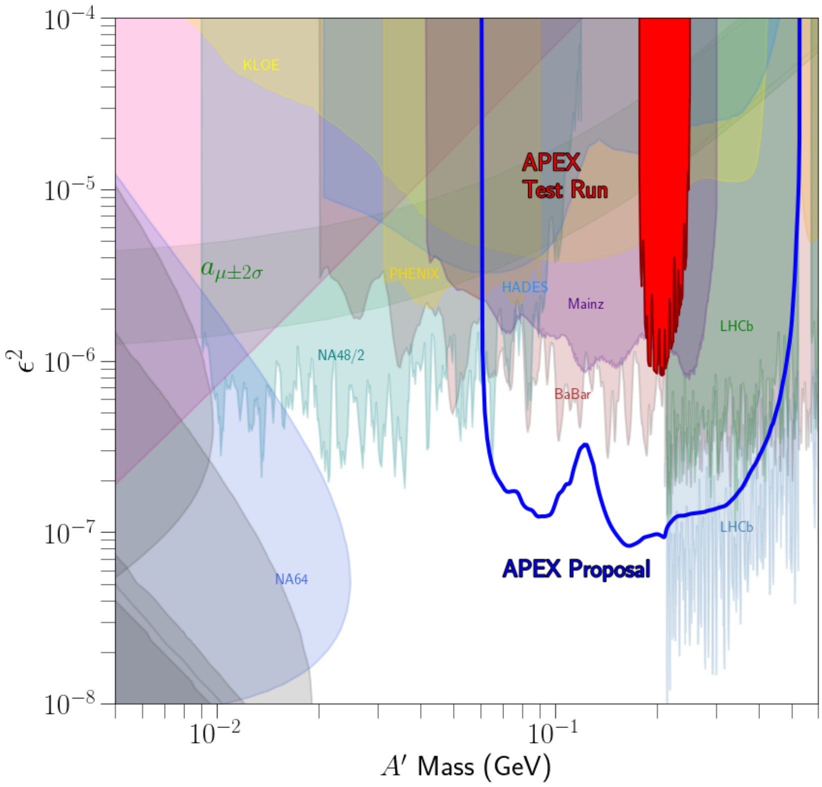

Figure 3.1: Exclusion plot for A′ searches in ϵ^2 versus $m_{A'}$. The APEX test run (2010) limits are shown in solid red, the projected limits from the APEX proposal for running at beam energies of 1.1 GeV, 2.2 GeV, 3.3 GeV and 4.4 GeV are displayed with a blue outline. Exclusion zones established by other experiments are also displayed.

3.2 APEX Apparatus

The second (and initial test) run of APEX took place in Hall A of Jefferson Lab (JLab). This facility, funded by the U.S. Department of Energy, is a national laboratory based in Virginia, USA. The primary purpose of JLab is to test the nature of QCD: probing hadron structure and studying hadron spectroscopy. For this pursuit JLab houses four experimental halls (A, B, C and D) with halls A and C possessing detector systems that focus on high luminosity measurements over angular coverage and halls B and D the reverse. All halls contain fixed target experiments that are fed by the CEBAF (Continuous Electron Beam Accelerating Facility) electron beam. Beginning its initial physics programme in 1995, the maximum beam energy of the facility was set at 6 GeV. This allowed the lab to achieve discoveries such as observing the unforeseen behaviour of the ratio of the proton's electromagnetic form factors G_E^p/G_M^p at high Q^2, pushed forward a variety of precision measurements in hadron physics [62], and included the test run of APEX in 2010 [1]. The facility then underwent a 12 GeV upgrade (with first beam in 2014) raising the energy of the beam and leading to an increased focus on BSM (Beyond Standard Model) physics (this is also when Hall D, the fourth hall, was added) [63].

3.3 CEBAF

The CEBAF produces a continuous wave, polarisable electron beam that can be delivered to all four halls of JLab simultaneously. The energy capability was increased from 6 to 12 GeV by the recent upgrade, with currents of up to 100 μA possible [63].

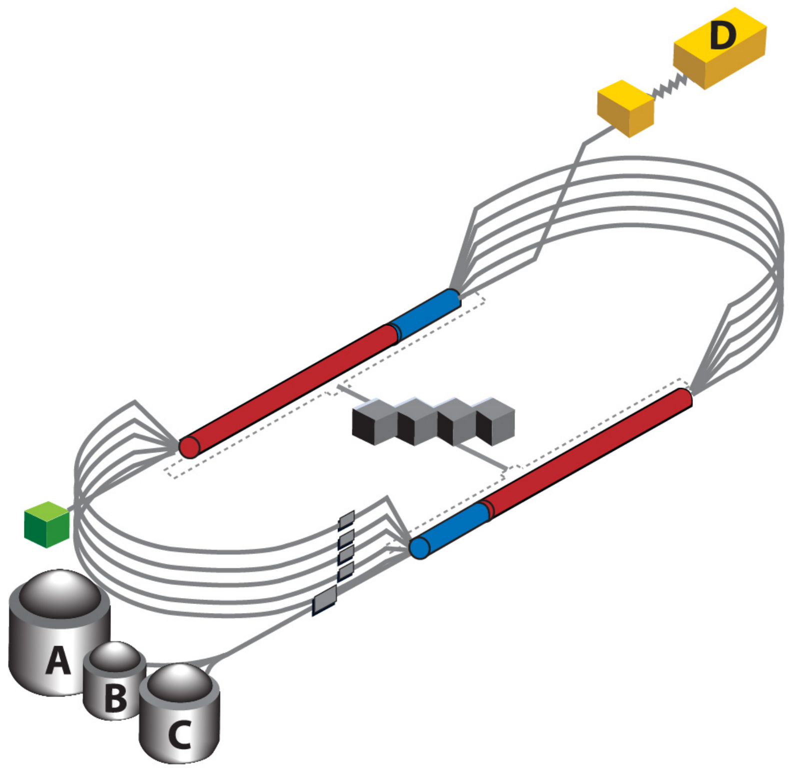

Figure 3.2: Schematic of CEBAF, following the 12 GeV upgrade [64].

The electrons are initially produced from the injector by a polarised, pulsed laser directed at a strained GaAs crystal. This pulsing produces separate bunches for each Hall, separated by 0.7 ns. As seen in figure 3.2, CEBAF consists of a 'race-track' configuration: two LINACs (linear accelerators) and two recirculating arcs (magnets) at each end connecting them and feeding electrons back around in a loop. These LINACs use SRF (Superconducting Radio-Frequency) cavities made from niobium, a material that becomes superconducting below 4.2K and is held at such temperatures by the liquid helium system at JLab, allowing for the continuous acceleration of electrons. The LINACs consist of 25 such cavities and provide a maximum acceleration of 2.2 GeV per pass with a maximum of 5 passes for Halls A, B and C (resulting in a maximum energy of 11 GeV for these halls). For Hall D there is a maximum of 5.5 beam passes, allowing for a 12 GeV beam. For Hall A, the beam is ultimately diverted by a series of magnets at the beam switch yard and sent to the Hall A beamline.

3.4 Hall A

The largest of the four experimental halls, Hall A has traditionally run an experimental programme focused on high precision hadron structure measurements suited to its standard detector set-up, the HRSs (High Resolution Spectrometers). The HRSs were used for the 2019 APEX run as well the 2010 test run [1]. The Hall A beam delivery, detector and DAQ systems are detailed in the following sections.

3.4.1 Hall A Beamline

The beamline transports beam to the target from the switch yard as described above. Eight dipoles magnets are used to steer the beam to the Hall A target, with the beam being transported to the beam-dump after traversing the target. It is important to continuously monitor and measure various properties of the beam as it is being propagated to ensure beam quality is maintained. For APEX, important parameters to measure were the beam position and current (beam polarisation was not important for the experiment, and beam energy is well-known and measured through various CEBAF monitors). The beam line apparatus is illustrated in figure 3.3 (for general Hall A experiments with HRSs, not specific to APEX set-up), with the beam travelling from left to right. In figure 3.3, 'BCM' refers to the Beam Current Monitor, 'BPM' to the Beam Position Monitor, 'Raster' to the magnet system used to raster the beam and 'Q1', 'Q2', 'Q3' and 'Dipole' to the quadropole and dipole magnets of the HRS. All of which will be detailed further. The Compton polarimeter, Møller polarimeter and EP referenced in figure 3.3 are not relevant to APEX and are not discussed further.

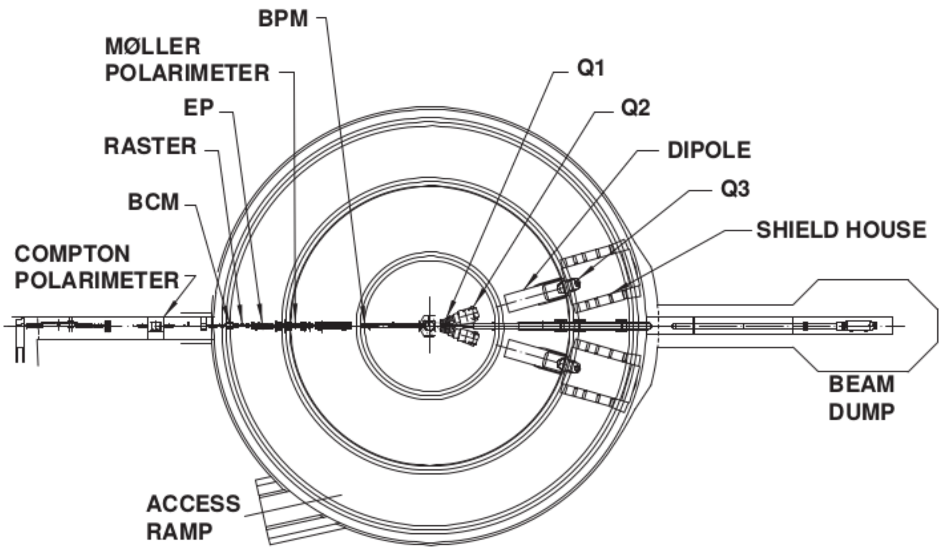

Figure 3.3: Schematic layout of the Hall A beam line (shown for general experiment without septum magnets installed), with beam travelling from left to right [65].

3.4.2 Position measurement

For APEX the beam-position is an important property to track as it is key in determining the initial position of the target interaction. In Hall A this is measured by two BPMs (Beam Position Monitors) located at 7.524m (BPMA) and 1.286m (BPMB) upstream of the standard target position. The BPMs consist of four open-ended antenna orientated at 90° to one another and positioned coaxially around the beamline, as depicted in figure 3.4. These antenna are tuned to the fundamental RF frequency of the beam. The four antenna are labelled u_+, u_-, v_+ and v_- with the antenna labelled with subscript '$+$' being directly across from those with subscript '$-$' within the u and v pairs. As the beam passes through this cavity a signal is induced in the antennae which is inversely proportional to the beam's position. From the differences in $u_+(v_+)$ and $u_-(v_-)$ signals a position can be determined in the axis connecting them [66]:

$$u(v) = \frac{u(v)_+ - u(v)_-}{u(v)_+ + u(v)_-}. \tag{3.1}$$

This 'difference-over-sum' technique gives a precision of within 100 µm with a beam current above 1 µA [65].

The BPMs are calibrated from an absolute measurement of the beam position performed by the Hall A harp wire scanners. The harps contain three wires at different angles to the beam which receive signals dependent on their distance to the beam.

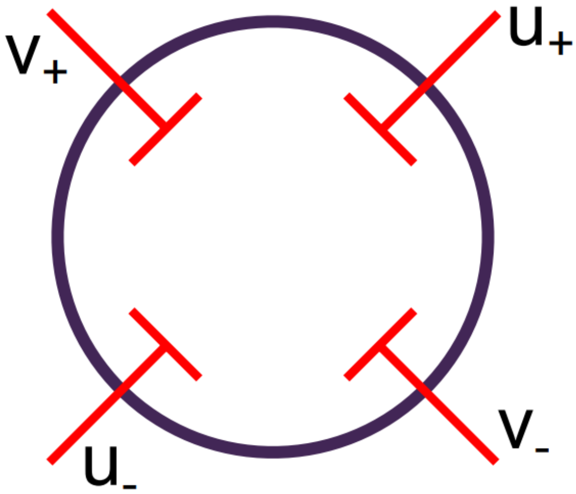

Figure 3.4: Beam Position Monitor (BPM) Chamber layout showing orientation of four sense wires. View looking downstream [66].

When inserted into the beam line the known position of the wires and the angles can be used to determine the exact position of the beam from which the BPMs can be calibrated [66] [67].

3.4.3 Beam Rastering

As with other Hall A experiments, APEX required for the electron beam to be rastered in order to avoid damage to the target. 'Rastering' in this context is cyclically moving the beam position at the target to avoid overheating and damaging the target. Fast rastering is achieved with two dipole magnets, for horizontal and vertical movement of the beam which are located approximately 17 metres upstream of the target [66]. A 25 kHz triangular wave is used to drive both magnets to provide an adjustable size raster, which was set to 1.5 mm × 5 mm for APEX productions runs.

The beam position is altered by the raster proportional to the current in the horizontal and vertical dipoles. This effect can be described by:

$$x^{rast} = O_x + A_x I_x^{rast}, \tag{3.2}$$

$$y^{rast} = O_y + A_y I_y^{rast}, \tag{3.3}$$

where x^{rast}, y^{rast} are the desired beam positions obtained from the raster, I^x, I^y are the mean raster currents and O_x, O_y, A_x, A_y are coefficients that must be calibrated.

3.4.4 Current measurement

The measurement of the beam current is performed by the Hall A Beam Current Monitor (BCM). This consists of an Unser monitor and two RF cavities, one either side of the Unser. The apparatus is enclosed within a box to provide necessary heat and magnetic shielding. The Unser, a parametric current transformer, acts as a reference for calibrating the RF cavities. The two cavities are cylindrical waveguides, tuned to the frequency of the beam (1.497 GHz [65]), which produce a voltage level in their outputs proportional to the beam current. This can also be referenced against additional monitors in the injector section of the beam line adding more redundancy to the system.

3.5 High Resolution Spectrometers

The Hall A HRSs are two magnetic spectrometers, designed for high angular and momentum resolution measurements. Both spectrometers have a QQD_nQ magnet configuration as shown in figure 3.5, with one arm set to positive polarity whilst the other is set to negative. The superconducting, indexed dipole magnet introduces a 45° bend in the central trajectory of particles and this dispersive bending of the beam, combined with tracking information, allows the determination of a particle's momentum (from its difference in position compared to the central trajectory) [65]. This dipole also focuses the beam in the vertical plane. The quadrupole magnets function as focusing and defocusing elements; Q1 focuses in the vertical and defocuses in the transverse whilst Q2 and Q3 do the opposite. These quadrupoles allow the HRSs to achieve its fractional momentum resolution of 2×10^{-4} and acceptance of $\pm 4\%$ in fractional momentum [65].

The top of both HRS arms is home to a detector stack, visible in figure 3.5, contained in a shielding hut where for APEX the installed detectors were used for the purposes of tracking, triggering and PID. These detectors will be detailed in the remainder of this section.

3.5.1 Vertical Drift Chambers

Both arms possess a VDC (Vertical Drift Chamber) which serves the purpose of particle tracking. The VDCs consist of two gas-filled chambers (VDC1 and VDC2 as depicted in figures 3.6 and 3.10), each orientated at 45° to the central trajectory of the spectrometer (as shown in figure 3.5), and horizontal to the lab floor. These chambers in turn contain

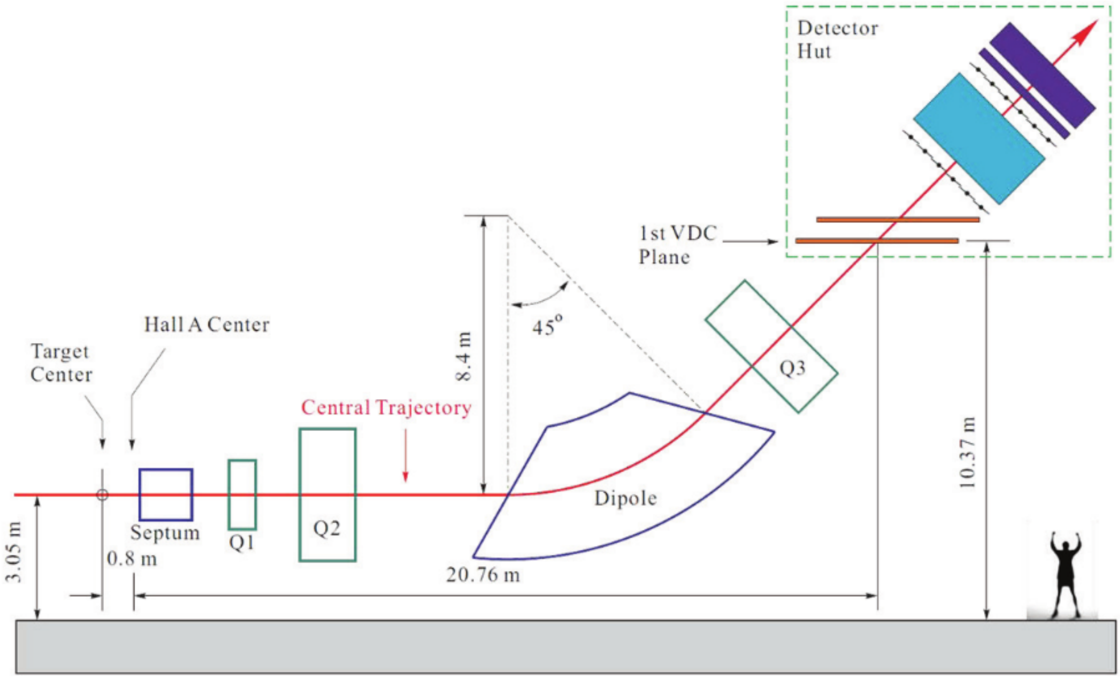

Figure 3.5: HRS: layout displaying QQD_nQ configuration bending the central trajectory of particles towards detector hut. Beam travelling from left to right [68].

two planes of wires in a 'U-V' formation, with the wires in one plane orientated at 90° to the other [69], as shown in figure 3.6.

Each plane has 368 gold-plated, sense wires which are held at ground voltage whilst the gold-plated, Mylar frame the wires are attached to is held at -4kV [69]. This provides the electric field needed for ionisation of the gas inside the chamber. A gas mixture, of 62% Argon and 38% Ethane, is used with Argon being the ionisable gas, and ethane the 'quencher' (absorbs the photons produced from ionisation) [65]. As a charged particle traverses one of these planes, it interacts with the electric field around the sense wires and ionises Argon atoms in the chamber. These electrons drift towards the sense wires at a near constant velocity, then as they approach the wire the radial behaviour of its field at smaller distances causes the electron to accelerate and produce an 'avalanche' of electrons. The ions produced drift instead towards the frame which acts as a cathode. Both of these phenomena induce a negative pulse in the sense wire which is recorded by Time-to-Digital Converters (TDCs).

The timing signals from wires are then used in 'cluster formation' where these timing signals are converted to distances, 'Time To Distance conversion' (TTD), and then a slope and intercept for a cluster of hits is extracted. This is discussed in more

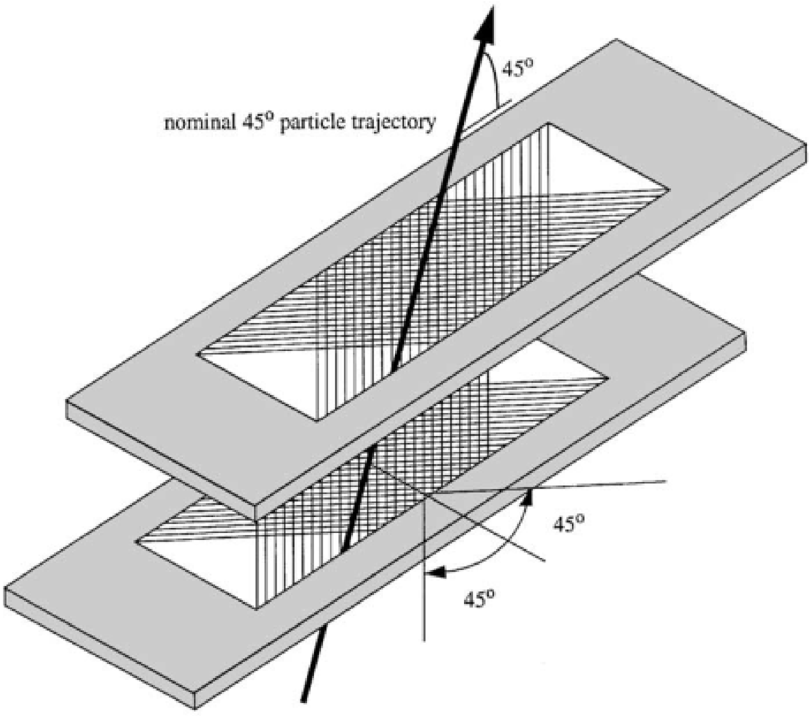

Figure 3.6: VDC configuration, showing both chambers with example particle trajectory [69].

detail in section 4.4. The VDCs have an estimated per-plane position resolution of 96 μm [69].

3.5.2 Gas Cherenkov

Gas Cherenkov detectors are present in both spectrometer arms and are used for the purpose of Particle Identification (PID). They are located in the detector stack between the two scintillator planes. The basic principle of a Cherenkov detector is that when a particle travels through a medium faster than the speed of light (possible if the refractive index of the material, n > 1), it forms a coherent light wave in its wake due to the response speed of the medium (c/n) being smaller than the particle's velocity. This coherent 'shock-wave' is formed at an angle of $\theta = \arccos(\frac{1}{\beta\eta})$ with respect to the particle trajectory, where $\beta = v/c$ with v being the particle velocity. This phenomenon has a cut-off for velocity, which can be translated into a momentum cut-off as described by:

$$\beta \geq \frac{1}{n}, \tag{3.4}$$

$$\implies p = \frac{mv}{\sqrt{1-\beta^2}} \geq \frac{mc}{\sqrt{n^2-1}}, \tag{3.5}$$

where m is the particle mass.

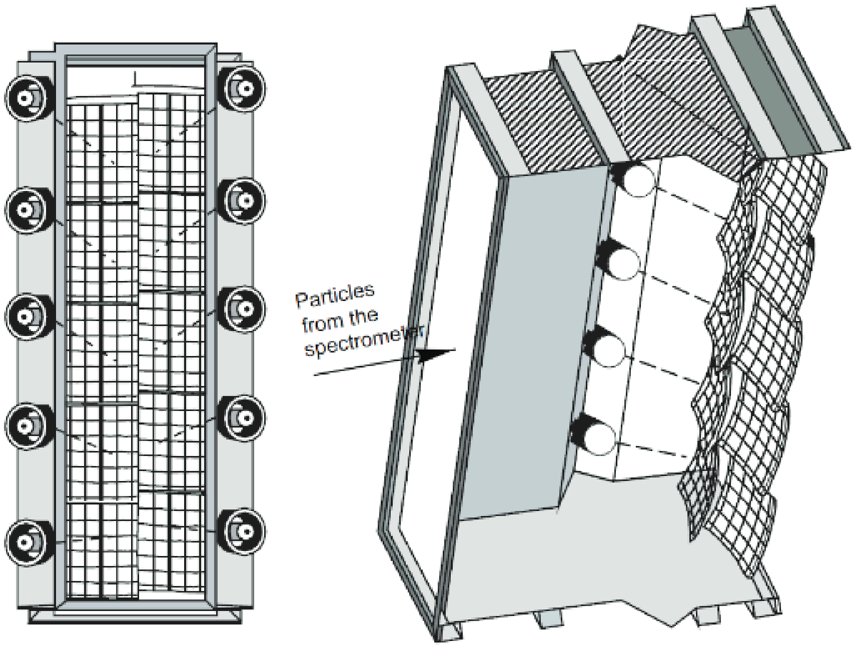

Figure 3.7: Hall A Cherenkov detector: Configuration showing 10 spherical mirrors in two columns of five. Left shows 'front view' looking from downstream, right shows partially open '3D' side view. [70].

The Cherenkov detectors in Hall A consist of ten spherical mirrors which are configured to slightly overlap each other and function to focus light to ten corresponding PMTs (Photomultiplier Tubes), as shown in figure 3.7. CO_2 gas is used in the Cherenkov detectors, and with n = 1.00041, this results in a threshold of 0.0018 GeV/c for electrons/positrons and a much higher threshold of 4.87 GeV/c for pions [70]. As the momentum acceptance of the HRS is limited to < 4 GeV and the central momentum for both arms for APEX production was $\sim$ 1.1 GeV, this means the Cherenkov detector can discriminate between electrons/positrons and pions with an efficiency of $\sim$99% [65]. The Cherenkov detector PMT signals are read out by both TDCs and FADCs (Flash Analogue-to-Digital Converters).

3.5.3 Electromagnetic Calorimeters

The electromagnetic calorimeters (also known as 'shower' detectors) serve the purpose of PID in the experiment and are the final detectors on both HRS arms. The calorimeters are made from lead glass blocks with PMTs attached (connected to a HV (High Voltage) supply), with the signals ultimately read out via ADC (Analogue-to-Digital Converters) channels. As a charged particle traverses the lead-glass blocks it deposits its energy primarily through bremsstrahlung and electron-positron pair production. Electrons deposit almost all of their energy into the calorimeter whereas the majority of hadrons retain a large fraction of their initial energy. Comparing the detected momentum versus energy deposition of a particle can thus provide a method of PID.

The makeup of the calorimeters differs between the LHRS and RHRS. Both are two layer calorimeters. For the LHRS both layers of the calorimeter, Pion Rejector 1 (PRL1) followed by Pion Rejector 2 (PRL2), consist of 34 lead-glass blocks 30 cm thick with faces of 15 cm $\times$ 15 cm. Both layers in the LHRS are orientated perpendicular to the track. The showers produced in each block are read out via PMT and then FADC.

For the RHRS the first calorimeter layer (Preshower (PS)) is orientated perpendicular to the track and consists of 48 lead-glass blocks 35 cm thick with front dimensions of 10 cm $\times$ 10cm. The second layer for the RHRS calorimeter (Shower (SH)) is orientated parallel to the tracks and is formed from 80 lead-glass blocks, 35cm thick with faces of 15cm $\times$ 15cm. The showers in each block are read out via PMT then ADC.

3.5.4 Scintillators

For APEX both HRS arms possessed two scintillators, S0 and S2, that were used for triggering and timing information in the experiment. The S2 scintillator, placed after the VDC, consists of sixteen 'paddles', 178 mm thick with dimensions of 51 mm in x and 140 mm in y (in the Transport Coordinate System (TRCS) described in 3.5.5). The paddles are made from EJ-230 [65], a fast plastic scintillator, which means S2 can provide the precise timing information needed in the experiment. S0 is the first detector after the VDC in the stack and is comprised of a single large paddle made from 10 mm thick BICRON 408 plastic scintillator [65]. The dimensions of S0 are 170 cm in x and 25 cm in y (in the TRCS).

For each paddle in S0 and S2 there are two PMTs, one connected to either end. These are read out by both TDCs and FADCs. The timing resolution for the S0 is $\sigma_t = 200ps$ and for S2 is $\sigma_t < 150ps$ [65]. As APEX was a coincidence experiment the scintillators were important in providing a coincidence time between recorded events in the LHRS and RHRS.

3.5.5 HRS Coordinate Systems

Several established coordinate systems are used in the description of the HRSs [71]. This is important for calibrating the spectrometer optics (tracing tacks formed in VDC to target), as described in section 4.5, as different coordinate systems are used in the stages of this process. These systems provide convenient descriptions of the various stages of track reconstruction: from track formation in the VDC to final variables at the target. In the VDC the Detector Coordinate System (DCS) and then Focal Plane Coordinate System (FCS) (via the Transport Coordinate System (TRCS)) describe the tracks formed. These are then reconstructed to the quantities at the target (in the Target Coordinate System (TCS)) which for the APEX analysis are needed for the calculation of the final invariant mass. The Hall Coordinate System (HCS) is used to describe beam position, target position and HRS position and orientation from which these are defined in the TCS.

All coordinate system diagrams in this section are reproduced from [71] and [72].

Hall Coordinate System

The HCS origin is defined by the intersection of the beam with the vertical axis of the target. For standard set-ups this coincides with the centre of the experimental hall but the septum magnets installed for APEX meant the origin was moved -1.053 m upstream. The $\hat{z}$ axis is defined as along the beam (from hall entrance to beam dump), with positive $\hat{y}$ direction as vertically up and positive $\hat{x}$ to the left if facing along $\hat{z}$.

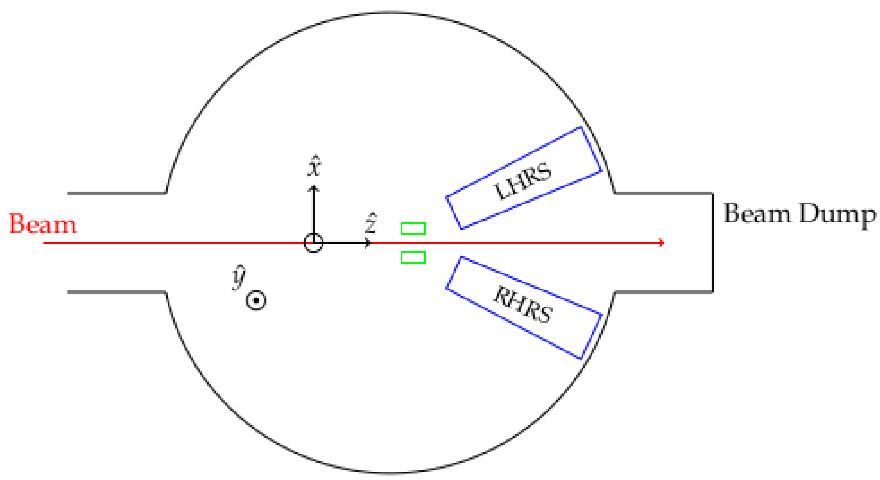

Figure 3.8: Hall Coordinate System. Shown with septum magnets (Green) installed.

Target Coordinate System

The TCS is defined separately for both spectrometer arms. The $\hat{z}_{tg}$ axis is defined by a line passing through the central hole of the sieve (described in section 3.9), perpendicular to the sieve plane (with positive $\hat{z}_{tg}$ pointed towards the sieve from the target). The $\hat{y}_{tg}$ axis is defined as pointing towards the left looking along $\hat{z}_{tg}$, with $\hat{x}_{tg}$ pointing downwards. In the ideal definition, the $\hat{z}_{tg}$ axis passes directly towards the hall centre (which becomes the origin of the TCS in this ideal case), and the distance from sieve to hall centre defines 'L' (marked on figure 3.9). In reality there are deviations (marked by D_x and D_y in figure 3.9) which are measured by a survey of the hall. The angle from the $\hat{z}$ axis of the HCS and $\hat{z}_{tg}$ is the central angle, θ_0 ($\pm 5^\circ$ for APEX). The in-plane (non-dispersive) angle is then defined as $\phi_{tg} = dy/dL$, and out-of-plane (dispersive) angle as $\theta_{tg} = dx/dL$. The distance from the Hall Centre to the interaction vertex is denoted, z_{react} , as marked on figure 3.9.

Detector Coordinate System

The origin of the DCS is defined by the intersection of wires 184 (central wire) of the U1 and V1 planes of the lower VDC chamber (VDC1), as shown in figure 3.10. The $\hat{z}$ axis is defined as vertically upwards. The $\hat{x}$ axis is defined as being parallel to the short symmetry axis of VDC1 and pointing downstream with $\hat{y}$ defined as parallel to the long symmetry axis and pointing towards the left when facing in the positive $\hat{x}$ (downstream) direction. The angles are defined as $\theta_{det} = dx/dz$ and $\phi_{det} = dy/dz$. Tracks formed in the VDC are described in this coordinate system, as detailed in section 4.4.

Transport Coordinate System

The TRCS at the focal plane is defined by a rotation of the DCS around its y axis by 45°. This coordinate system is used as an intermediate step in converting coordinates in the DCS to the FCS. Coordinates in the TRCS can be converted from the DCS as:

$$\theta_{tra} = \frac{\theta_{det} + \tan(\rho_0)}{1 - \theta_{det}\tan(\rho_0)}, \tag{3.6}$$

$$\phi_{tra} = \frac{\phi_{det}}{\cos(\rho_0) - \theta_{det}\sin(\rho_0)}, \tag{3.7}$$

$$x_{tra} = x_{det}\cos(\rho_0)(1 + \theta_{tra}\tan(\rho_0)), \tag{3.8}$$

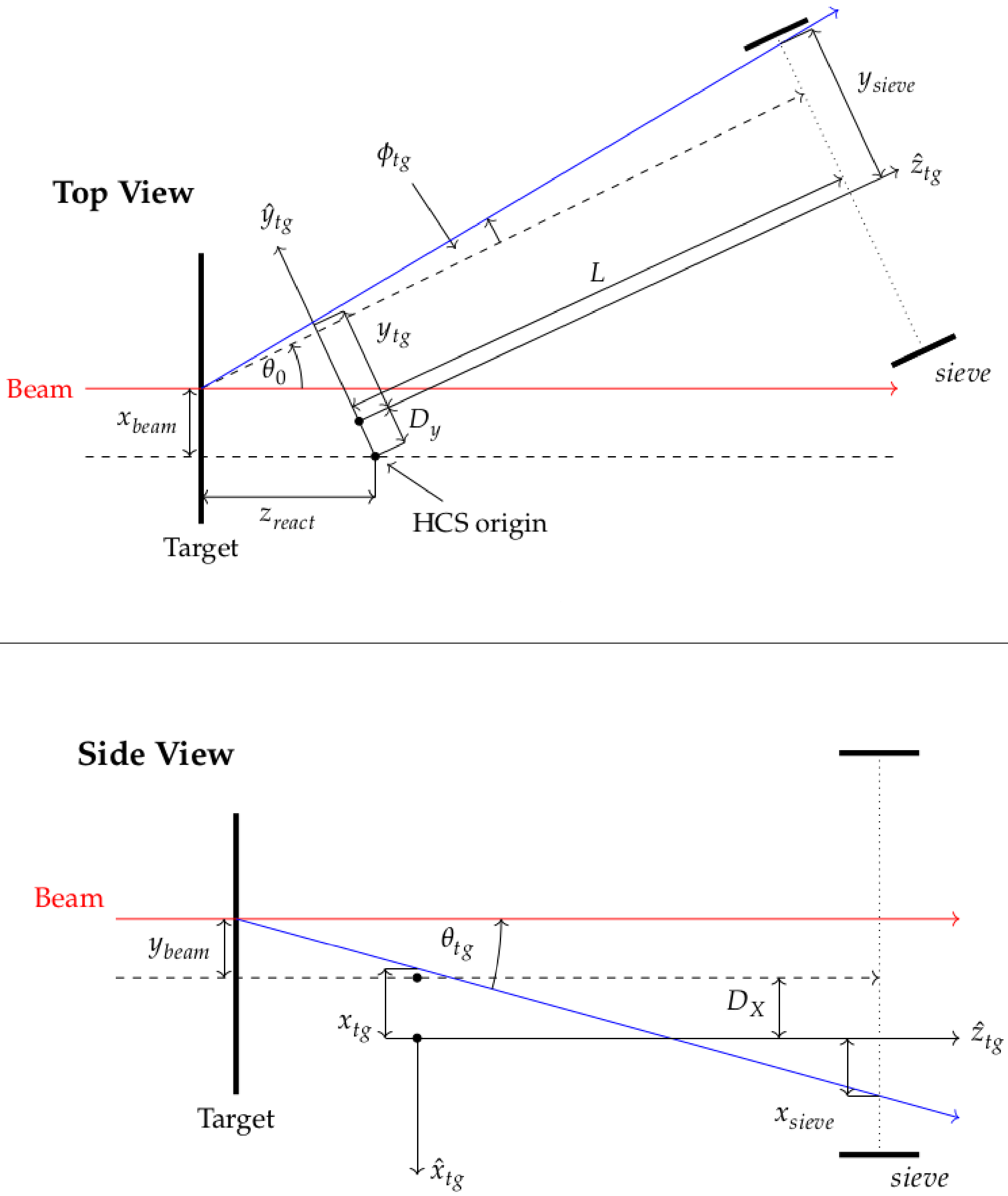

Figure 3.9: Target Coordinate System (top and side views). The HCS origin is labelled, with the TCS origin having horizontal and vertical deviations from this marked as D_x and D_y respectively. θ_0 is the central angle.

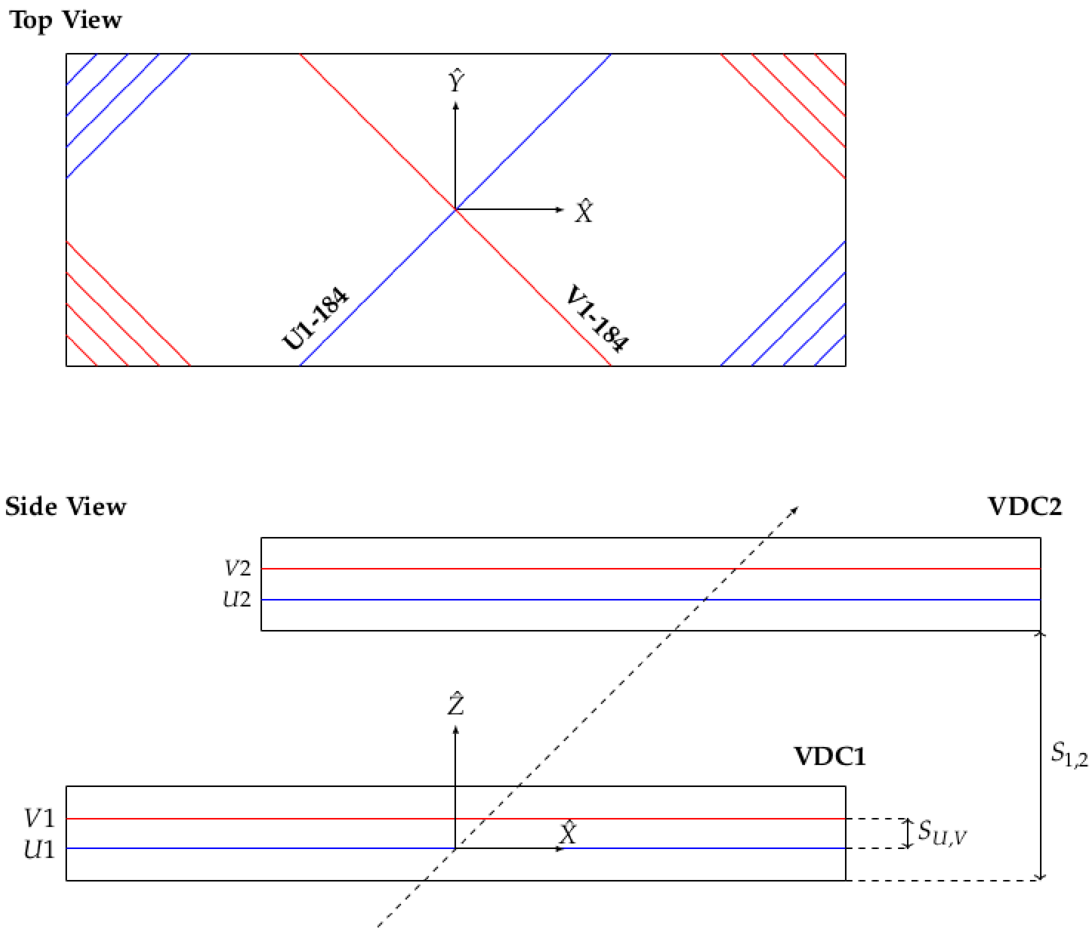

Figure 3.10: Detector Coordinate System (top and side views). The top view shows VDC1, with the intersection of wires 184 from U1 (U1-184) and V1 (V-184) defining the DCS origin. $S_{1,2}$ denotes the vertical distance between the two VDC chambers and $S_{U,V}$ denotes the vertical distance between the U and V VDC planes within one VDC chamber. The typical particle trajectory is shown with a dashed arrow in the side view.

$$y_{tra} = y_{det} + \sin(\rho_0)\phi_{tra}x_{det}, \tag{3.9}$$

where $\rho_0 = -45^\circ$ is the rotation angle.

Focal Plane Coordinate System

The FCS is defined as a rotation of the TRCS around its y axis by an angle ρ such that $\hat{z}_{FP}$ is parallel to the 'local central ray', defined as having scattering angles $\theta_{tg} = \phi_{tg} = 0$ for the track momentum, p. This is illustrated in figure 3.11. Particles traversing the HRS with the same momentum will be focused at the focal plane, making the relative momentum, $\delta p = \frac{(p-p_0)}{p}$ where p_0 is the central momentum, a function of x_{tra} (and

p_0). The rotation angle, ρ, is thus a function of x_{tra}, ie $\rho(x_{tra})$. Coordinates in the FCS can be translated from the DCS and TRCS as:

$$x_{fp} = x_{tra}, \tag{3.10}$$

$$\theta_{fp} = \frac{\theta_{det} + \tan(\rho)}{1 - \theta_{det}\tan(\rho)}, \tag{3.11}$$

$$y_{fp} = y_{tra} - \sum C^{y}_{i000} x^{i}_{fp}, \tag{3.12}$$

$$\phi_{fp} = \frac{\phi_{det} - \sum C^{p}_{i000} x^{i}_{fp}}{\cos(\rho)(1 - \theta_{det}\tan(\rho))}, \tag{3.13}$$

$$\tan(\rho) = \sum C^{t}_{i000} x^{i}_{fp}, \tag{3.14}$$

where the coefficients C^{y}_{i000}, C^{p}_{i000} and C^{t}_{i000} account for systematic offsets in the VDCs due to misalignment.

For the FCS the dispersive angle (θ_{fp}) is small across the entire focal plane, and approximately symmetric. This results in a faster convergence during the process of optimising the optics matrix (used to project coordinates from FCS to TCS as described in 4.5) [71].

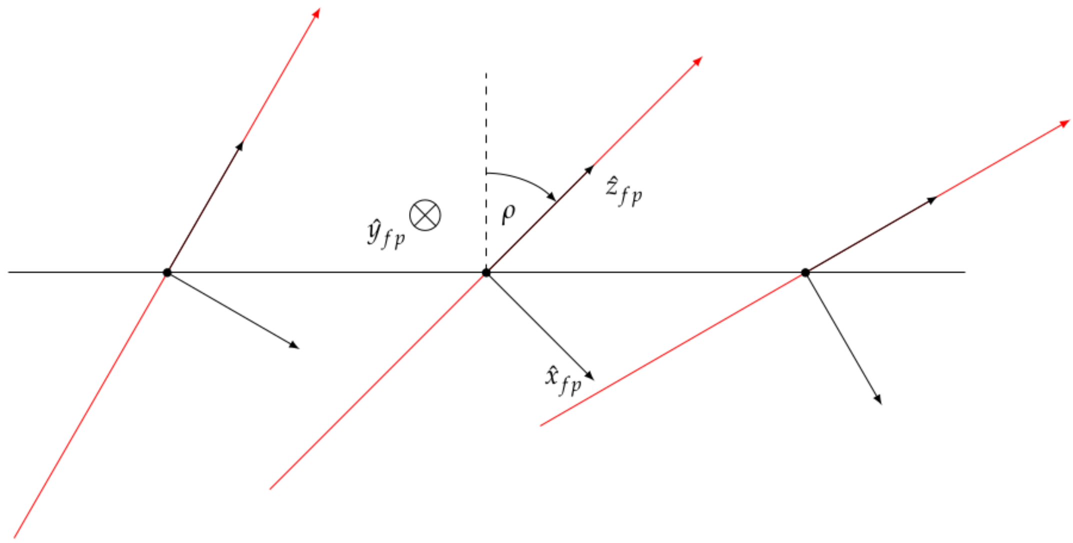

Figure 3.11: Focal Plane Coordinate System. The red trajectories show local central rays with $\theta_{tg} = \phi_{tg} = 0$.

3.6 Hall A Data Acquisition

The Hall A data-acquisition (DAQ) system consists of a combination of hardware and software elements designed to control the reading of data during experiments and its subsequent storage. This system is built around CODA (CEBAF On-line Data Acquisition System), a software framework developed for JLab which manages the readout of hardware components and enables the reading, monitoring and storage of data [73]. Detector channels are read out and digitised by Fastbus or VME modules (Fastbus for ADC and TDC, VME for FADC). Certain channels are also read out as scalars, used primarily for online monitoring. EPICS (Experimental Physics and Industrial Control System) [74] information, which for APEX recorded beam current and position, HRS and septum magnet settings and currents, beam position and current and other variables, was also injected into the data-stream.

The read out of detectors was controlled by CODA and can be split into different processes:

- Readout Controllers (ROCs) are single-board computers mounted and ran on the front-end modules (as described above which read out detector signals). The ROCs buffer collected data in memory and then transfer the data, 'event fragments', to the Event Builder.
- The Event Builder (EB) collects data from the different ROCs and merges this into a data structure in the CODA format. This process combines the several event fragments (ultimately data read out from the various detectors) into one 'event'. Events serve as the unit of analysis, associating output in the various detectors to one interaction.
- The Event Transfer (ET), which is used to insert additional data (EPICS, scalers) into the data stream, and allow online access (used for monitoring of detectors).
- The Event Recorder (ER) writes the data stream to a local disk before final storage.
- The RunControl process which controls the starting and stopping of runs and experimental configurations used. For APEX different configurations were used for optics runs where one arm recorded data with a low beam current, 'cosmic' test runs which were ran with no beam current (to test detector performance) and production runs with both arms recording data to obtain the final experimental result.

Finally the data is sent to the mass storage tape silo (MSS) at JLab for long-term storage. From this tape storage individual runs can be retrieved for analysis [75].

3.6.1 APEX Triggers

Triggers in the HRS are controlled by the Trigger Supervisor (TS) system including the Trigger Supervisor version 2 (TS2) module, a Transition Module (TM) and an interface card for each front-end ROC [75]. Triggering controls the readout of detectors, with data being taken only when set conditions are met: corresponding to a 'good event'. The TS2 module accepts and prescales the triggers, and manages the dead-time logic of the system and the read-out and synchronisation of front-end crates. When a trigger is received the TS2 module sends a Level 1 Accept (L1A) signal [76]. The L1A signal is sent to the TM, which generates the TDC stops and ADC gates which are needed for the front-end ROCs. Re-timing of the L1A signal is controlled by a retiming (RT) module, with the retimed L1A signal used by the TM to generate new gates and common stops. The TMs on both arms can be ran in either independent mode where the L1A signals used on both arms are independent of each other or in paired mode, where the TS system of one arm controls the readout and timing of DAQ for both. APEX, as a coincidence experiment, used paired mode for the production runs with the RHRS TS system controlling readout for both arms. Independent mode was used for cosmic test and optics runs.

The triggers used for APEX were formed from combinations of single-detector triggers. These are summarised in table 3.1, with GC referring to the Gas Cherenkov detector and S2R the right paddle of S2. The single-detector triggers (that were used for APEX) were:

- Scintillator Triggers: signals from scintillator PMTs are discriminated, testing if they exceed a set threshold. For S0, with only one paddle the logical AND of both PMTs formed the S0 trigger. The S2 trigger was formed by any S2 paddle (of sixteen) having signals from both its PMTs passing the threshold: the logical OR of the sixteen paddles, each paddle requiring a logical AND of both PMTs. S2R trigger is formed by any S2 paddle having a signal on its right PMT exceeding the threshold: the logical OR of the sixteen paddles, each paddle needing only the right PMT signal to pass discrimination.
- Cherenkov Trigger: the sum of of all ten channel PMT signals is discriminated.

The combination of these single-detector triggers into more sophisticated triggers (as in T1, T4, T5 and T6) is accomplished by a Majority Logic Unit (MLU) on both arms. S2 has a greater timing resolution than other detectors, and is thus used to set the timing of the triggers. T2 and T5 were the primary triggers used for single arm running (optics, cosmic testing) on the LHRS and RHRS respectively. The T6 trigger was used for production, coincidence runs.

Trigger Label	Description
T1	LHRS S0&S2, with S2R timing
T2	LHRS S2, with S2R timing
T3	RHRS S2, with S2R timing
T4	RHRS S0&S2, with S2R timing
T5	RHRS GC&S2, with S2R timing
T6	T2&T5 coincidence, T2 timing

Table 3.1: Triggers used for APEX. T1-T2 describe single-arm triggers for the LHRS, T3-T5 describe single-arm triggers for the RHRS, T6 describes a coincidence trigger between both arms.

3.7 APEX Target

For APEX a unique target was designed and produced to meet the requirements of the experiment (details of its specifications are taken from [22]). The main features desired were to maximise the invariant mass range scanned and the statistics gathered, to achieve the best possible mass resolution and to minimise the QED trident background. From these specifications the APEX target was designed as shown in figure 3.12. The production targets are ten 2.5 mm wide, 10 micron thick tungsten wires placed 55 mm apart (bottom layer of target system (figure 3.12)). Tungsten was chosen as a high-Z material to maximise the number of e^+e^- pairs compared to pion background production. The 55 mm spacing between foils significantly reduces the probability of produced e^+e^- pairs that are within the HRS acceptance interacting further with the target. This means multiple scattering is limited to the individual foils whilst the beam passes through all ten foils, ensuring greater luminosity. This set-up also allows extended coverage of the invariant-mass range, with each foil corresponding to a different m_A (as discussed in section 2.3, $\theta \sim m_{A'}/E_0$ such that different foils correspond to different values of θ and thus $m_{A'}$).

The top layer of the target consists of eight carbon foils which act as the optics calibration targets for the experiment (top of figure 3.12). With this arrangement the beam can pass through four wires at one time or all eight and provide optics calibration along the full length of the production target.

The beam alignment section (second layer from top as in figure 3.12) has four horizontal and three vertical tungsten wires. The target system was accurately surveyed and the position of the alignment section known with respect to the rest of the system. This meant the alignment section could serve to align the beam as well as be used for optics calibration purposes. The vertical wires were staggered horizontally and the horizontal wires staggered vertically such that the beam could be positioned to hit only one. The third from top layer consists of ten carbon foils and was also used during the run to confirm beam alignment.

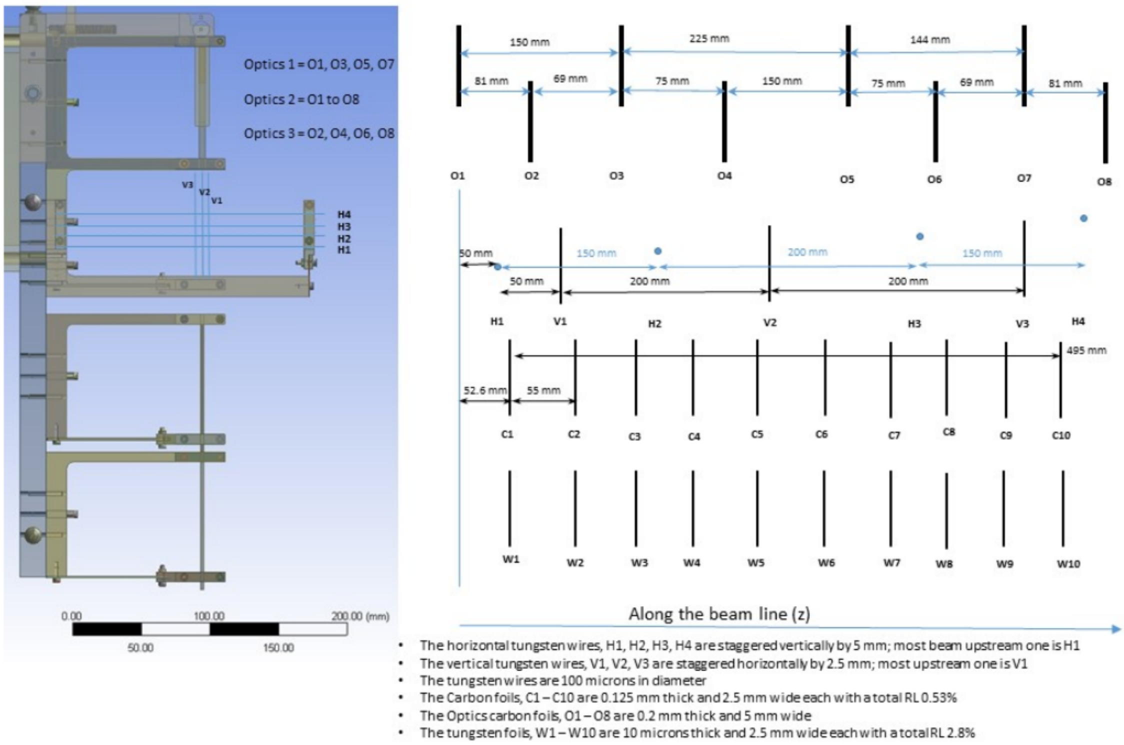

Figure 3.12: APEX target system. Top Layer: optics calibration targets, second (from top) layer: alignment targets, third (from top) Layer: Carbon foils, bottom layer: Tungsten Production Targets [22].

3.8 Septum Magnet

As described in section 2.3, A′ production is focused at small angles. The HRS spectrometers, however, are limited to a minimum angle of 12.5°. The APEX set-up thus employed a septum magnet, as shown in figure 3.5, to reach smaller angles. The septum magnet was constructed by Stony Brook University, and consists of a water-cooled iron septum run with a current of ∼1000 A. Figure 3.13 provides an illustration of the septum position between scattering chamber and entrances to the HRS arms. Corrector magnets were installed both upstream and downstream of the target to compensate for the fringe fields produced by the septum magnet.

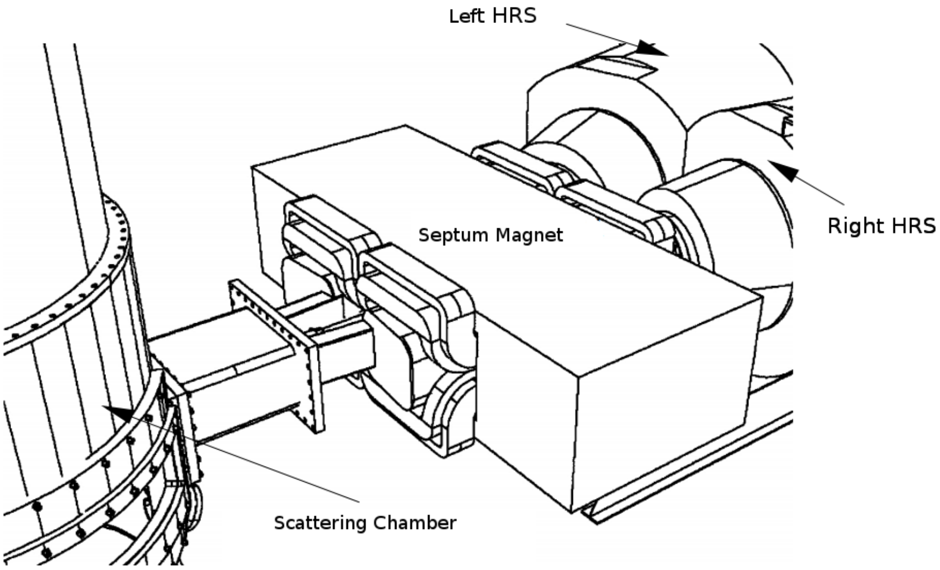

Figure 3.13: Diagram of APEX septum position, downstream of scattering chamber and upstream of HRS entrance (Taken from [22], showing position of older septum with same general layout as 2019 run).

The field strength of the septum and the HRS magnets (known as the septum and spectrometer 'tunes') for APEX are listed in table 3.2. Where the magnet settings are given as a factor by which the nominal field value for the central momentum (1.1 GeV for APEX) is multiplied.

Magnet	Setting
Septum	1.05
Q1	0.67
Dipole	1.0
Q2	0.95
Q3	1.20

Table 3.2: Spectrometer tune used for APEX. Values in Setting column are factors by which the nominal field value for the central momentum is multiplied.

3.9 Sieve Slits

Retractable sieve slits were installed before the septum, for the purpose of spectrometer optics optimisation as described in section 4.5. As shown in figure 3.14, each sieve slit has 225 holes used to obtain a precise and reliable description of the magnetic optics of the system across the entire acceptance. The 6.35 mm thick tungsten sieve slits are designed to be used in optics runs taken at a low beam current to stop all particles except from those passing through the sieve holes. Particles tracks formed in the VDC could then be assumed to have passed though the well-defined positions of the sieve holes, providing a known reference to calibrate from. This accuracy was assured by a detailed survey of the hall, including of the exact position and orientation of the sieve slits. The sieve slits were inserted for optics runs, and retracted for any high beam current run, including all production runs.

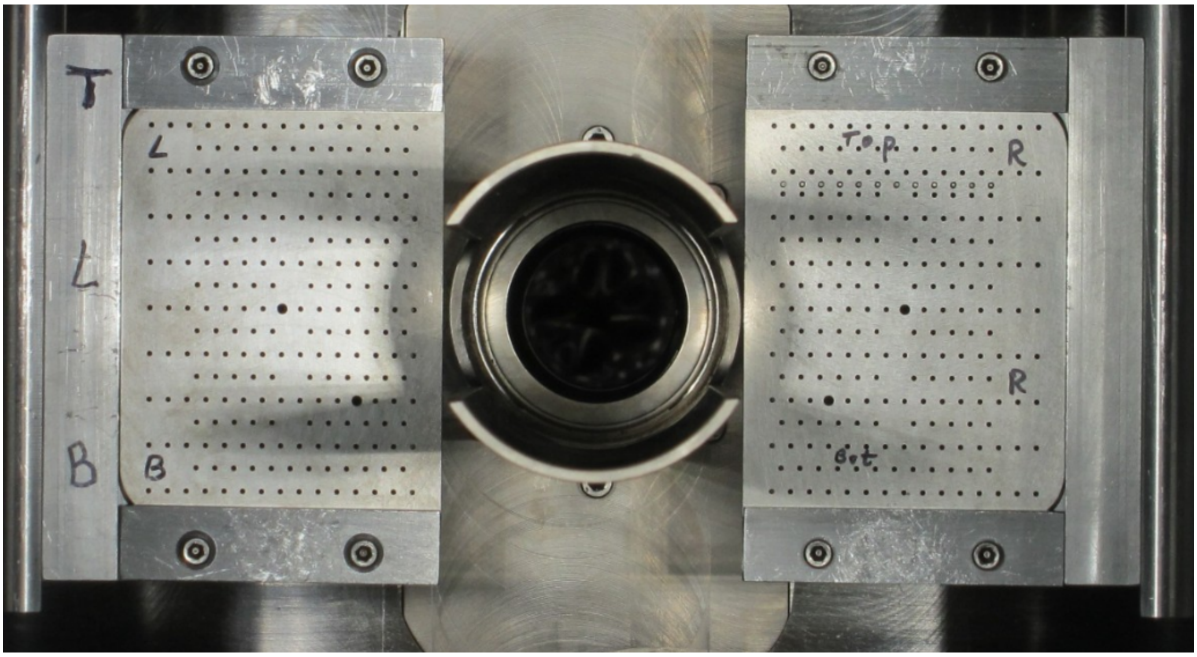

Figure 3.14: Photograph of Sieve slits inserted before APEX optics run. Left side shows sieve before LHRS entrance marked with 'L', right side shows sieve before RHRS entrance marked with 'R'.

Chapter 4

Detector Calibration and Analysis

The ultimate aim of the APEX analysis is to produce an invariant mass spectrum and perform a peak search for a dark photon, either finding a peak or providing a lower limit for ϵ^2 in the search mass range. Several steps had to be performed before obtaining a final invariant mass spectrum. These steps are taken in order to ensure accuracy of the invariant mass obtained, maximise the ratio of signal to background in the final event sample and to optimise the invariant mass resolution achieved. The raw data from detector ADC and TDC channels is stored in CODA format. The Hall A Analyzer [77], a C++, object-orientated framework built on top of ROOT [78], was used to 'replay' the CODA files. This processed the data, performing various algorithms (removal of pedestals, tracking algorithm, path reconstruction etc) to obtain final variables: track positions, total hits in detectors, track times, reconstructed positions etc, which were stored in a ROOT file. Some of these processes require calibrated inputs, part of the analysis described in this chapter was to reliably determine these values.

The primary analysis steps taken in order to produce the final invariant mass spectrum are detailed below:

- Particle Identification (PID): used to discriminate electrons (LHRS) or positrons (RHRS) from pion or muon backgrounds. PID involved both the Cherenkov detector and calorimeters on both arms, for which PID cuts were optimised.
- Coincidence Timing: defined by difference in S2 time between arms. True coincidence events should have correlated coincidence time. A cut can thus be placed on coincidence time to reduce the number of accidental coincidence events between arms. Several offsets and corrections were tested to achieve optimal timing resolution.

- Beam position: BPMs and raster information were used to determine beam position at target. Calibration procedures were used to ensure an accurate beam position.
- VDC tracking: algorithm used to construct tracks and determine positions and angles. APEX ran with a high beam current resulting in high rates in the LHRS VDC. Along with the regular calibrations for the VDC, modifications were made to the tracking algorithm to reduce accidentals and ensure well-constructed tracks.
- HRS Optics: used to project track coordinates from VDC back to coordinates at the target. The angular and momentum resolutions determine the invariant mass resolution, the vertex reconstruction is used as a cut. The optics matrices were optimised to minimise the angular and vertex resolutions.

4.1 Particle Identification

Particle Identification is important in the APEX analysis in order to minimise the portion of pion (and to a lesser extent muon) contamination contributing to the final invariant mass spectrum. PID for APEX was performed by a combination of Cherenkov and calorimeter detectors on both arms. To ensure accuracy both detectors had to be calibrated, after which the PID cut levels were tested to measure PID efficiency.

4.1.1 Cherenkov Detector

As described in section 3.5.2, the Cherenkov detectors on both arms have ten channels. As each of these are read via PMT the pedestal and gains for each had to be calibrated. Each channel read out via ADC (or FADC) has a different ADC-dependent electronic background referred to as the pedestal. This is present regardless of any signal from the PMT and should thus be removed for physics analysis. This could be achieved by taking 'pedestal runs' with no signal and extracting a pedestal from the ADC signal (via a simple Gaussian fit).

The signal from the Cherenkov detector is taken as the sum of all ten channels, so each channel must be calibrated to give the same response. After pedestal-subtraction each channel should have a prominent peak above zero corresponding to the single photo-electron (SPE) peak, which can be fitted with a Gaussian function. The calibration is carried out using a gain factor to align the mean of the SPE peak of all channels. All channels were set to have a SPE peak at 300 counts:

$$G_i = \frac{300}{\mu_i^{cer(ps)}}, \tag{4.1}$$

where G_i is the gain of the i$^{\text{th}}$ channel and $\mu_i^{cer(ps)}$ is the fitted centre of the SPE peak for channel i (pedestal-subtracted ADC spectrum).

4.1.2 Calorimeter

The calorimeters on the left and right HRS arms were read out via either FADC (LHRS) or ADC (RHRS). Thus each channel had a pedestal that could be calibrated as described in section 4.1.1. The calibration of the gain for each channel, however, differs from the Cherenkov detector and must involve the sum of ADC signals from multiple channels. The overall energy, E_i, for an event i in a calorimeter can be described as a sum over N blocks:

$$E_i = \sum_j^N G_j A_{ij}, \tag{4.2}$$

where A_{ij} are the pedestal subtracted ADC values for channel j and event i, and G_j are the gain coefficients which must be calibrated for each channel. This calibration can be achieved by forming a χ^2 between the calorimeter energy and the track momentum, p_i, (returned from optics reconstruction of the VDC track) over many (O) events:

$$\chi^2 = \sum_i^O \Big(\sum_j^N G_j A_{ij} - p_i \Big)^2. \tag{4.3}$$

This was minimised using Minuit in ROOT [79]. An alternative method using differentiation to obtain a set of linear equations was tested for a previous HRS experiment. Both methods were found to give similar results and found to be stable when given different initial values for the G_j coefficients and when the step size was varied [80].

4.1.3 PID Efficiency

For APEX the purpose of PID is to maximise the ratio of $e^{+(-)}$ to unwanted background, primarily pions, with smaller contributions from muons and cosmic ray particles. Cuts placed on both the calorimeters and the Cherenkov detectors for each arm can be used to discriminate $e^{+(-)}$ from background. The standard method of determining the cut level and efficiency of both PID detector systems involves using one detector to determine a 'clean' sample of electrons (or positrons) and pions (and muons) and then testing the efficiency of the other detector in discriminating these samples successfully. Depending on experimental kinematics, however, it is possible for a number of events to consist of particles that produce a signal in the Cherenkov detector and a successful trigger but register no signal in the Calorimeter. This effect was less prominent for APEX but has been observed and studied in other Hall A experiments using the HRSs including the GMp measurement [81]. These events can be distinct from those which passed through both detectors and due to the relative efficiencies of both detectors only produced a signal in the Cherenkov detector. This would then give an artificially low result for the calorimeter efficiency.

An analysis of the PID efficiency of the Cherenkov detector and calorimeter of both arms was undertaken. In addition to any PID cuts used for the PID analysis, other cuts were placed to ensure at least one track was formed in the VDC and basic cuts were placed on the acceptance (1D cuts on θ_{tg}, ϕ_{tg} and δp distributions, simpler versions of acceptance cuts described in section 4.6). Tight PID cuts were placed on one detector to produce samples of $e^{+(-)}$s and pions (and muons) for which the electron efficiency, ϵ_e, and pion rejection efficiency, ϵ_π were then tested. The general expressions for ϵ_e and ϵ_π are given by equations 4.4 and 4.5 respectively:

$$\epsilon_e = \frac{N_e^{pass}}{N_e^{sample}}, \tag{4.4}$$

$$\epsilon_\pi = 1 - (\frac{N_\pi^{pass}}{N_\pi^{sample}}), \tag{4.5}$$

where N^{sample} is the number of events in the sample and N^{pass} is the number of events in the sample surviving the PID cut.

For examining the PID efficiency and optimal cut level of the Cherenkov detector, samples of 'pions' (in addition to 'muons' for RHRS) and 'electrons' ('positrons' for RHRS) were taken from the calorimeter and tested against different levels of Cherenkov detector cuts. For the LHRS the sample cuts from the calorimeter can be seen in the left plot of figure 4.1 where red lines indicate electron cuts and blue lines pion cuts. These sample cuts are designed to produce as clean samples as possible. The right plot of figure 4.1 shows the electron sample (red) and pion sample (blue) Cherenkov detector sum distributions. As expected it can be observed that the pion sample peaks at low Cherenkov detector sum values and the electron sample leaves a much greater signal. From the Cherenkov detector sum distributions the electron efficiency and pion rejection efficiency can be calculated. The optimal cut level is shown in the right plot, which was found to be Cherenkov detector sum > 650. For the RHRS, the same process was undertaken as illustrated in figure 4.2. The primary difference is the presence of μ^+s in the RHRS that are also selected with the π^+s as part of the background. The optimal cut level for the RHRS was determined to be Cherenkov detector sum > 1000.

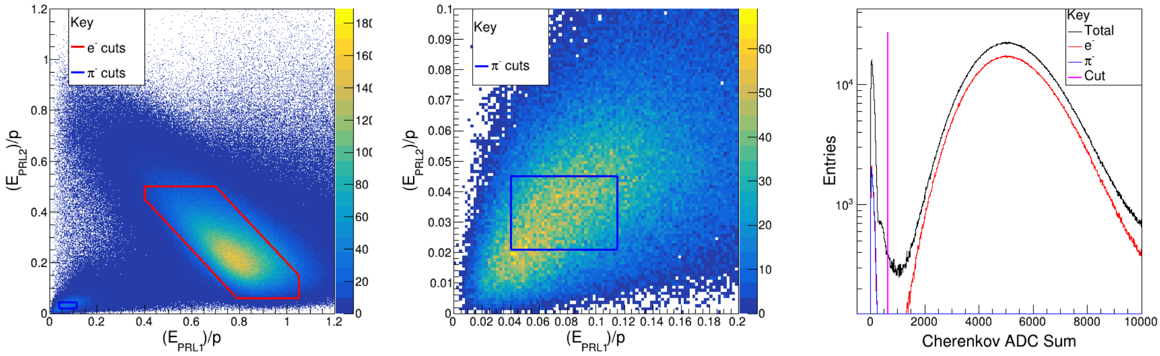

Figure 4.1: Cherenkov detector scan plots for the LHRS. The left plot shows sampling from calorimeter (red lines are e^- cuts and blue lines π^- cuts). The centre plot shows sampling from the calorimeter with restricted axes to illustrate the π^- cuts (blue rectangle). All energies are scaled to track momentum. Right plots shows distribution of samples in Cherenkov detector, with the pink line illustrating the cut.

A similar process is carried out to test the PID efficiency and cut level for the calorimeter. In the top-left plot of figure 4.3 the cuts used to sample from the Cherenkov detector (LHRS) can be seen (all energies in this figure are scaled to track momentum). The e^- and π^- samples obtained from the Cherenkov detector were plotted in E_{PRL1}, the energy from PRL1 (shown in the top left plot of figure 4.3), and $E_{PRL1} + E_{PRL2} = E_{tot}$, the sum of the energies deposited in PRL1 and PRL2 (shown in the bottom-left plot of figure 4.3). As discussed, a pion sample obtained from the Cherenkov detector can contain contamination. This can be seen in the top-right and bottom-left plots of figure 4.3 where the π^- distribution has a flat continuation into higher energy contributions and the 'true' π^- peak (illustrative) is highlighted with a green dashed line. The bottom-right plot displays the final PRL cuts.

Figure 4.4 shows the same calorimeter scan process for the RHRS, where e^+ contamination is present in the π^+, μ^+ distribution but to a lesser extent than the effect in

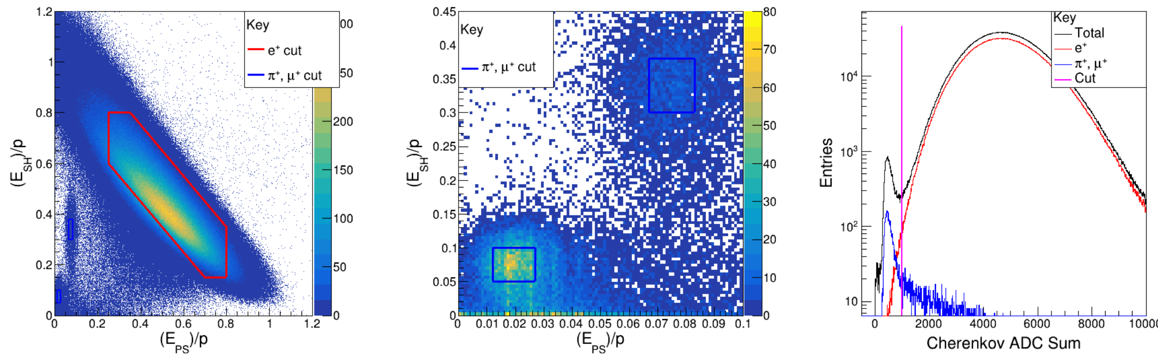

Figure 4.2: Cherenkov detector scan plots for the RHRS. The left plot shows sampling from calorimeter (red lines are e^+ cuts and blue lines π^+, μ^+ cuts). The centre plot shows sampling from the calorimeter with restricted axes to illustrate the π^+ and μ^+ cuts (blue rectangles). All energies are scaled to track momentum. Right plots shows distribution of samples in Cherenkov detector, with the pink line illustrating the cut.

the LHRS. This known contamination in the π^- (LHRS) and π^+, μ^+ (RHRS) samples from the Cherenkov detector will result in the efficiencies obtained from this method being less accurate. The efficiencies can be calculated by a different method, given that the calorimeter can provide clean samples and therefore reliable Cherenkov detector efficiencies [80]. The number of overall events that pass the track cuts, N_0, the number of events passing Cherenkov detector and track cuts, N_{Ch}, the number of events passing calorimeter cuts and track cuts, N_{Cal}, and the number of events passing Cherenkov detector, calorimeter and track cuts, N_{Cal+Ch}, can be combined with the Cherenkov detector efficiencies to calculate PID efficiencies for the calorimeter. This is described by equations 4.6-4.9:

$$N_0 = N_e + N_\pi, \tag{4.6}$$
$$N_{Ch} = \epsilon_e^{Ch} N_e + (1 - \epsilon_\pi^{Ch}) N_\pi, \tag{4.7}$$
$$N_{Cal} = \epsilon_e^{Cal} N_e + (1 - \epsilon_\pi^{Cal}) N_\pi, \tag{4.8}$$
$$N_{Cal+Ch} = \epsilon_e^{Ch} \epsilon_e^{Cal} N_e + (1 - \epsilon_\pi^{Cal})(1 - \epsilon_\pi^{Ch}) N_\pi. \tag{4.9}$$

These equations have four unknown parameters, with six known, and can thus be solved to give the calorimeter efficiencies (and the number of electron and pion events).

The PID cuts for the calorimeter are made on energy over track momentum (E/p) and are given in natural units. The final cuts for the LHRS calorimeter were $E_{PRL1} > 0.20$, $(E_{PRL1} + E_{PRL2}) > 0.70$ and $(E_{PRL1} + E_{PRL2}) < 1.4$ (this last cut is included to remove higher energy events which form a linear background distinct to the main peak of the electron energy distribution, it is not included in efficiency calculations to make them comparable to previous Hall A analyses). The equivalent cuts for the RHRS were $E_{PS} > 0.20$, $(E_{PS} + E_{SH}) > 0.72$ and $(E_{PS} + E_{SH}) < 1.25$. Assuming independence of the detectors the overall PID efficiencies can then be calculated as the product of the separate detector efficiencies as in equations 4.10-4.11:

$$\epsilon_e^{PID} = \epsilon_e^{Cal}\epsilon_e^{Ch}, \tag{4.10}$$
$$\epsilon_\pi^{PID} = 1 - (1 - \epsilon_\pi^{Cal})(1 - \epsilon_\pi^{Ch}). \tag{4.11}$$

This gave final combined PID efficiencies of $\epsilon_e^{PID} = 0.98$ and $\epsilon_\pi^{PID} = 0.97$ for the LHRS and $\epsilon_e^{PID} = 0.98$ and $\epsilon_\pi^{PID} = 0.99$ for the RHRS.

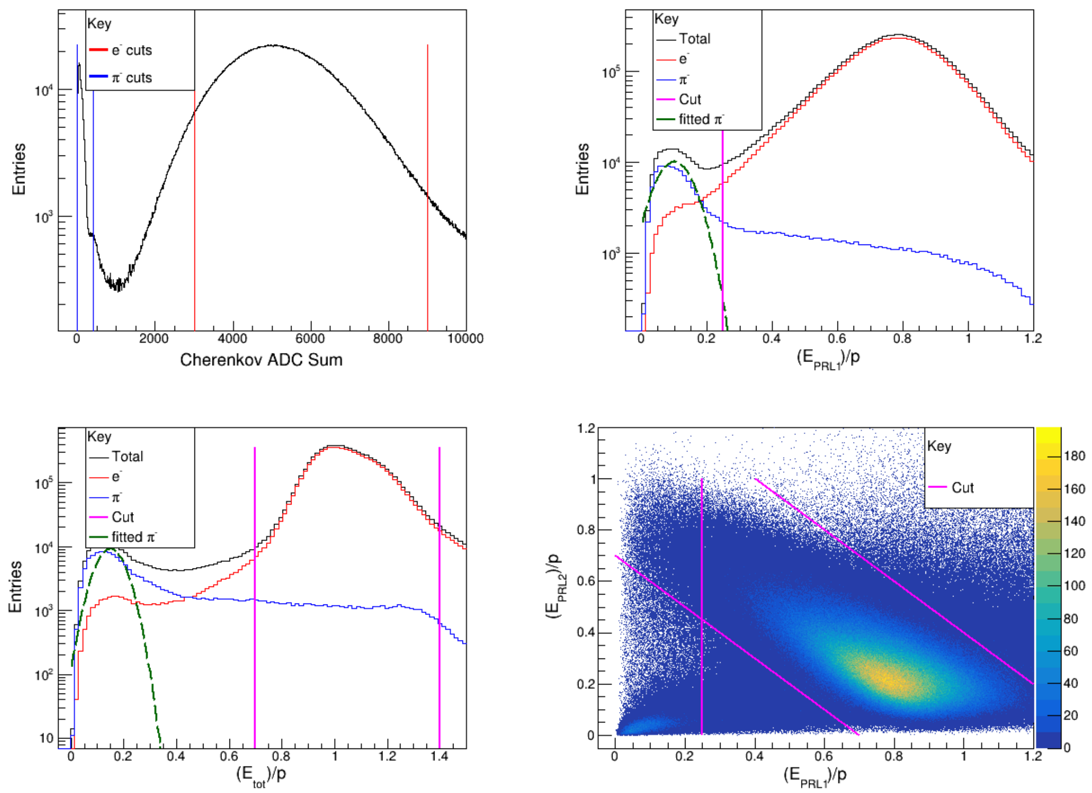

Figure 4.3: Calorimeter scan plots for LHRS. Top-left plot shows sample cuts from Cherenkov detector. Top-right and bottom-left plots show PRL energy distributions (scaled to track momentum) of π^-s (blue) (with 'true' peak fitted and displayed with a green dashed line) and e^-s (red). E_{tot} is sum of E_{PRL1} and E_{PRL2}. Bottom-right plot shows position of final cuts.

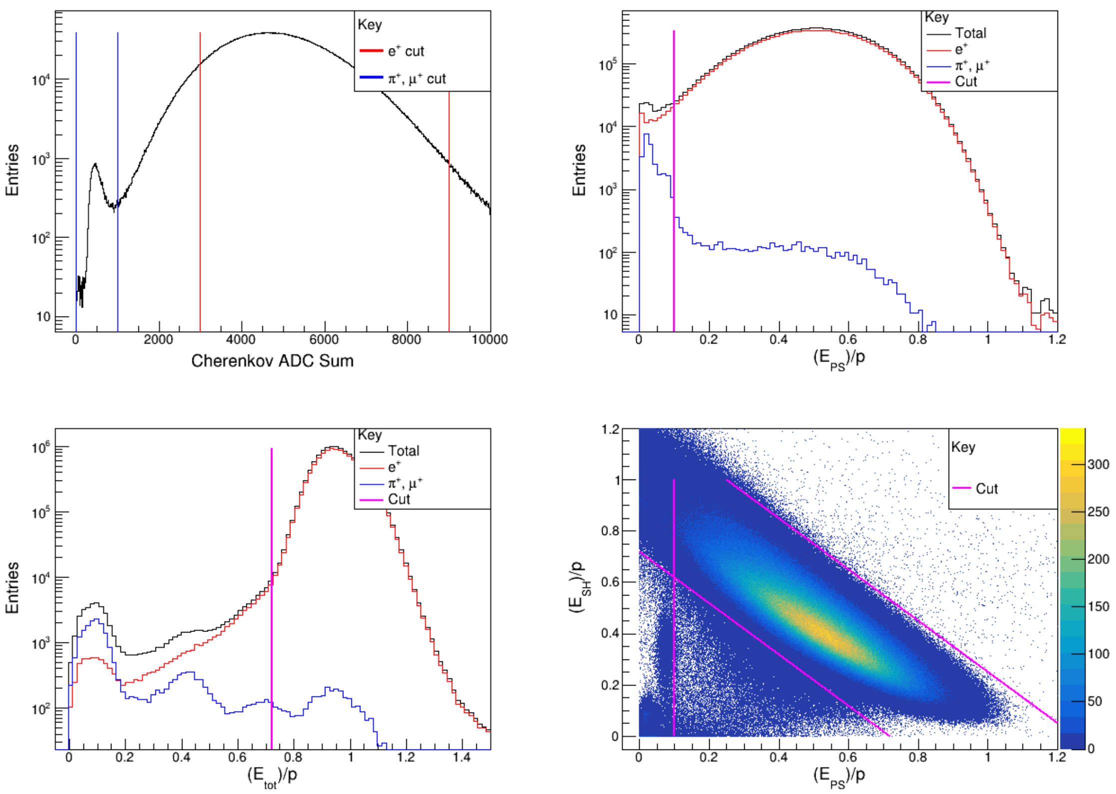

Figure 4.4: Calorimeter scan plots for RHRS. Top-left plot shows sample cuts from Cherenkov detector. Top-right and bottom-left plots show calorimeter energy distributions (scaled to track momentum) of π^+s & μ^+s (blue) and e^+s (red). E_{tot} is sum of E_{PS} and E_{SH}. Bottom-right plot shows position of final cuts.

4.2 Coincidence Timing

For coincidence measurements taken with both HRS arms coincidence timing between the arms is important in separating true coincidence events from accidental hits in both arms which happen to form a coincidence trigger. True coincidence events with both the e^- in the LHRS and e^+ in the RHRS coming from the same reaction vertex in the target form a coincidence peak in the timing spectrum over the accidental background. The goal of coincidence timing optimisation is to improve the timing resolution and minimise the width of the true coincidence peak. The coincidence time, T_{coinc}, in the HRSs is defined as the difference in time between the LHRS S2 (T_i^{LHRS} for i$^{\text{th}}$ paddle) and RHRS S2 (T_j^{RHRS} for j$^{\text{th}}$ paddle):

$$T_{coinc} = T_i^{LHRS} - T_j^{RHRS}, \tag{4.12}$$

$$T_{coinc} = \frac{(T^{LHRS}_{L,i} + T^{LHRS}_{R,i})}{2} - \frac{(T^{RHRS}_{L,j} + T^{RHRS}_{R,j})}{2}. \tag{4.13}$$

Here the time for one arm is taken as the mean of the times in the left and right PMTs of a paddle ($T^{LHRS}_{L,i}$ and $T^{LHRS}_{R,i}$ for the LHRS, $T^{RHRS}_{L,j}$ and $T^{RHRS}_{R,j}$ for the RHRS). To optimise the coincidence timing between arms the timing factors affecting the reported time from each S2 paddle must be considered.

When a charged particle traverses an S2 paddle, the light emitted travels to both ends of the paddle and is collected by PMTs as shown in figure 4.5. The analogue pulse created by the PMT is then sent to a circuit, discriminated and sent to a TDC. Labelling the time of the hit in S2 for paddle i as $T_{S2,i}$, the times recorded in the TDCs for the left ($T_{L,i}$) and right ($T_{R,i}$) PMTs of the paddle can be expressed as:

$$T_{L,i} = T_0 - (T_{S2,i} + \frac{L_0/2 - y_i}{c_n} + \Delta T_{L,i}), \tag{4.14}$$

$$T_{R,i} = T_0 - (T_{S2,i} + \frac{L_0/2 + y_i}{c_n} + \Delta T_{R,i}). \tag{4.15}$$

Here T_0 is the time of the common stop of the TDC (related to the trigger), y_i is the distance of the hit position from the centre of the paddle (positive y goes to the left as in figure 4.5), L_0 is the full length of the paddle, c_n is the speed of light in the scintillator and $\Delta T_{L,i}$, $\Delta T_{R,i}$ are the timing offsets for the left and right PMT of the ith paddle respectively. Calibration of the S2 scintillators thus requires determining the various contributions to ΔT_L and ΔT_R, to ensure that the coincidence time between arms is not dependent upon which paddle is hit.

The correction to the S2 left and right PMT times can be split into several contributions that were found to be significant in the APEX analysis:

$$T_{L(R),i} = T'_{L(R),i} - \Delta T_{L(R),i} - \Delta T_{pl,L(R)} - \Delta T_J, \tag{4.16}$$

where $T'_{L(R),i}$ is the uncorrected TDC time, $\Delta T_{L(R),i}$ is the individual electronic paddle offset, $\Delta T_{pl,L(R)}$ is the path-length correction and ΔT_J is the jitter correction.

4.2.1 S2 Timing Offsets

In Hall A two methods have been used to calibrate the $\Delta T_{L(R),i}$ offsets: using the Time of Flight (TOF) between S0 and S2 and an alignment method between adjacent paddles.

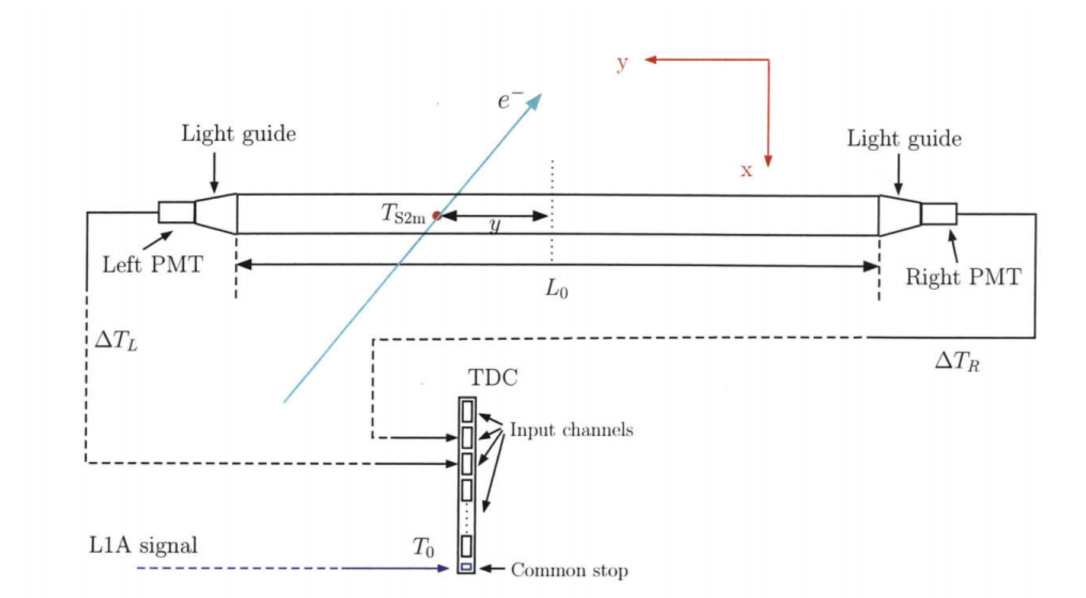

Figure 4.5: Electron passing through S2, creating signals in Left PMT and right PMT with different timing offsets. The transport coordinate system is shown by the red axes. The L1A signal and the common stop its generated are shown beneath the scintillator. [82]

Both of these methods utilise the time difference between left and right PMTs of the same paddle. Both were tested for APEX and the alignment method was found to result in a superior timing resolution.

Taking the difference in time between the two PMTs on the i$^{\text{th}}$ paddle gives:

$$T_{L,i} - T_{R,i} = \frac{2y}{c_n} + (\Delta T_{R,i} - \Delta T_{L,i}). \tag{4.17}$$

From 4.17, $(\Delta T_{R,i} - \Delta T_{L,i})$ can be extracted by plotting $(T_{L,i} - T_{R,i})$ against the VDC track projection along the paddle (as a proxy for y) for each paddle and taking the intercept of a linear fit. The slope of this fit should be given by $\frac{2}{c_n}$. The alignment method looks at events for which adjacent paddles in S2 registered hits (with those hits being close in time) as seen in figure 4.6. The difference in time between paddles for such events can be described as:

$$(T_{L,i+1} + T_{R,i+1}) - (T_{L,i} + T_{R,i}) = (T_{s2,i+1} - T_{s2,i}) - (\Delta T_{L,i+1} + \Delta T_{R,i+1}) - (\Delta T_{L,i} + \Delta T_{R,i}). \tag{4.18}$$

For large distributions of such events for a pair of paddles, it can be assumed that the difference in the T_{s2} terms in 4.18 $(T_{s2,i+1} - T_{s2,i})$ for the adjacent paddles forms a

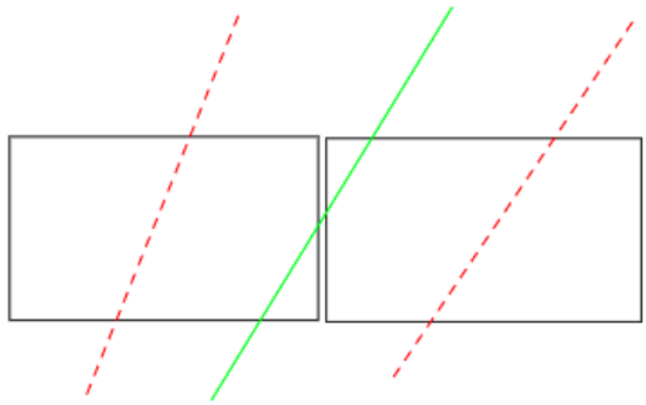

Figure 4.6: Adjacent S2 paddles. Green track of interest for adjacent paddle alignment technique. Dotted red lines show tracks which only pass through one paddle.

narrow distribution around zero. If this is neglected then the relation simplifies to:

$$(T_{L,i+1} + T_{R,i+1}) - (T_{L,i} + T_{R,i}) = (\Delta T_{L,i+1} + \Delta T_{R,i+1}) - (\Delta T_{L,i} + \Delta T_{R,i}). \tag{4.19}$$

The alignment method relies on the assumption that the relative difference between times in different paddles is important, not the absolute measurement. With this assumption one of the PMT offsets (left PMT of eighth paddle) can be set to zero. Equations 4.17 and 4.19 can then be combined to obtain values for all timing offsets iteratively starting with the eighth paddle and its direct neighbours.

4.2.2 Path-Length Corrections

Variations in path-length traversed by a particle in the spectrometer will result in an altered time recorded at S2. These variations can be categorised by differences in θ_{fp}, ϕ_{fp} and x_{fp}, (FCS coordinates as defined in section 3.5.5) and will widen the timing distribution of particles originating from the same vertex. These corrections for both arms can be modelled as second order polynomials and the overall path-length correction expressed as:

$$\Delta T_{pl} = p_{t_1}\theta_{fp} + p_{t_2}\theta_{fp}^2 + p_{x_1}x_{fp} + p_{x_2}x_{fp}^2 + p_{p_1}\phi_{fp} + p_{p_2}\phi_{fp}^2. \tag{4.20}$$

Plotting the coincidence time versus the relevant path length variables can be used to extract the values of the coefficients (p_{t_i}, p_{x_i}, p_{p_i}) through a second order polynomial fit. This can be seen in figures 4.7 and 4.8 for the LHRS and RHRS respectively. This was done sequentially, starting with fitting and then implementing a correction for θ_{fp}, followed by x_{fp} and finally ϕ_{fp}. For this analysis relations and corrections were found for both θ_{fp} and ϕ_{fp} but no simple relation or subsequent correction could be found for x_{fp}.

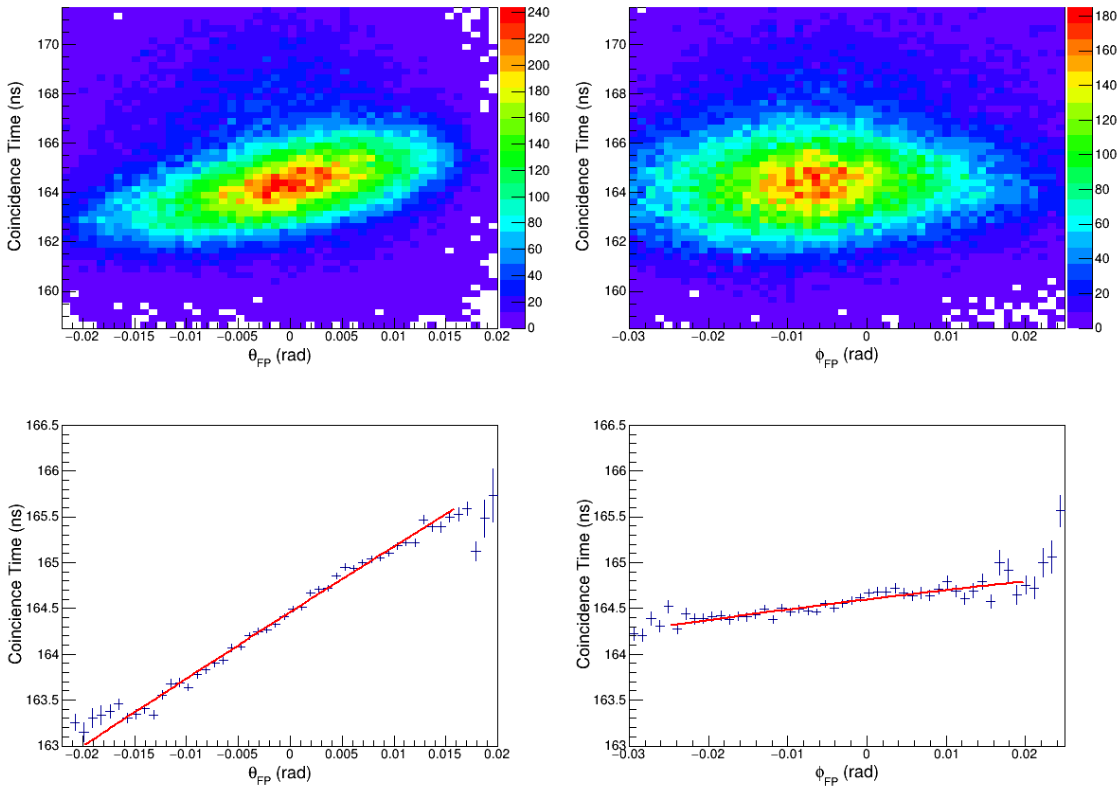

Figure 4.7: LHRS S2: coincidence time versus path length variables (defined in FCS). Path length variables from left to right are: θ_{fp} and ϕ_{fp}. The top plots show 2D histograms, the bottom plots show the means of Gaussian fits of the coincidence timing distributions over small ranges in θ_{fp} or ϕ_{fp}, with the red line showing the fit used to extract the correction.

4.2.3 Jitter Correction

Timing jitter in a discriminator is caused by signal noise and can result in a signal crossing the discriminator threshold away from the 'true' time (if there was no signal noise). For the HRSs the jitter correction can be described by:

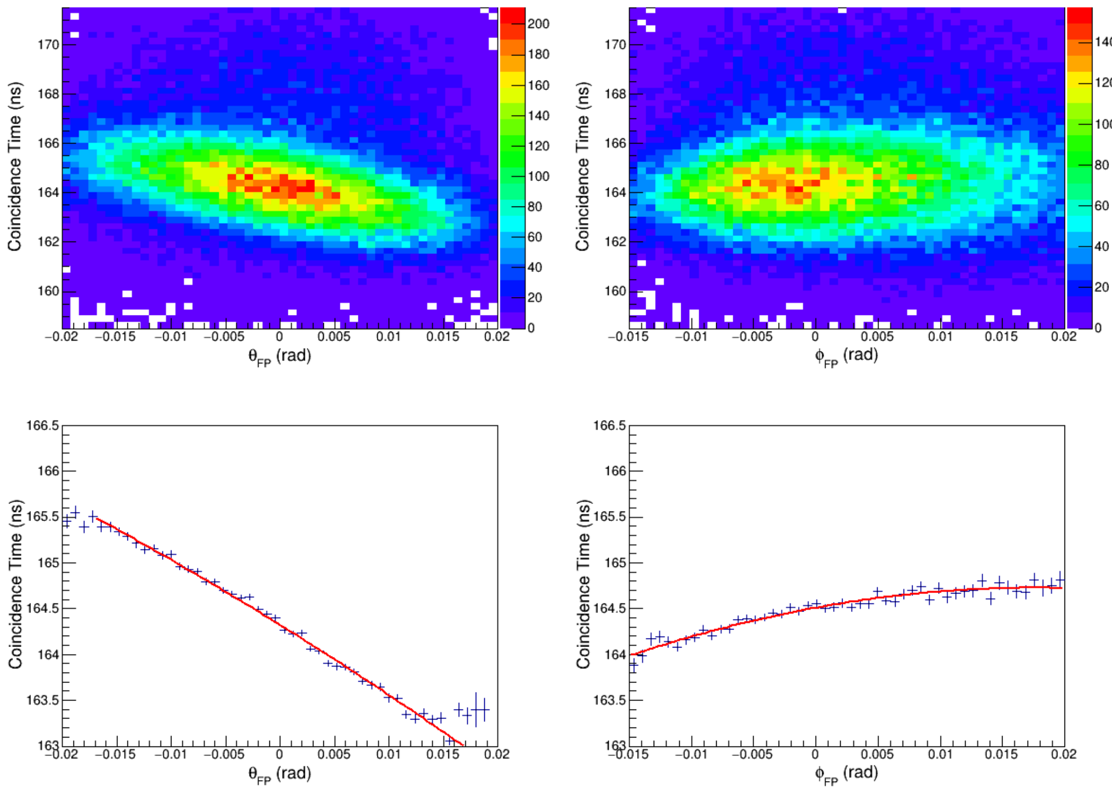

Figure 4.8: RHRS S2: coincidence time versus path length variables (defined in FCS). Path length variables from left to right are: θ_{fp} and ϕ_{fp}. The top plots show 2D histograms, the bottom plots show the means of Gaussian fits of the coincidence timing distributions over small ranges in θ_{fp} or ϕ_{fp}, with the red line showing the fit used to extract the correction.

$$\Delta T_j = \frac{T_{L_{L1a,remote}} - T_{R_{L1a,remote}}}{2}, \tag{4.21}$$

where $T_{L_{L1a,remote}}$ is the time recorded for the L1A (Level 1 Accept) signal in the LHRS and $T_{R_{L1a,remote}}$ is the time recorded for the L1A signal in the RHRS. For APEX the RHRS controlled the triggering of both arms. Equation 4.21 gives the difference in the L1A signal time in both arms, and is used as a correction. The L1A signal is used to form the common stop for the TDCs, thus differences in L1A signal time between arms would result in a divergence from the true coincidence time for an event.

4.2.4 Coincidence Peak

The resulting resolution of the coincidence timing peak was $\sigma_{ct} \sim 0.62$ ns (averaged over all runs), with an example for run 4468 shown in figure 4.9 (with additional cuts on there only being only one hit in each scintillator to provide a cleaner sample). This can be compared to a resolution of $\sigma_{ct} \sim 1.53$ ns before the implementation of the offset, path-length and jitter corrections described. Due to slight alterations of the relative timing between the two arms, the run period was split into three sections where the location of the timing peak moved (as shown in table 4.1). In the final invariant mass analysis a 3σ cut around the peak was used.

Run Period	Run Numbers	Timing Peak (ns)
First	3977->4363	204.4
Intermediate	4374->4407	200.5
Final	4425->5006	202.38

Table 4.1: Coincidence Peak Times throughout Run Period

The portion of accidental events which survive the coincidence timing cut can be determined from a fit of the coincidence timing peak plus background (as in figure 4.9). This is done after all other cuts have been applied. The portion of accidentals remaining in the final event sample is known as the 'accidental fraction'. For APEX, this was 11.9% and is needed for the calculation of the experimental reach in ϵ^2 (as detailed in section 5.5.1).

4.2.5 Sideband Subtraction

It can be observed from the coincidence timing spectrum (figure 4.9) that a fraction of the events surviving a timing cut will come from accidental coincidences between arms. When examining production data it is important to consider these accidental coincidence events that remain in the final event sample. Though these accidental events should be disproportionately removed by other cuts (PID, track cuts etc) a fraction will still survive in the ultimate event sample. To account for this when considering distributions in the production data a technique called 'sideband subtraction' can be used. This technique accounts for the background by taking a distribution in some variable corresponding to events from the 'prompt' region (around the peak) and subtracting a distribution of events from 'random' regions (or sidebands). The

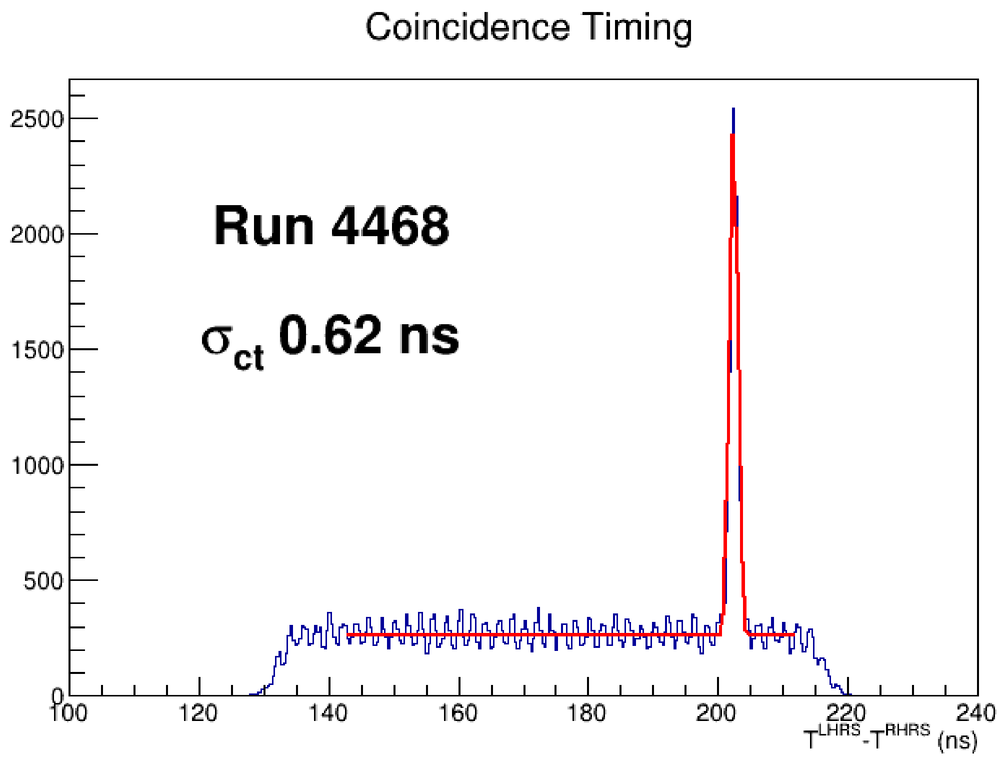

Figure 4.9: Coincidence time for a production run (4468) with fit of true coincidence peak with σ_{ct} = 0.62 ns. Gaussian fit is used for peak.

definitions of these regions are illustrated in figure 4.10, a plot of the coincidence timing (without the additional timing cuts described for figure 4.9), which shows the prompt timing region (the 3σ region around the peak defined in 4.2.4) as red cuts and the random timing regions (or sidebands) as blue cuts. The sideband events correspond to accidental coincidences and their subtraction is assumed to account for the effect of accidental coincidences that occur in the peak region. The sideband subtraction is scaled by the relative widths of the random regions, which are wider in order to have greater statistics.

The effect of sideband subtraction can be seen in several distributions and is discussed for the reconstructed z vertex in section 4.5.4, and the momentum in section 4.5.5. An example of sideband subtraction is provided in Figure 4.11, which shows single arm z vertex positions. The left hand plots of figure 4.11 show the distributions that survive the prompt and random (sideband) timing cuts, with the random distribution scaled as described previously. It can clearly be seen how these distributions differ: the random distribution is relatively flat compared to the prompt distribution which is greater at lower values of z (corresponding to downstream targets). The right

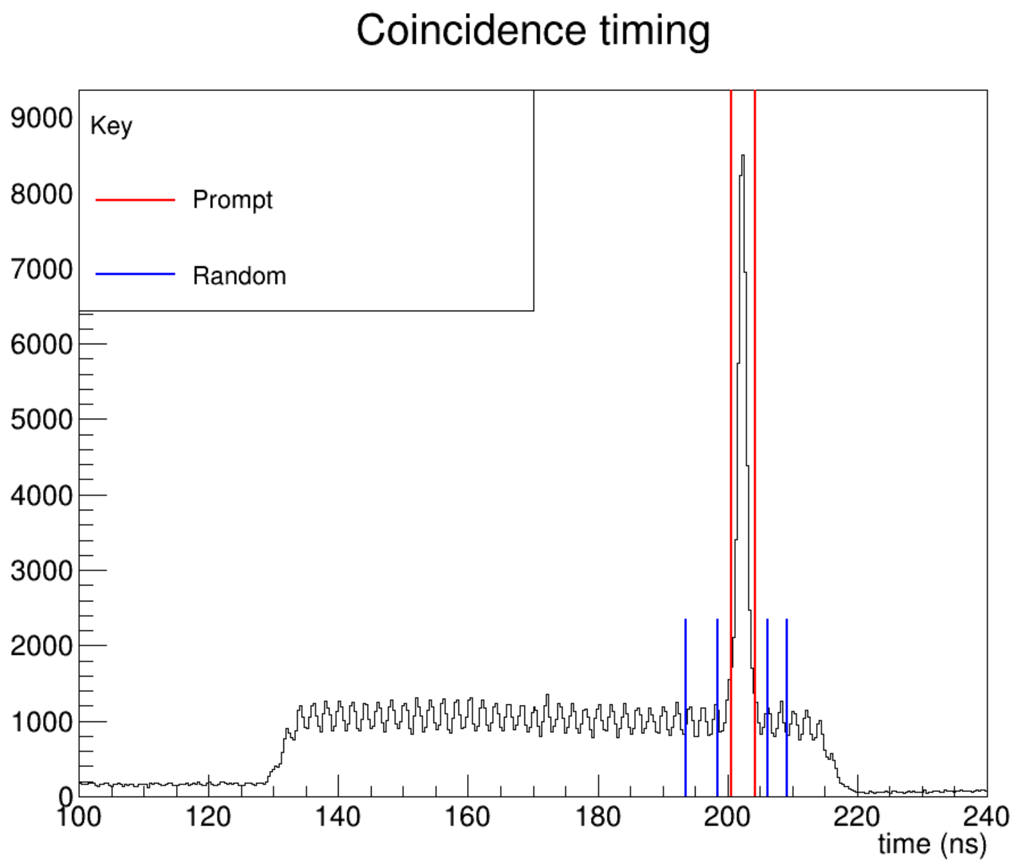

Figure 4.10: Coincidence time for a production run (4468) with cuts for prompt (red) and random (blue) regions.

hand plots of figure 4.11 show the effect of subtracting the sidebands, removing the distinct distribution from random coincidences.

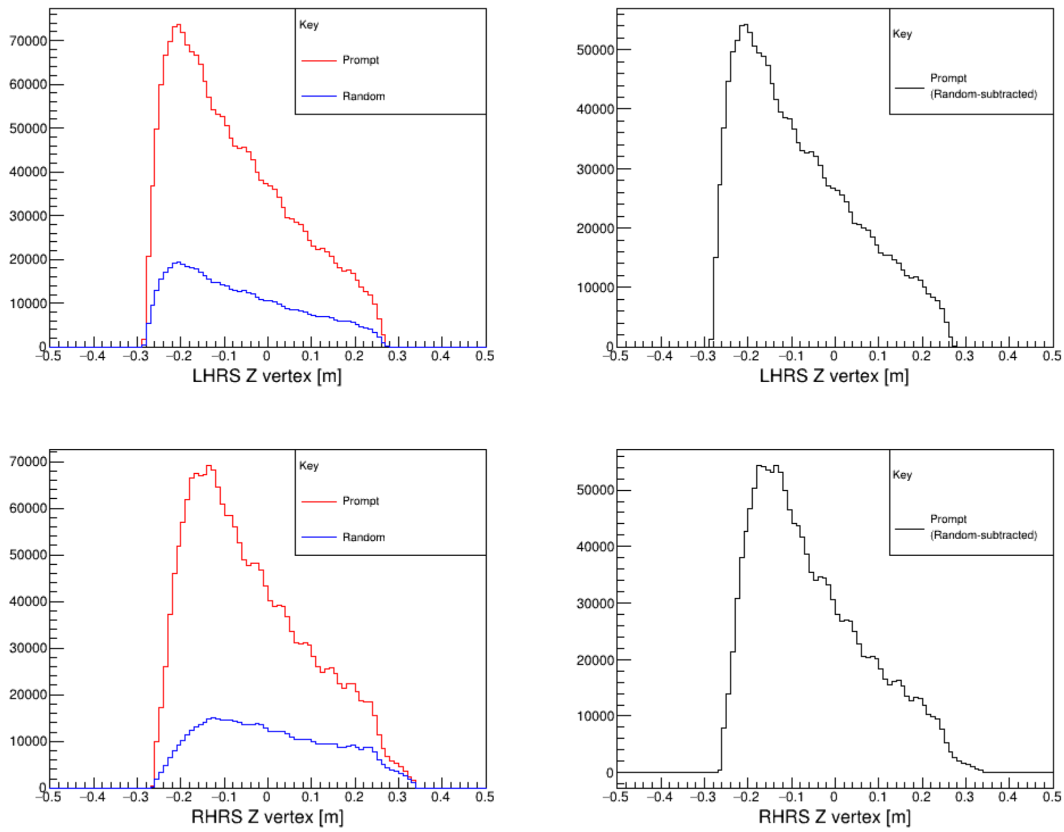

Figure 4.11: Single-arm reconstructed z vertex plots. Top - LHRS: Left plot shows the distribution of events from prompt (red) and random (blue) timing cuts, Right plot shows the prompt distribution after sideband subtraction. Bottom - RHRS: same plots as described for LHRS.

4.3 Beam Position

For APEX knowledge of the beam position is needed to determine the position of the reaction vertex and thus the target variables used in calculating the invariant mass. Precise calibration of the beam position is required and necessitates two stages: calibration of the BPMs and then calibration of the raster.

The position obtained from BPMA(B) is described by:

$$\begin{bmatrix} x \\ y \end{bmatrix}_{BPMA(B)} = \begin{bmatrix} C_{x,u} & C_{x,v} \\ C_{y,u} & C_{y,v} \end{bmatrix} \begin{bmatrix} u \\ v \end{bmatrix}_{BPMA(B)} + \begin{bmatrix} C_{x,off} \\ C_{y,off} \end{bmatrix}_{BPMA(B)}, \tag{4.22}$$

where the final position $(x, y)_{BPMA(B)}$ is translated from the initial BPM values $(u, v)_{BPMA(B)}$ (described by equation 3.1), with calibrated scaling parameters, $C_{x(y),u}$, $C_{x(y),v}$, and offsets $C_{x(y),off}$. The BPM signals are read out via FADC and the initial BPM values $(u, v)_{BPMA(B)}$ are pedestal-subtracted. The process for calibrating these pedestals is the same as described for the Cherenkov detector in section 4.1.1.

The calibration of the BPMs was carried out based on a position measurement from the Hall A harp ('a scan'), as described in section 3.4.2. The harp scan results for a group of five runs is shown in figure 4.12 for BPMA and 4.13 for BPMB. Using the known position of the beam from the harp scanner (shown as grey markers on figures 4.12 and 4.13) and the measured current in the BPMs the values of the calibration parameters were determined. This was done via matrix inversion using values from all five harp scans.

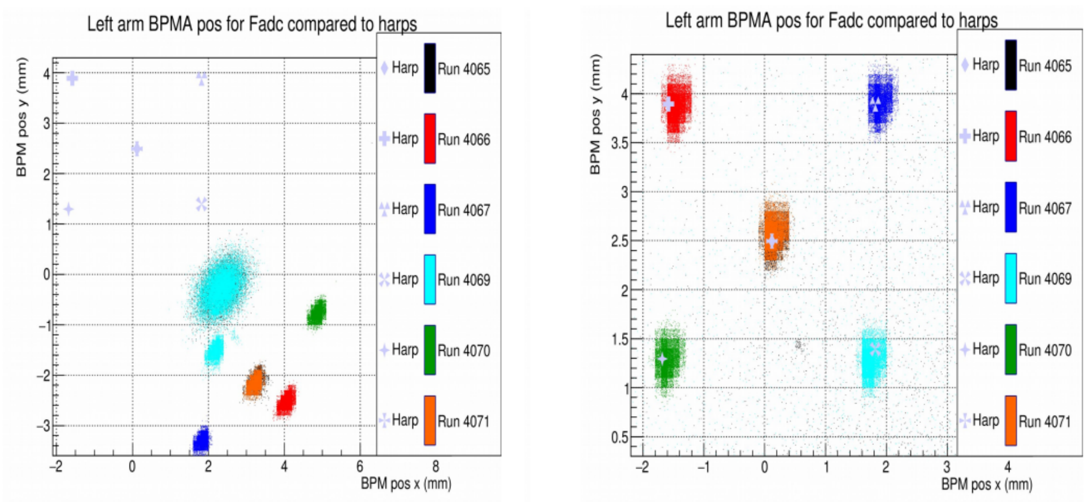

Figure 4.12: Illustration of BPMA calibration. Grey markers on plots indicate known position of beam as measured by harp scan. Left plot shows pre-calibration BPM positions and right plot shows post calibration BPM positions.

The information from the BPMs must be combined to obtain the position of the beam at the target:

$$\theta_{BPM} = \frac{x_{BPMB} - x_{BPMA}}{S_{BPM}}, \tag{4.23}$$

$$\phi_{BPM} = \frac{y_{BPMB} - y_{BPMA}}{S_{BPM}}, \tag{4.24}$$

$$x_{BPM} = x_{BPMB} + \theta_{BPM} S_{B,targ}, \tag{4.25}$$

$$y_{BPM} = y_{BPMB} + \phi_{BPM} S_{B,targ}, \tag{4.26}$$

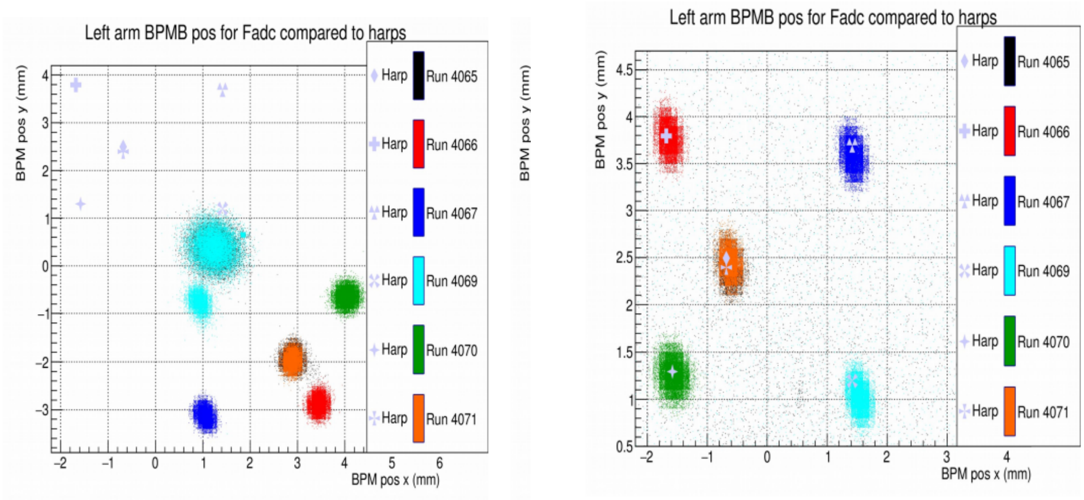

Figure 4.13: Illustration of BPMB calibration. Grey markers on plots indicate known position of beam as measured by harp scan. Left plot shows pre-calibration BPM positions and right plot shows post calibration BPM positions.

where S_{BPM} is the separation between the BPMs, $S_{B,targ}$ is the separation between BPMB and the target, $(x,y)_{BPM}$ is the position at target and $(\theta,\phi)_{BPM}$ is the direction of the beam derived from the BPMs. The position at target from the BPMs is used to calibrate the raster and used directly for some optics runs which were taken at a low beam current without a raster.

As described in section 3.4.3, APEX production runs used a raster to avoid damaging the target at high beam current. Equations 3.2-3.3 describe the translation from raster current to position at BPMA, BPMB and target. The calibration was performed by comparing the raster current and beam position from BPM distributions. The mean, $\mu_{I^{raster}_{x(y)}}$, and RMS, $\Delta I^{raster}_{x(y)}$, of the raster current is compared with the mean, $\mu_{x(y)_{BPM}}$, and width, $\Delta x(y)_{BPM}$, of the beam position from the BPMs:

$$A_{x(y)} = \frac{\Delta x(y)_{BPM}}{\Delta I^{raster}_{x(y)}}, \tag{4.27}$$

$$O_{x(y)} = \mu_{x(y)_{BPM}} - \mu_{I^{raster}_{x(y)}} A_{x(y)}. \tag{4.28}$$

Different values for O_x, O_y, A_x, A_y are obtained for the raster at BPMA, BPMB and target by comparing the raster current to the beam position from BPMs at these locations. The resulting uncertainty of the beam position at target has multiple contributions from the uncertainty on the pedestal for the BPMs, uncertainty in the calibration constants of the BPMs, uncertainties in BPM survey information and uncertainty in the raster calibration constants and has previously been determined to be ∼1-2 mm in position and ∼1-2 mrad in angle [66].

4.4 VDC Tracking

The VDCs on both HRS arms recorded the position and angles of particles, necessary for reconstructing the momentum of particles at the vertex as used in the invariant mass calculation. For APEX there was an additional challenge in VDC analysis of running at high rates in the LHRS which required modifications to the standard VDC algorithm.

A typical cluster of hits in one VDC plane is shown in figure 4.14. The known location and separation of the wires (4.24 mm) could be used to reconstruct tracks but this method would have per-plane spatial resolution on the order of the wire separation. Using the TDC time information recorded for each wire allows for superior resolutions to be achieved. This requires conversion of the times recorded into drift distances as in figure 4.14. These drift distances versus distance in the VDC plane (known for wires) can then be fitted to determine the 'crossover point' (where the track creating a cluster of hits crossed the VDC plane). The typical per-cluster position resolution achieved with this method for the Hall A VDCs is 225 μm FWHM (Full Width at Half Maximum) [65].

The time recorded by each wire is composed of several elements, the drift time, t_d, which can be converted to a drift distance and another component, the reference time or t_0, which takes into account the time of flight for a particle to travel to detectors forming a trigger, the time taken in trigger formation and the time it takes the signal from the wire to reach the TDC. To obtain t_d for the wire, t_0 must first be calibrated. An example of the TDC spectrum (VDC signal is recorded in common stop mode hence larger channels correspond to smaller times) for one wire can be seen in figure 4.15. The peak on the right side of the plot corresponds to particles that are close to the wire (where the field goes from parallel to quasi-radial [69]), this is where t_d goes to zero and thus where the offset t_0 is located. This peak is fitted with a Gaussian function and the time 1.4σ to the right of the peak is taken to be t_0. Groups of sixteen wires share a discriminator and are thus assumed to have the same t_0.

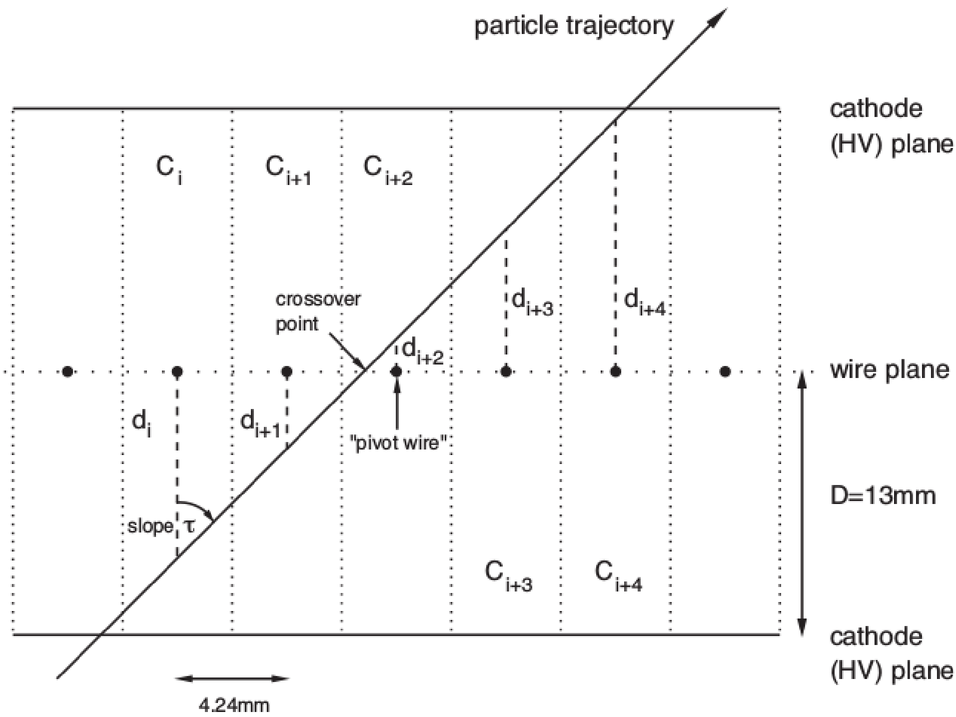

Figure 4.14: Cluster of five wire hits in a VDC Plane. The perpendicular drift distance from the i^th wire is denoted as d_i and the corresponding wire cell as c_i. The sense wires are separated by 4.24 mm. [65]

4.4.1 Drift Time to Distance Conversion

The relationship between drift time and perpendicular distance is nonlinear. This can be seen in figure 4.16 where the non-uniformity of the electric field near the wire results in larger mean drift velocities. The effect of the electric field non-uniformity in the wire cell on the drift lines (path of shortest time taken by drift electrons) can be seen in figure 4.17. Different methods of characterising this relationship between drift time and vertical distance have been employed. The current method in the Hall A Analyzer, used for this analysis, linearises the drift distances by using a third order polynomial with coefficients fitted to data [77] [83]. Alternative approaches that have been used are a third order polynomial with coefficients determined from a GARFIELD simulation [83] and a 'velocity look-up table' based on integration of the VDC wire TDC timing spectrum [69] [84].

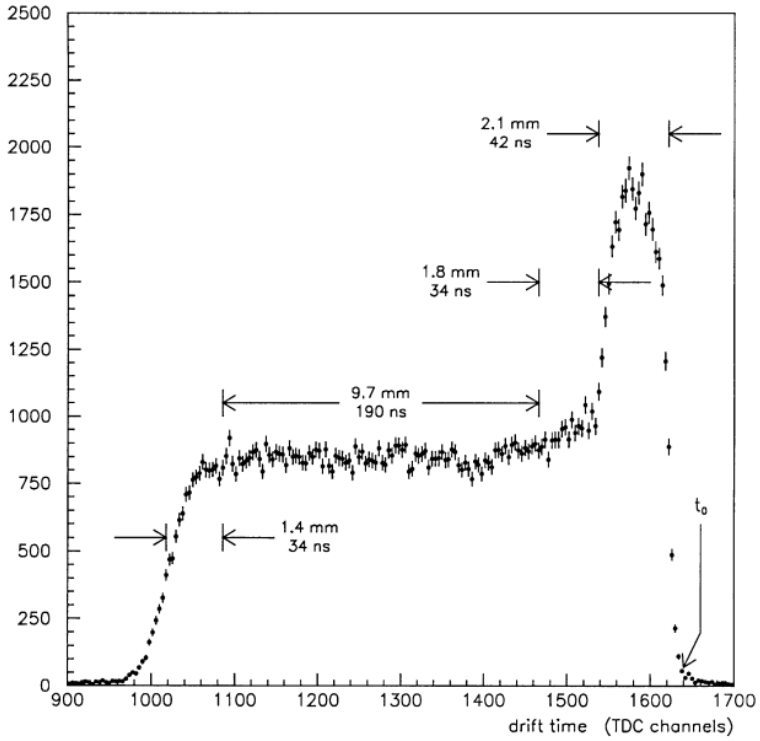

Figure 4.15: Typical TDC timing spectrum of drift times. [69]

4.4.2 Cluster Formation

Two parameter fit

The standard Hall A Analyzer algorithm uses a two-parameter fit on clusters to extract an intercept p_0 and slope p_1. Once the recorded drift times have been converted into drift distances a standard linear regression [85] is used to fit a straight line to the drift distances (as in path for figure 4.14). The algorithm extracts the fit parameters from a straight line and then converts these into two parameters, m, the slope, and b, the crossover point, as defined in equations 4.29-4.31:

$$d = p_1 u(v) + p_0, \tag{4.29}$$

$$m = \frac{1}{p_1}, \tag{4.30}$$

$$b = -\frac{p_0}{p_1}. \tag{4.31}$$

Here d is the vertical drift distance from a wire and $u(v)$ is the distance along the u(v)-plane.

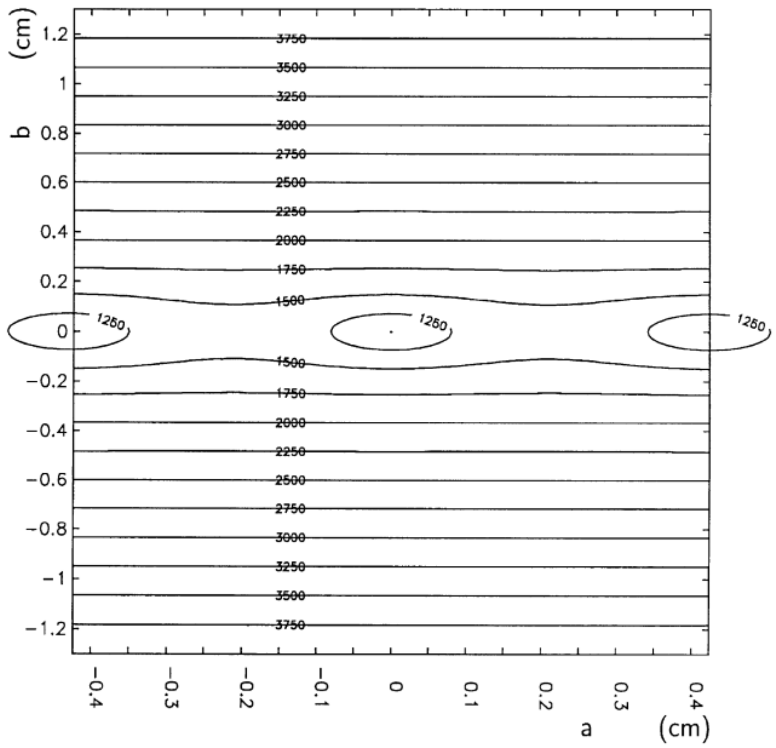

Figure 4.16: Drift cell negative high-voltage contours as modelled by GARFIELD [69]. 'a' dimension is perpendicular to wire length and in plane of VDC plane, 'b' dimension is perpendicular to VDC plane.

Three parameter fit

High rates during the APEX run in the LHRS (400 kHz) result in many events in the VDC having multiple tracks and multiple clusters in each plane. A high amount of accidental clusters (not associated with the main trigger event) were recorded by the VDC. One method of distinguishing accidental clusters from real clusters associated with the true track is based on fitting the 'timing offset' of the track. The timing offset is an additional common timing offset shared by all wire hits of an accidental cluster, due to the early or late arrival of the track with respect to the trigger. The expected distribution of the timing offsets for accidentals would thus be uniform over the total timing window recorded.

For a 'real' cluster, with five wire hits, the times recorded would be expressed as:

$$(t_{d1} + t_0), (t_{d2} + t_0), (t_{d3} + t_0), (t_{d4} + t_0), (t_{d5} + t_0). \tag{4.32}$$

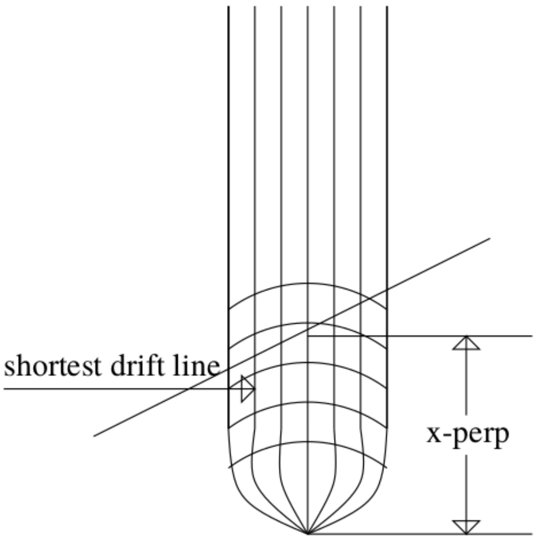

Figure 4.17: 'Drift lines' for single VDC wire. Vertical lines show path drift electrons take (for shortest time). Curved lines show perpendicular distances of tracks that have equal drift times. [83]

Accidental clusters have no relation in time to the trigger and thus the time stop of the TDCs. Wire times in accidental clusters can thus gain an additional time offset, t_{off}, and be expressed as:

$$(t_{d1} + t_0 + t_{off}), (t_{d2} + t_0 + t_{off}), (t_{d3} + t_0 + t_{off}), (t_{d4} + t_0 + t_{off}), (t_{d5} + t_0 + t_{off}). \tag{4.33}$$

If the times in an accidental cluster with timing offset, t_{off}, were to be converted to drift distances linearly (an approximation) then each distance would gain an offset $d_{off} = \pm t_{off} v_d$, where v_d is the drift velocity. This would then lead to the linear fitting of such a cluster to either overestimate or underestimate the true slope of the track made by the cluster. This is illustrated in figure 4.18. A three parameter fit can be performed by adding a 'timing mismatch' parameter.

Approximating t_{off}

Inspecting the changes in cluster times caused by t_{off} leads to the derivation of an approximation of t_{off}. If a cluster has no timing offset then the times of hits in the cluster can be expressed in terms of the pivot time, t_p (smallest time in cluster), the time

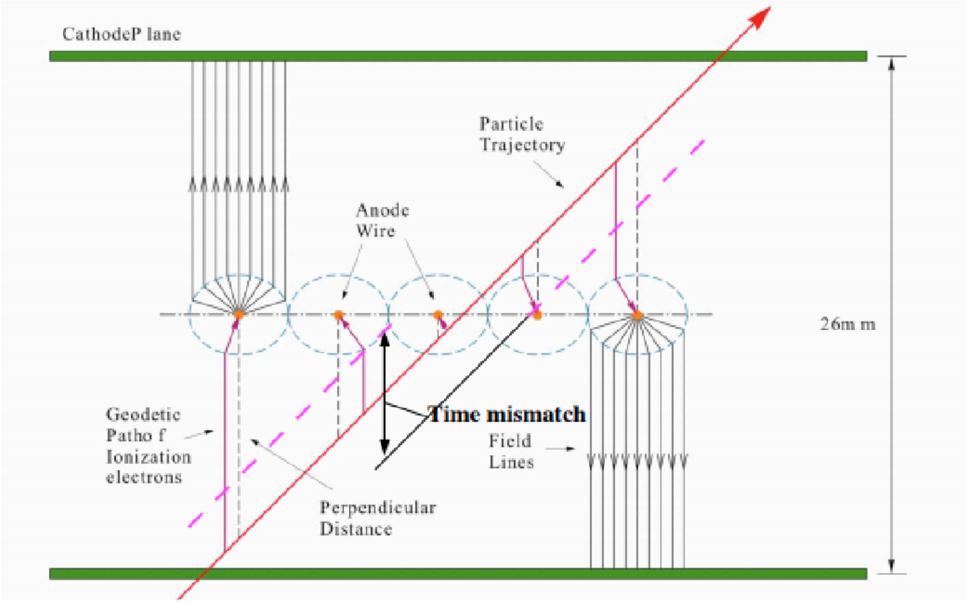

Figure 4.18: Diagram for timing offset: red line is a 'real' track with no timing offset which is well reconstructed, the dashed violet lines are the calculated drift distances for an accidental track where the time mismatch (offset) has resulted in a distance mismatch between the reconstructed path either side of the pivot wire [22].

of the wire hit where the path was closest to the wire plane. Depending on the relative sign of the vertical distances (with positive or negative vertical distance meaning above or below the wire plane) of the track at the pivot wire and other wires in the cluster, the recorded times of hits in the cluster will be greater or smaller. Assuming a linear conversion from drift time to distance, the following set of equations describes the drift times:

$$t_{p+1} = \frac{s}{v_d}\tan(\theta_t) \pm t_p, \tag{4.34}$$

$$t_{p-1} = \frac{s}{v_d}\tan(\theta_t) \mp t_p, \tag{4.35}$$

$$\implies (t_{p+1} - t_{p-1}) = \pm 2t_p, \tag{4.36}$$

$$|(t_{p+1} - t_{p-1})| - 2t_p = 0, \tag{4.37}$$

where t_{p-1} and t_{p+1} refer to the drift times of the wires proceeding and following the pivot wire, s is the separation between wires in the VDC plane and θ_t is the angle of the track with respect to the VDC plane. The signs in equations 4.34-4.36 are dependent upon the sign of d_p, the drift distance of the track at the pivot wire (whether the track passes over or beneath the pivot wire).

The addition of a timing offset, however, alters the equations to:

$$t_{p+1} = \frac{s}{v_d}\tan(\theta_t) \pm (t_p + t_{off}) + t_{off}, \tag{4.38}$$

$$t_{p-1} = \frac{s}{v_d}\tan(\theta_t) \mp (t_p + t_{off}) + t_{off}, \tag{4.39}$$

$$\implies (t_{p+1} - t_{p-1}) = \pm(2t_p + 2t_{off}), \tag{4.40}$$

$$\implies t_{off} = \frac{|(t_{p+1} - t_{p-1})| - 2t_p}{2}. \tag{4.41}$$

Equation 4.41 thus gives access to t_{off}.

The timing offset for a cluster can be extracted either by a three parameter fit (using MINUIT in ROOT) or through an approximation as described. Using a three parameter fit was computationally expensive, however, particularly for runs with higher beam currents and thus higher singles rates in the LHRS. A three parameter fit in MINUIT was also found to be unreliable for clusters which had less than five hits. The timing offsets obtained via the two methods were compared and found to be consistent within the expected timing resolution with a noted offset (∼6.7 ns). The logic of this comparison is similar to the analysis of the per-plane timing resolution in [69] where 'relative timing', ΔT, in the VDC for a cluster with five hits with the third wire being the pivot wire is defined as:

$$\Delta T = |(t_1 - t_2) - (t_5 - t_4)|, \tag{4.42}$$

where t_i is the time of the i$^{\text{th}}$ hit in the cluster. If the VDC had infinitesimal resolution, ΔT would be zero for all events, and the distribution of ΔT over many clusters would be a δ-function at $\Delta T = 0$. The width of the real distribution then gives access to the per-plane timing resolution. Assuming equal contribution from the four TDC measurements and the five drift cells crossed gives an expression for the per-plane timing resolution, Δt, of [69]:

$$\Delta t = \frac{1}{\sqrt{5}}\frac{1}{\sqrt{4}}\Delta T. \tag{4.43}$$

A similar logic can be used to check the consistency of the fitted timing offset t_{off}^{fit} and the approximated timing offset t_{off}^{app}. The difference of t_{off}^{fit} and t_{off}^{app}, ΔT_{off}, when taking into account the offset between the two, would form a δ-function at 0 if the VDC had perfect resolution and the approximation were accurate. If Δt dominates over uncertainty in the timing approximation then ΔT_{off} should give access to Δt. For the case of calculating ΔT_{off} there are four TDC measurements and three drift cells traversed which gives the expression:

$$\Delta t_{off} = \frac{1}{\sqrt{3}} \frac{1}{\sqrt{4}} \Delta T_{off}, \tag{4.44}$$

where Δt_{off} is the combination of Δt and the resolution for the approximation Δt_{app}. Figure 4.19 shows the relative timing resolution for a set of five hit clusters in the U1 plane in the LHRS for a production run, and figure 4.20 show the distribution for Δt_{off} for the same clusters. The value obtained for Δt was 2.7 ns and for Δt_{off} was 3.1 ns. Δt_{off} was thus dominated by Δt which demonstrates the timing offset approximation was accurate.

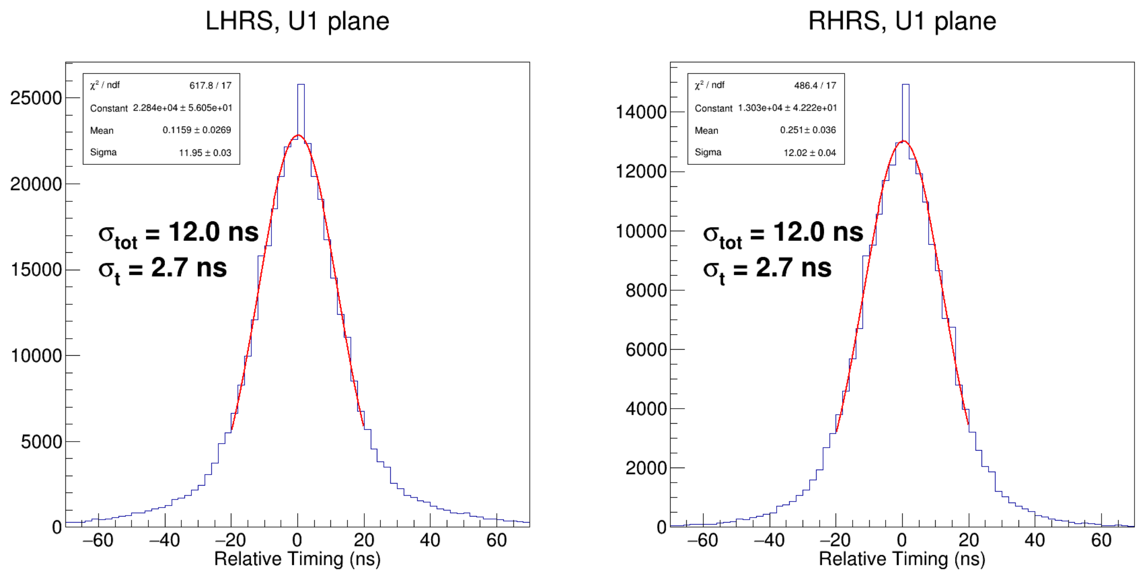

Figure 4.19: 'Relative timing' in VDC U1 plane for five-hit clusters in a production run: left plot for LHRS, right plot for RHRS.

A cut was placed on the timing offset of the cluster, of $|t_{off}| < 30$ns, as a first step of eliminating obvious accidentals (track clearly not associated with coincidence trigger).

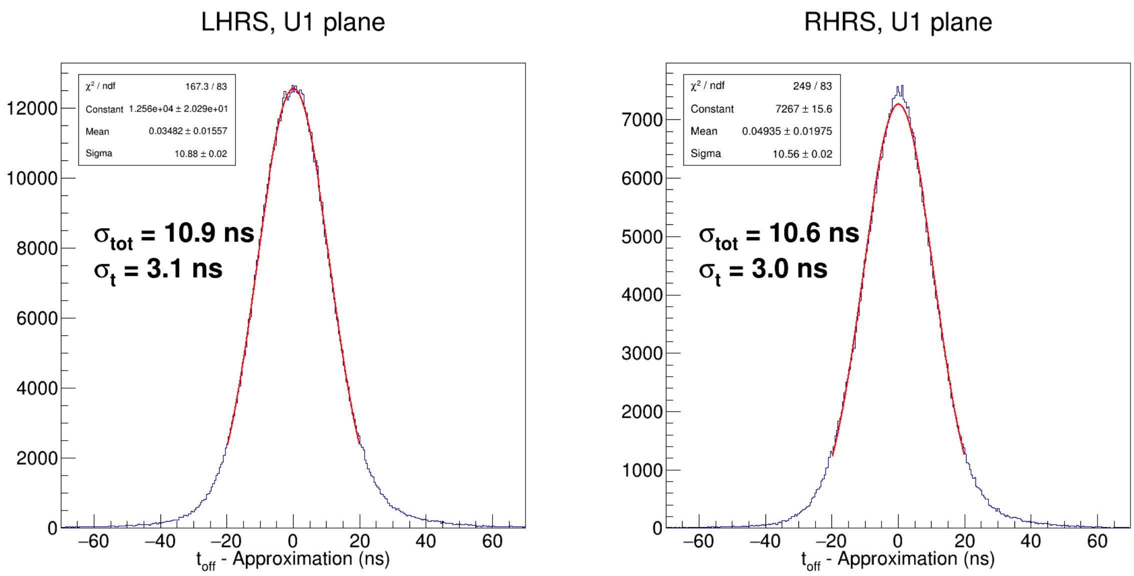

Figure 4.20: Δt_{off}, difference between fitted and approximate timing offset, in VDC U1 plane for five-hit clusters in a production run: left plot for LHRS, right plot for RHRS.

4.4.3 Track selection

The timing offset parameter can be used, in addition to other fit metrics, as a 'goodness of match' parameter, χ^2_{GoM}, for a potential track. Previously this has been formulated as [65]:

$$\chi^2_{GoM} = \chi^2_{\mu_1\mu_2} + \chi^2_{v_1v_2} + \left(\frac{t_{0,v_1v_1} - t_{0,v_1v_1}}{min(\sigma(t_{0,v_1,v_2}), \sigma(t_{0,\mu_1,\mu_2}))}\right)^2. \tag{4.45}$$

This was applicable for a previous version of the Hall A Analyzer which first formed pairs between clusters in the U planes of the lower and upper chambers and pairs between clusters in the V planes of the lower and upper chambers before forming overall tracks.

The current algorithm instead forms pairs of clusters between the U and V clusters of each chamber, 'cluster pairs', before combining to form overall tracks. A goodness of match parameter is based on contributions from the projections of clusters pairs from one chamber to the other and timing offset differences:

$$\chi^2_{GoM} = \chi^2_{\mu_1v_1} + \chi^2_{\mu_2v_2} + \chi^2_{toff}, \tag{4.46}$$

$$\chi^2_{\mu_1 v_1} = \frac{(x_{\mu_1 v_1} - x_{p(\mu_2 v_2)})^2}{\sigma^2_{x,1}} + \frac{(y_{\mu_1 v_1} - y_{p(\mu_2 v_2)})^2}{\sigma^2_{y,1}}, \tag{4.47}$$

$$\chi^2_{\mu_2 v_2} = \frac{(x_{\mu_2 v_2} - x_{p(\mu_1 v_1)})^2}{\sigma^2_{x,2}} + \frac{(y_{\mu_2 v_2} - y_{p(\mu_1 v_1)})^2}{\sigma^2_{y,2}}, \tag{4.48}$$

$$\chi^2_{toff} = \frac{1}{2} \sum_{(i=1)}^{3} \sum_{(j=i+1)}^{4} \frac{(t_{off,i} - t_{off,j})^2}{\sigma^2_{t_i} + \sigma^2_{t_j}}. \tag{4.49}$$

Here $x_p(y_p)$ is a projection of a UV pair from one chamber to the other, using its position, $x(y)$, and angle, $\theta(\phi)$ (the U and V coordinates of a cluster pair can be converted to the DCS coordinates). The terms $\chi^2_{\mu_1 v_1}$ and $\chi^2_{\mu_2 v_2}$ thus represent the (squared) difference between the position of a UV pair in one chamber and the projection from the UV pair in the opposite chamber. The subscripts 1 and 2 refer to the lower and upper chamber of the VDC respectively (as described in section 3.5.1). Equation 4.49 is the term for the timing offset contribution, the 1/2 factor comes from there being six terms in the sum of timing offset differences between the four planes but only three degrees of freedom. All terms are scaled by RMS values for their distributions such that they can be meaningfully summed.

The conversion of the U and V coordinates of a cluster pair to the DCS is described by the equations:

$$v_1 = v_1' - m_{v,1} * S_{U,V}, \tag{4.50}$$

$$x_1 = (u_1 * \sin(\alpha_v) - v_1 * \sin(\alpha_u)) * \frac{1}{\sin(\alpha_v - \alpha_u)}, \tag{4.51}$$

$$\theta_1 = (m_{u,1} * \sin(\alpha_v) - m_{v,1} * \sin(\alpha_u)) * \frac{1}{\sin(\alpha_v - \alpha_u)}, \tag{4.52}$$

$$y_1 = (v_1 * \cos(\alpha_u) - u_1 * \cos(\alpha_v)) * \frac{1}{\sin(\alpha_v - \alpha_u)}, \tag{4.53}$$

$$\phi_1 = (m_{v,1} * \cos(\alpha_u) - m_{u,1} * \cos(\alpha_v)) * \frac{1}{\sin(\alpha_v - \alpha_u)}, \tag{4.54}$$

$$p_{x,1} = x_2 - S_{1,2} * (\theta_2), \tag{4.55}$$

where x, y, θ and ϕ here are described in the DCS (Detector Coordinate System), which is detailed in section 3.5.5. These equations describe the coordinates in the first (lower) VDC chamber and an equivalent set of definitions exist for the second (upper) chamber. u_1, v_1 are the intercepts from the cluster fits in the U and V planes and $m_{u,1}$, $m_{v,1}$ are the slopes of the fits in the U and V planes respectively. $S_{U,V}$ is the separation between U and V planes, and $S_{1,2}$ is the separation between the chambers (labelled in figure 3.10). For the Hall A VDCs the angles are $\alpha_u = -45^\circ$ and $\alpha_v = 45^\circ$. Some of these equations can thus be simplified to:

$$x_1 = \frac{1}{\sqrt{2}}(u_1 + v_1), \tag{4.56}$$

$$\theta_1 = \frac{1}{\sqrt{2}}(m_{u,1} + m_{v,1}), \tag{4.57}$$

$$y_1 = \frac{1}{\sqrt{2}}(v_1 - u_1), \tag{4.58}$$

$$\phi_1 = \frac{1}{\sqrt{2}}(m_{v,1} - m_{u,1}). \tag{4.59}$$

The VDC algorithm uses χ^2_{GoM} to order potential tracks, combinations of cluster pairs from the lower and upper chambers known as 'BT pairs' (Bottom-Top pairs). Due to the high rates in the LHRS VDC and its limitations, additional cuts were used in the analysis:

- Cut on $\chi^2_{GoM} < 86$, to ensure a reasonable track.
- Cuts on cluster pair formation to ensure the resulting cluster pair has coordinates within acceptable range: -1 m $< x_{\mu_1 v_1} < 1$ m, -0.05 m $< y_{\mu_1 v_1} < 0.04$ m, -0.6 m $< x_{\mu_2 v_2} < 1.4$ m, -0.06 m $< y_{\mu_2 v_2} < 0.05$ m.
- Ambiguous track cut: if a cluster pair can form BT pairs with multiple cluster pairs in the other chamber, surviving all cuts, then ignore this event. It is a fundamental design limitation of the VDCs that the sole criterion for matching U and V clusters is their timing [65], this cut removes potentially ambiguous tracks which cannot be distinguished by the VDC.
- Multiple track cut: if there are multiple valid tracks with multiple hits in the LHRS S2 with the correct coincidence timing then the event is cut. This signature is likely caused by multiple particles originating from the reaction vertex or a secondary interaction which should be removed. Alternatively this could be observed for an e^+e^- pair, in coincidence with an accidental track (with the correct properties) but the real and accidental tracks would be difficult to distinguish with sufficient confidence.

In the case of multiple surviving tracks the algorithm takes the track with minimum χ^2_{GoM}, known as the 'golden track', forward for the remainder of the analysis.

4.4.4 Focal Plane Coordinates

Once the clusters making up a track have been determined the final DCS coordinates used are obtained from the crossover points, but not slopes, from cluster fitting. This is because the local slope, m, from fitting is strongly dependent on the TTD method used whereas the crossover point, b, is relatively independent of TTD conversion [69]. This is summarised in the following equations:

$$\theta_{DCS} = \frac{x_2 - x_1}{S_{1,2}}, \tag{4.60}$$

$$\phi_{DCS} = \frac{y_2 - y_1}{S_{1,2}}, \tag{4.61}$$

$$x_{DCS} = x_1, \tag{4.62}$$

$$y_{DCS} = y_1 - \phi_{DCS} S_{U,V}. \tag{4.63}$$

The coordinates in the DCS can then be translated into the Transport Coordinate System (TRCS) and then the Focal Plane Coordinate System (FCS), both of which are described in section 3.5.5. The FCS, a rotated coordinate system, is useful as the dispersive angle (vertical for the HRS), θ_{fp}, is small across the entire focal plane. This results in a more quickly converging optics optimisation as described in section 4.5 [71].

4.4.5 LHRS VDC Stability

During the earlier portion of the run period the LHRS VDC was found to have sub-optimal efficiency. This was noticed during running, and a scheduled beam downtime was used to inspect the VDC. The effect was found to be due to an unplugged control cable from the RPi (Raspberry Pi) board to the relay box [86], though it could not be determined when exactly this became unconnected. This relay box is controlled by the RPi board and is used to limit trip current and stop the VDC high voltage (HV) from tripping. With the RPi board disconnected, the VDC HV was connected through a 68 MΩ resistor only. After inspection this was reconnected and LHRS VDC efficiency was restored for the remainder of the run period.

The effects of this can be seen in figures 4.21 and 4.22. Plot 4.21 shows the LHRS plane efficiency for all four planes, defined as the fraction of events that pass PID cuts which produce a cluster in the plane when wire hits are processed in the VDC algorithm. The algorithm had a tolerance of allowing single wire gaps in cluster formation. Figure 4.22 shows the total LHRS VDC efficiency, defined as the fraction of events passing PID cuts for which a track was formed. As can be seen in both plots, runs before run 4664 had a significantly reduced efficiency, an effect which increased with higher beam current (as more current was being drawn from the VDC). The effect is more pronounced when looking at the total efficiency, as a track requires clusters in all four planes to be successfully formed. As can be seen in figure 4.23, showing the total VDC efficiency for the RHRS, the RHRS VDC did not have this problem (the RPi board to relay box connection was also checked and found to be properly connected).

For the LHRS the reduced VDC efficiency for the earlier portion of the run period can be seen in individual wire efficiencies, defined for a wire as the fraction of events where the wire records a hit when the two adjacent wires have recorded hits (for the two end wires in a plane the definition is adjusted to the one adjacent wire). Figure 4.24 shows the wire efficiencies for the LHRS U1 VDC plane for run 4119 and 4668 respectively, where run 4119 was recorded before correction with reduced VDC efficiency and run 4668 was taken after reconnection.

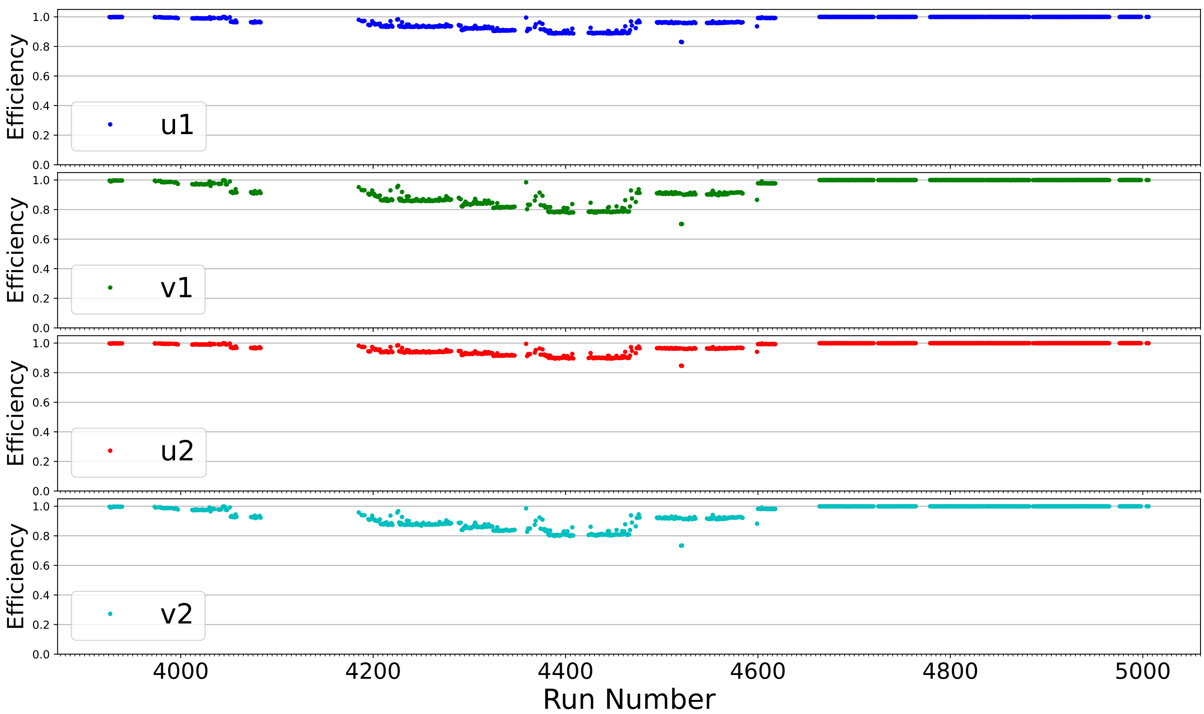

Figure 4.21: LHRS VDC plane efficiency plots for all production runs. For each run plane efficiency is defined as the fraction of events passing PID cuts that have at least one cluster successfully formed in the plane.

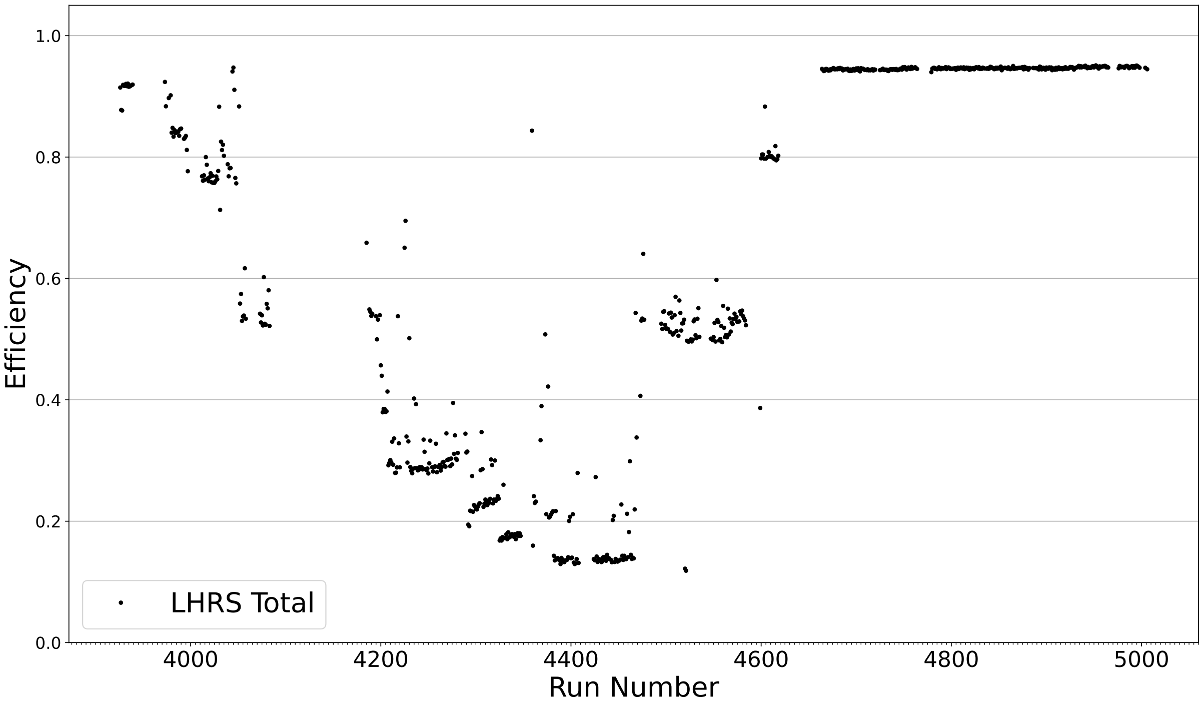

Figure 4.22: LHRS total VDC efficiency plot for all production runs. Total efficiency defined as fraction of events passing PID cuts that have at least one track formed.

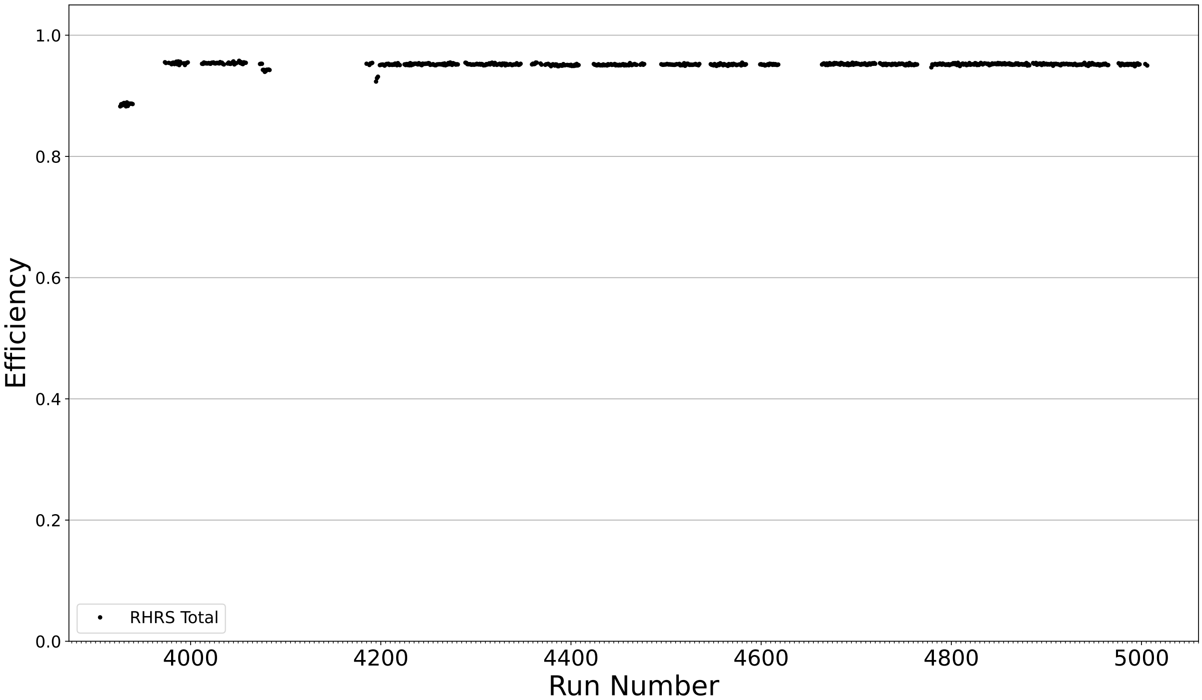

Figure 4.23: RHRS total VDC efficiency plot for all production runs. Total efficiency defined as fraction of events passing PID cuts that have at least one track formed.

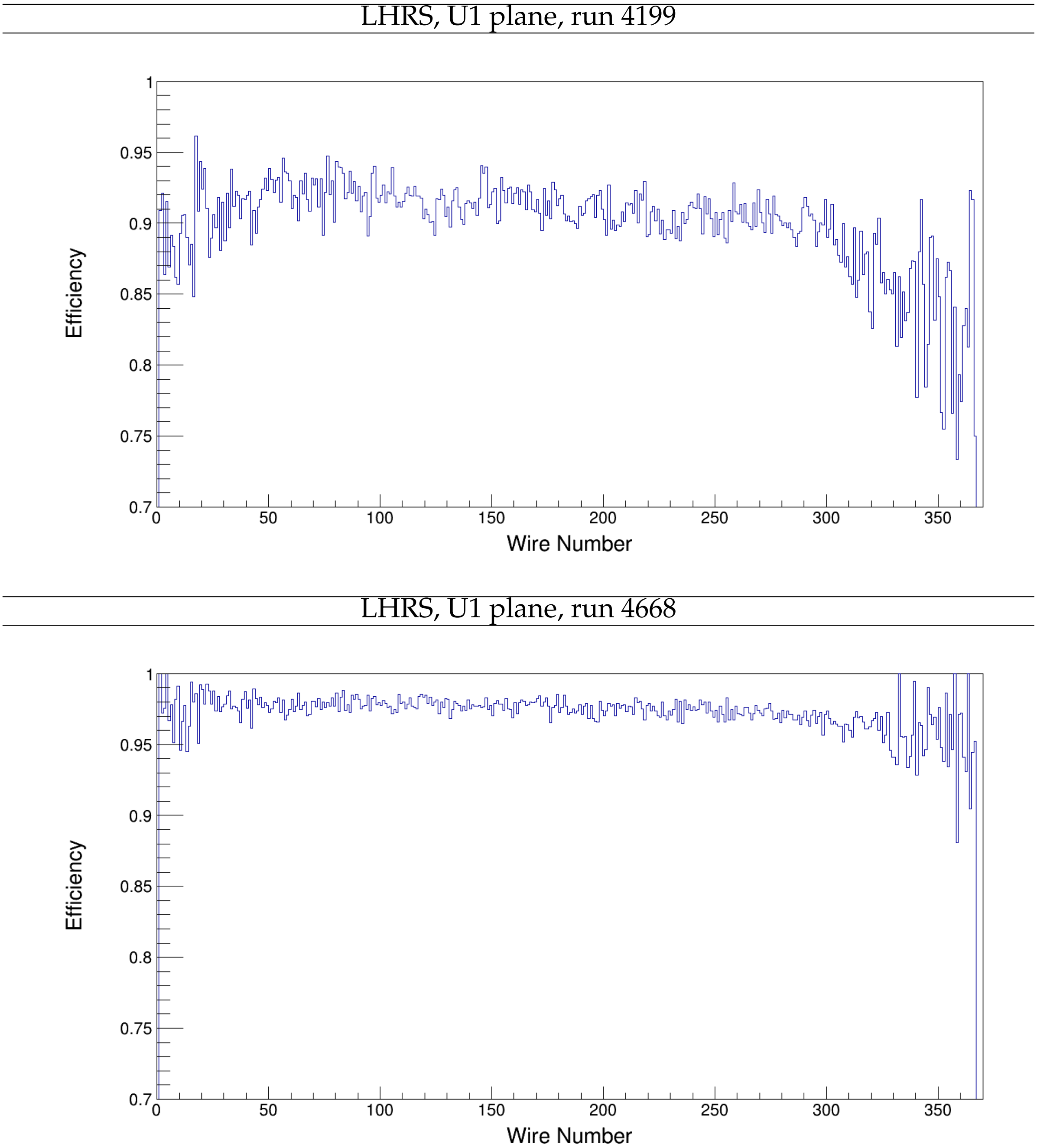

Figure 4.24: LHRS VDC U1 wire efficiency plots. Wire efficiency defined as fraction of events where a VDC wire records a hit when its adjacent wires have recorded hits. Top plot is from run 4199 before correction, bottom plot is from run 4668 after correction.

4.5 Spectrometer Optics

Optics reconstruction is a well-established process for the HRSs. This operation is used to take focal plane coordinates (from tracks in the VDC) and project them backwards through the HRS magnetic elements on to target variables in the TCS (described in [87] and section 3.5.5). For optics calibration the x-component of the trajectory at the target in the TCS, x_{tg}, is set to zero [87] and as a first order approximation the following relationship between coordinates at the target and focal plane is true for a standard HRS experiment:

$$\begin{bmatrix} \delta \\ \theta \\ y \\ \phi \end{bmatrix}_{tg} = \begin{bmatrix} \langle\delta|x\rangle & \langle\delta|\theta\rangle & 0 & 0 \\ \langle\theta|x\rangle & \langle\theta|\theta\rangle & 0 & 0 \\ 0 & 0 & \langle y|y\rangle & \langle y|\phi\rangle \\ 0 & 0 & \langle\phi|y\rangle & \langle\phi|\phi\rangle \end{bmatrix} \begin{bmatrix} x \\ \theta \\ y \\ \phi \end{bmatrix}_{fp} . \tag{4.64}$$

Equation 4.64 is only true, however, when the system posseses 'midplane symmetry'. The standard QQD_nQ HRS magnet configuration (described in section 3.5) exhibits midplane symmetry meaning that there is a midplane such that the magnetic field $\vec{B}$ is always normal to the plane. This plane is defined in the TCS by x_{tg} (dispersive in dipole) and y_{tg} (non-dispersive in dipole).

4.5.1 Optics with septum magnet

The introduction of the septum magnet into the APEX set-up breaks the midplane symmetry for both arms (as an orthogonal dipole to the existing HRS dipole). The relationships between focal plane and target coordinates are thus more complex.

The target coordinates, $\vec{x}_{tg}$, can be related to the focal plane coordinates, $\vec{x}_{fp}$, through a set of tensors described by:

$$y_{tg} = \sum_{j,k,l} Y_{jkl} \theta^j_{fp} y^k_{fp} \phi^l_{fp} = \sum_{i,j,k,l} C^Y_{ijkl} x^i_{fp} \theta^j_{fp} y^k_{fp} \phi^l_{fp}, \tag{4.65}$$

$$\theta_{tg} = \sum_{j,k,l} T_{jkl} \theta^j_{fp} y^k_{fp} \phi^l_{fp} = \sum_{i,j,k,l} C^T_{ijkl} x^i_{fp} \theta^j_{fp} y^k_{fp} \phi^l_{fp}, \tag{4.66}$$

$$\phi_{tg} = \sum_{j,k,l} P_{jkl} \theta^j_{fp} y^k_{fp} \phi^l_{fp} = \sum_{i,j,k,l} C^P_{ijkl} x^i_{fp} \theta^j_{fp} y^k_{fp} \phi^l_{fp}, \tag{4.67}$$

$$\delta p = \sum_{j,k,l} D_{jkl} \theta^j_{fp} y^k_{fp} \phi^l_{fp} = \sum_{i,j,k,l} C^D_{ijkl} x^i_{fp} \theta^j_{fp} y^k_{fp} \phi^l_{fp}, \tag{4.68}$$

where the tensors Y_{jkl}, T_{jkl}, P_{jkl} and D_{jkl} are polynomials in x_{fp} and C_{ijkl} are the elements of the 'optics matrix'. This is known as the matrix description and in the case of midplane symmetry gives the restrictions that for T_{jkl} and D_{jkl} non-zero elements must have (k+l) being even and for Y_{jkl} and P_{jkl} non-zero elements must have (k+l) being odd (where k and l are as defined in equations 4.65-4.68). These conditions do not apply for the APEX set-up where a septum is deployed.

The introduction of the septum substantially increases the uncertainty in the vertical angle (θ_{tg}), horizontal angle (ϕ_{tg}), and vertex position (z_{react}). The standard resolutions for the HRS (without septum) are ∼0.21 mrad for ϕ_{tg}, ∼0.42 mrad for θ_{tg} and ∼0.42 mm for z_{react} [65]. For the 2010 APEX analysis (which had a septum installed) the angular resolutions were 0.29 mrad for ϕ_{tg} and 1.86 mrad for θ_{tg} for the LHRS, and 0.44 mrad for ϕ_{tg} and 1.77 mrad for θ_{tg} for the RHRS [68].

4.5.2 Optics Calibration Procedure

The values of these tensors are optimised through the sieve slit calibration method. The sieve slits are 6.35 mm thick collimators with grids of holes with well measured and established positions, x_{sieve} and y_{sieve}, which are inserted before the septum magnet (detailed in section 3.9). Electrons which are not incident on holes are absorbed by the sieve slit and thus particle tracks found in the spectrometer can be associated with positions x_{sieve}, y_{sieve} (though a small amount of 'punch-through' the sieves is possible). From surveying the Hall, and knowledge of the beam position (see section 4.3) these sieve slit positions can be related to target variables by:

$$\theta_{tg} = \frac{x_{sieve} + D_x + y_{beam}}{L - z_{surv}\cos(\theta_0) - x_{beam}\sin(\theta_0)}, \tag{4.69}$$

$$\phi_{tg} = \frac{y_{sieve} + D_y - x_{beam}\cos(\theta_0) + z_{surv}\sin(\theta_0)}{L - z_{surv}\cos(\theta_0) - x_{beam}\sin(\theta_0)}, \tag{4.70}$$

$$x_{tg} = x_{sieve} - L\theta_{tg}, \tag{4.71}$$

$$y_{tg} = y_{sieve} - L\phi_{tg}, \tag{4.72}$$

$$z_{react} = \frac{-(y_{tg} + D_y) + x_{beam}(\cos(\theta_0) - \phi_{tg}\sin(\theta_0))}{\cos(\theta_0)\phi_{tg} + \sin(\theta_0)}, \tag{4.73}$$

where L, θ_0, D_x and D_y are defined for the TCS (as described in section 3.5.5) and z_{react} is a reconstructed particle position from the optics matrix. z_{react} can be compared with z_{surv}, the known z position of targets used in optics.

For all of these quantities the optics reconstruction matrix is then optimised by minimising a function of the form:

$$\delta(W) = \sum_{s} \left[\frac{\sum_{ijkl} C^{Y}_{jkl} x^{i}_{fp} \theta^{j}_{fp} y^{k}_{fp} \phi^{l}_{fp} - W^{0}}{\sigma^{s}_{W}} \right]^{2}, \tag{4.74}$$

where s is the number of events taken for calibration, W represents any of the target variables and W_0 is the corresponding reference value established from measurement and surveying of the Hall.

The APEX target system, as described in section 3.7 and illustrated in figure 3.12, had several targets designed for use in optics calibration. The vertical and horizontal wire targets were staggered such that an individual wire could be targeted for an optics run. This allowed a starting point for optics which could then be improved by use of the optics foils which covered the full phase space, and could be positioned such that the beam hit only four or all eight foils at once. Runs were taken with a low beam current ($\sim 1\mu A$) to minimise noise.

4.5.3 Angular Resolutions

The angular resolutions (in θ_{tg} and ϕ_{tg}) were extracted from the resolutions observed in sieve hole distributions which had two separate contributions: the resolution due to optics reconstruction, σ_{opt}, and the surveyed width of the sieve hole, σ_{sur}. Previous analyses (including the APEX 2010 test run) have fit a Gaussian to the observed distribution for sieve holes in θ_{tg} or ϕ_{tg}, σ_{tot}, and subtracted in quadrature the known value for contribution of the sieve hole width, σ_{sur}. It was found during analysis that for some holes the distribution of events deviated significantly from a Gaussian and extraction of the resolution from this method would be unreliable. The angular distributions for sieve holes were instead described as the convolution, $c(\theta_{tg})$, of a normal distribution (describing the optics resolution), $n(\theta_{tg})$, and a function describing a uniform circular distribution in one dimension, $u(\theta_{tg})$, which accounted for the contribution from the sieve hole:

$$u(\theta) = 2h\sqrt{(R_\theta^2 - (\theta - \theta_{cen})^2)}, \tag{4.75}$$

$$n(\theta) = \frac{1}{\sigma_\theta\sqrt{2\pi}} e^{\left(-\frac{1}{2}\frac{\theta^2}{\sigma_\theta^2}\right)}, \tag{4.76}$$

$$c(\theta) = u(\theta) \circledast n(\theta), \tag{4.77}$$

where h is a scaling factor (directly proportional to the number of hits passing through a sieve hole), R_θ is the equivalent of the known radius of the sieve hole (R) in θ: $R_\theta = \arctan(\frac{R}{D_{sep}})$, where D_{sep} is the distance from sieve hole to target, θ_{cen} is the centre of the hole in θ_{tg} and σ_θ is the RMS of the normal distribution. Equivalents of equations 4.75-4.77 and subsequent definitions apply in ϕ_{tg} also. Figure 4.25 is an example of these fits in θ_{tg} and ϕ_{tg} for a sieve hole, from an optics run with the V2 wire target.

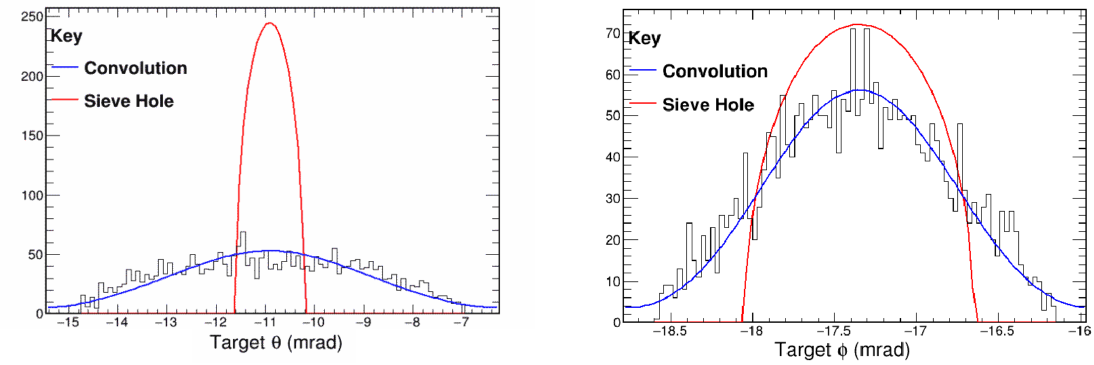

Figure 4.25: Sieve hole in column 10, row 6 for optics run with V2 wire target. For both plots the red function represents the uniform circular distribution, the blue function a convolution of the uniform circular distribution with a Gaussian. Left plot: θ_{tg} distribution, Right plot: ϕ_{tg} distribution.

The procedure for optimisation was carried out for both arms separately. For both arms events from vertical wire and optics foil runs were used. Vertex cuts were made such that events could be identified with a particular target and subsequent sieve hole cuts were made such that events could be identified with a sieve hole from which angular information could be calculated (in combination with the known z position). For both arms the two most downstream optics foils (O7 and O8) did not have clear enough reconstructed sieve holes to identify and use in optimisation.

The resulting angular resolutions from optimisation were for the LHRS 0.46 mrad in ϕ_{tg} and 1.8 mrad in θ_{tg}, and for the RHRS 0.56 mrad in ϕ_{tg} and 1.76 mrad in θ_{tg}.

Sieve plane projections from optics runs taken with the vertical wires are shown in figures 4.26 and 4.27 showing the unoptimised and final optimised results respectively. Both figures show the same sieve hole data from vertical wire runs from which sieve holes were cut as described above.

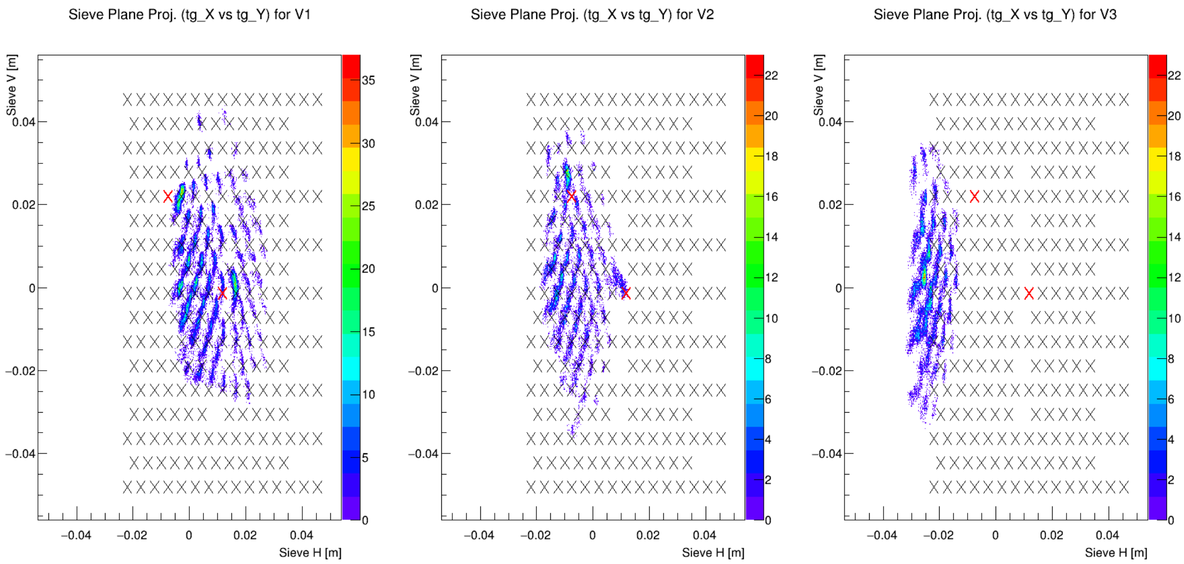

Figure 4.26: Sieve plane projections for the vertical wires (named V1, V2 and V3 from upstream to downstream) using an unoptimised optics matrix from previous experiment. Crosses show position of sieve holes from survey, with red crosses marking the two larger sieve holes. Colour scale on right corresponds to number of events in histogram bins. Data selection described in text.

4.5.4 Vertex Reconstruction

The vertex resolution is related to the resolution in y_{tg} as described by equation 4.73. The known positions of the sieve holes, and the optics targets (3.12), were used to obtain the reference values, W_0 (as in 4.74), used for optimisation of $y_{tg}/\ z_{react}$.

The initial steps of optics optimisation used optics runs with the beam directed at individual vertical wires such that events (after acceptance cuts) could be assumed to have originated from a known vertex position. Results of vertex resolution for the vertical wires can be seen in figures 4.28 and 4.29. For both arms the process of expanding $y_{tg}/\ z_{react}$ optimisation to the optics foils proved to be challenging, with only the 6 most upstream optics foils (O1-O6 in the nomenclature of 3.12) having clear enough data to extract sieve holes from.

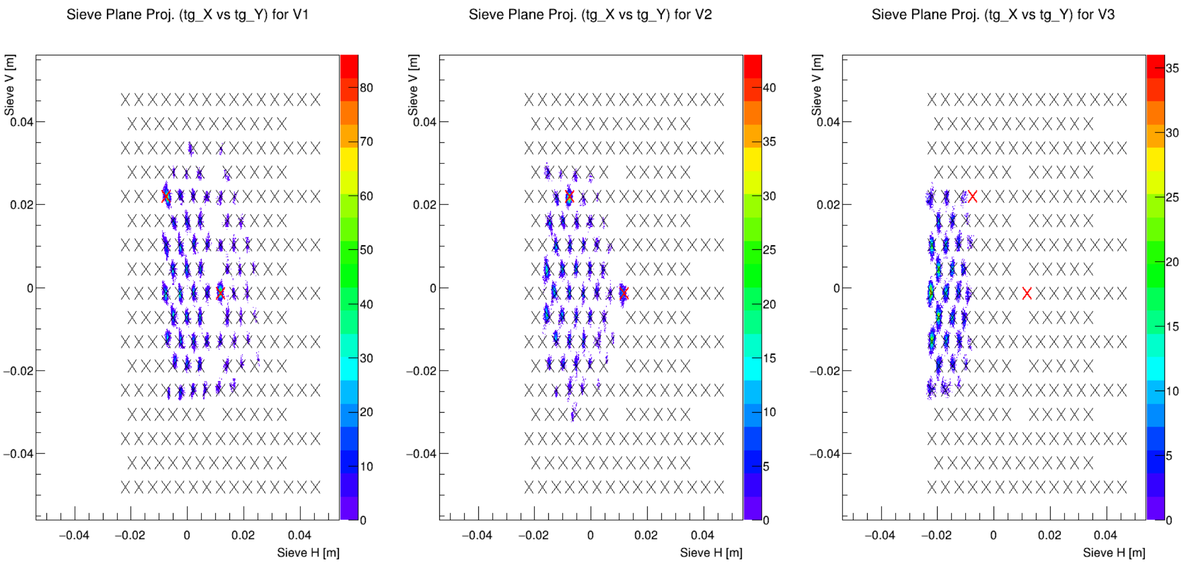

Figure 4.27: Sieve plane projections for the vertical wires (named V1, V2 and V3 from upstream to downstream) using optimised optics matrix (optimised on the vertical wires and optics foils 1-6). Crosses show position of sieve holes from survey, with red crosses marking the two larger sieve holes. Colour scale on right corresponds to number of events in histogram bins. Data selection described in text.

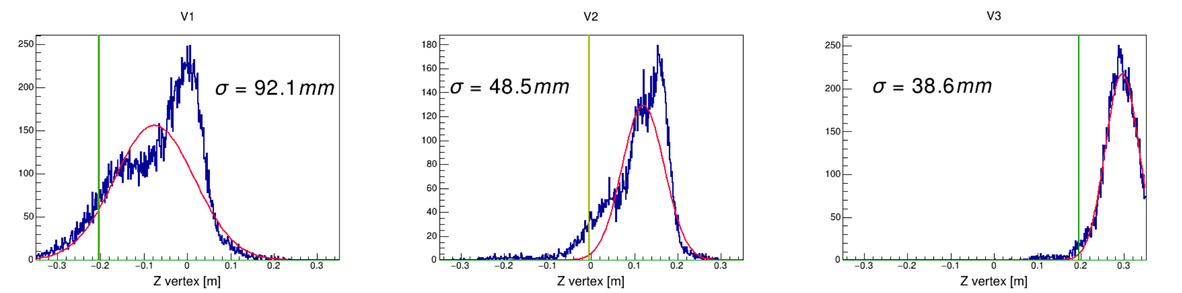

Figure 4.28: Reconstructed Z for all Vertical Wires with unoptimised LHRS optics matrix. Blue line shows reconstructed z, red line shows a Gaussian fit (with σ of fit displayed) and the green line marks the true position of vertical wire from survey. For the unoptimised matrix, the distribution is clearly non-Gaussian but a Gaussian fit is included for illustration.

The reconstructed z position was ultimately used in a cut to separate true from accidental coincidences for the final event sample. The obtained vertex resolution can thus be examined in the context of production data. For production data a coincidence is required between the two HRS arms. If this is a true coincidence then the electron (in the LHRS) and positron (in the RHRS) should be reconstructed to the same production foil. The difference between LHRS and RHRS reconstructed z vertices should thus provide a cut to separate true coincidences from accidentals for

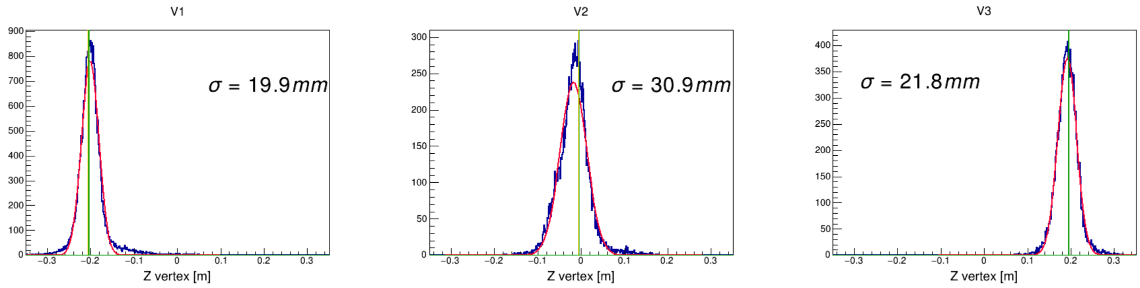

Figure 4.29: Reconstructed Z for all Vertical Wires with optimised LHRS optics matrix. Blue line shows reconstructed z, red line shows a Gaussian fit (with σ of fit displayed) and the green line marks the true position of vertical wire from survey.

which the two reconstructed z vertices do not have any relationship. This can be seen in figure 4.30, the left-plot of which illustrates the relatively flat random (sideband) distribution compared to the peaked structure of the prompt events. The right-plot of figure 4.30 is the prompt distribution after sideband subtraction. The width of the z vertex difference distribution, $\sigma_{z_{diff}}$, (after sideband subtraction) is related to the z vertex resolutions of both arms, $\sigma_{z,L}$ and $\sigma_{z,R}$, as follows:

$$\sigma_{z_{diff}} = \sqrt{\sigma_{z,L}^2 + \sigma_{z,R}^2}, \tag{4.78}$$

$$\sigma_{z,L} = \sigma_{z,R} = \frac{1}{\sqrt{2}} \sigma_{z_{diff}}. \tag{4.79}$$

Equation 4.79 is true under the assumption that the z vertex resolution is equal for both arms. With this assumption the fit of the z vertex difference (as illustrated in figure 4.30) then allows extraction of an estimate of the single arm z vertex resolutions. This fit is also used to determine a cut on the z vertex difference which is used for obtaining the final invariant mass sample (cut shown in figure 4.30), as 2.5 $\sigma_{z_{diff}}$. The resulting single arm resolutions are $\sigma_{z,L} = \sigma_{z,R} \sim 32.7$ mm. This estimate of $\sigma_{z,L}$ and $\sigma_{z,R}$, however, does obscure differences between the two arms and variation in the z vertex resolution along the z vertex range. It can be compared to the values obtained in the 2010 APEX test run, which were $\sigma_{z,L} = 27$ mm and $\sigma_{z,R} = 17$ mm [68]. The 2010 APEX set-up, however, only had one target which meant a vertex (or equivalently y_{tg}) optimisation which was only constrained by one position and could potentially achieve an artificially 'good' resolution (as the 2010 run only had one target the analysis did not focus on the z vertex reconstruction).

The production targets for APEX are separated by 55 mm, so to be clearly distinguishable on an event-by-event basis the z vertex resolutions would need to be

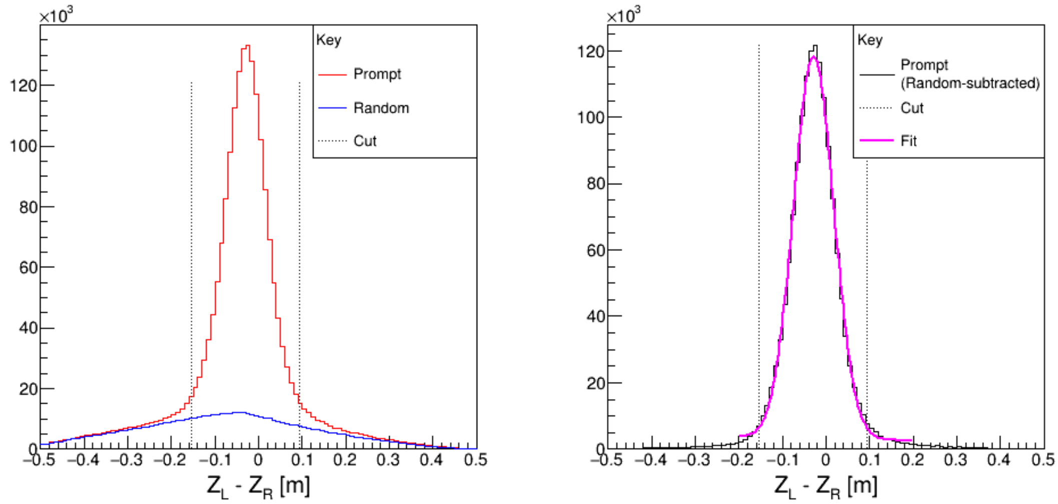

Figure 4.30: Z vertex difference plots (between arms), defined as $z_L - z_R$. Left: Distribution for events for prompt (red) and random (blue) timing cuts, with z vertex difference cut shown. Right: Distribution for prompt after sideband subtraction (black) with Gaussian fit (Magenta) and z vertex difference cut shown.

$\sigma_{z,L.,(R)} \lesssim 18.3\,mm$. This was not achieved in the 2019 analysis, though the resolution obtained still allows for cut on the z vertex difference to be used. Figure 4.31 shows a plot of the z vertex difference, $z_L - z_R$, against the mean of the z vertices, $(z_L + z_R)/2$ (prompt random-subtracted), where the ten production foils are visible.

4.5.5 Momentum Reconstruction

The momentum deviation, $\delta p = \frac{(p-p_0)}{p}$ where p_0 is the central momentum, is obtained from focal plane coordinates as described by equation 4.68. The standard procedure for optimising the momentum resolution relies on using a carbon target and the known carbon elastic peaks for scattering [65]. The momentum can be calculated from scattered electron energy, E', incoming electron energy, E, target mass, M, and scattering angle θ_{scat}:

$$p(M,\theta) = E' = \frac{E}{1 + E/M(1 - \cos(\theta_{scat}))}. \tag{4.80}$$

With corrections for energy loss in the target this allows for the extraction of 'true' δp, and thus W_0 (as in equation 4.74) in the optimisation of the momentum resolution. For the APEX 2019 run it was not possible to perform the 'delta scan' with a carbon target as is used in the standard momentum optimisation. Momentum optics elements, C^D_{ijkl},

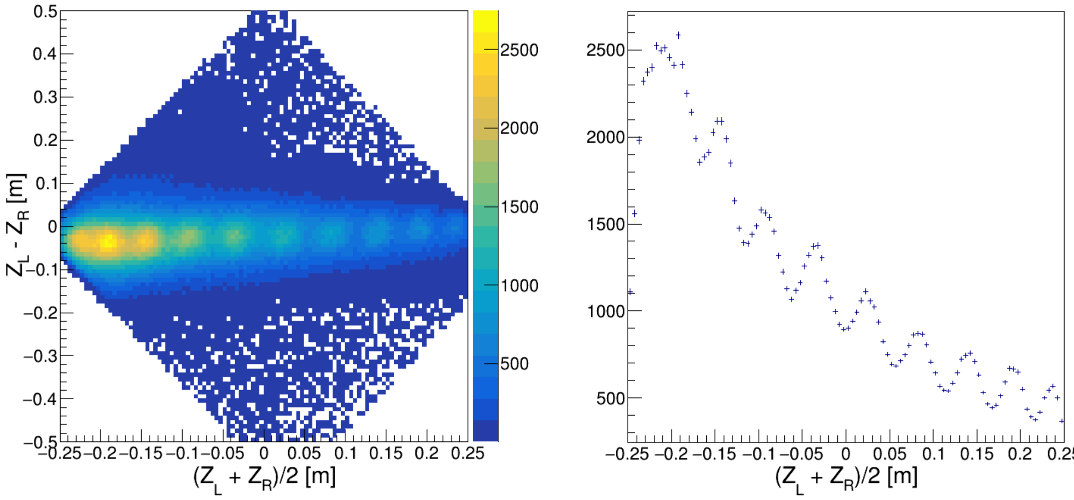

Figure 4.31: Left: Z vertex difference, $z_L - z_R$, plotted against z vertex mean, $(z_L + z_R)/2$ (prompt random-subtracted). Colour scale on right corresponds to number of events in histogram bins. Right: Constant parameter of Gaussian fit of $(z_L - z_R)$ over small ranges of $(z_L + z_R)/2$, showing average reconstructed position of target foils.

were taken from a previous experiment with a septum installed. An estimate of the momentum resolution was determined with production data, using the momentum deviation from both arms.

As with the examination of z vertex reconstruction it was necessary when looking at production data to use sideband subtraction to account for accidental coincidences. An upper limit for the momentum deviation sum exists for true coincidence pairs, whose momentum sum is related to the beam energy. For accidental coincidences the sum is only limited by the momentum acceptance in each spectrometer independently. This can be seen in the left-plot figure 4.32, where the different distributions of prompt and sideband events for the momentum deviation sum are evident. The right-plot of figure 4.32 shows the prompt distribution after sideband subtraction. If both arms possessed perfect momentum resolution, $\sigma_{\delta p}$, then the drop off in the momentum deviation sum distribution after reaching the limit for the momentum deviation sum would be purely vertical. The observed deviation from this can thus be used to extract the resolution (of the momentum deviation sum, $\sigma_{\delta p_{sum}}$). To exclude acceptance effects, from the edges of the momentum acceptance, a cut on both single arm momentum deviations can be made: $|\delta p| < 0.02$. A plot of the momentum deviation sum with this additional cut, and a zoomed in axis on the region of interest, is shown in figure 4.33. The divergence from an absolute drop off at the momentum deviation sum cut off can be modelled as the complement of the cumulative distribution function of a Gaussian distribution multiplied by a function describing the momentum deviation sum distribution (before the cut off). The fit in figure 4.33 uses a first order polynomial to describe the momentum deviation sum distribution, and with this obtains a resolution for the momentum deviation sum of 1.35×10^{-3}. This fit was also used to determine the cut on the momentum deviation sum: $\sigma_{\delta p_{sum}} < 0.0187$. Similar to the process described in section 4.5.4 and equation 4.79 for the vertex resolution, if both arms are assumed to have the same momentum resolution then $\sigma_{\delta p,L} = \sigma_{\delta p,R} = \frac{1}{\sqrt{2}}\sigma_{\delta p_{sum}}$, and the resulting single-arm momentum resolution for both arms is 9.35×10^{-4}. This can be compared to the standard resolution of $\mathcal{O}(10^{-4})$ [65] and the resolution achieved in the 2010 APEX test run of $< 5 \times 10^{-4}$ [68]. The momentum deviation resolution is ultimately a small contribution to the final invariant mass resolution, as discussed in section 5.2.

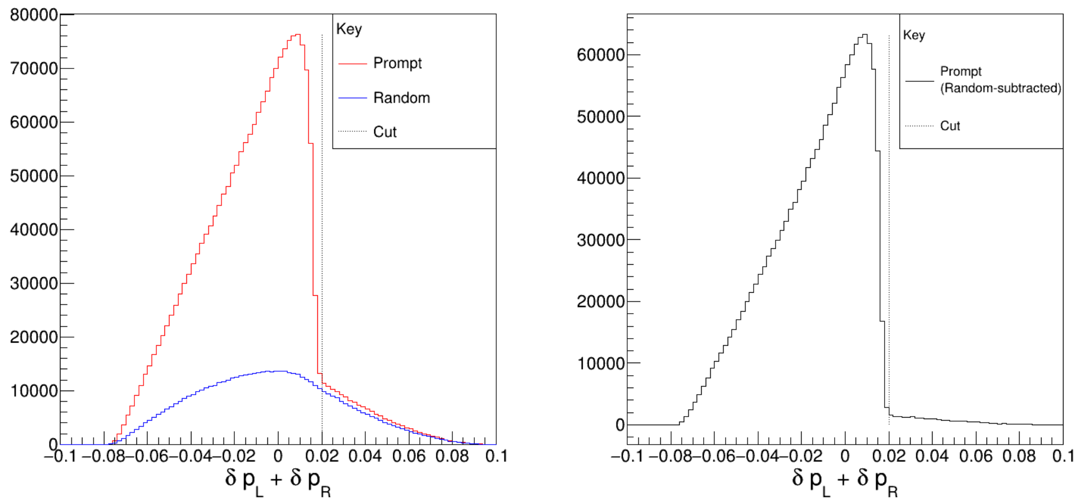

Figure 4.32: Momentum deviation sum plots defined as $\delta p_L + \delta p_R$. Left: Distribution for events for prompt (red) and random (blue) timing cuts, with momentum deviation sum cut shown. Right: Distribution for prompt after sideband subtraction (black) and momentum deviation sum cut shown.

4.5.6 Optics Status

The optics optimisation achieved can be discussed in relation to the different functions it serves in the analysis (as presented in this thesis): cuts to separate true coincidences from accidentals and the different contributions to the invariant mass resolution. The z-vertex resolution obtained serves as a cut on the difference in z-vertex between

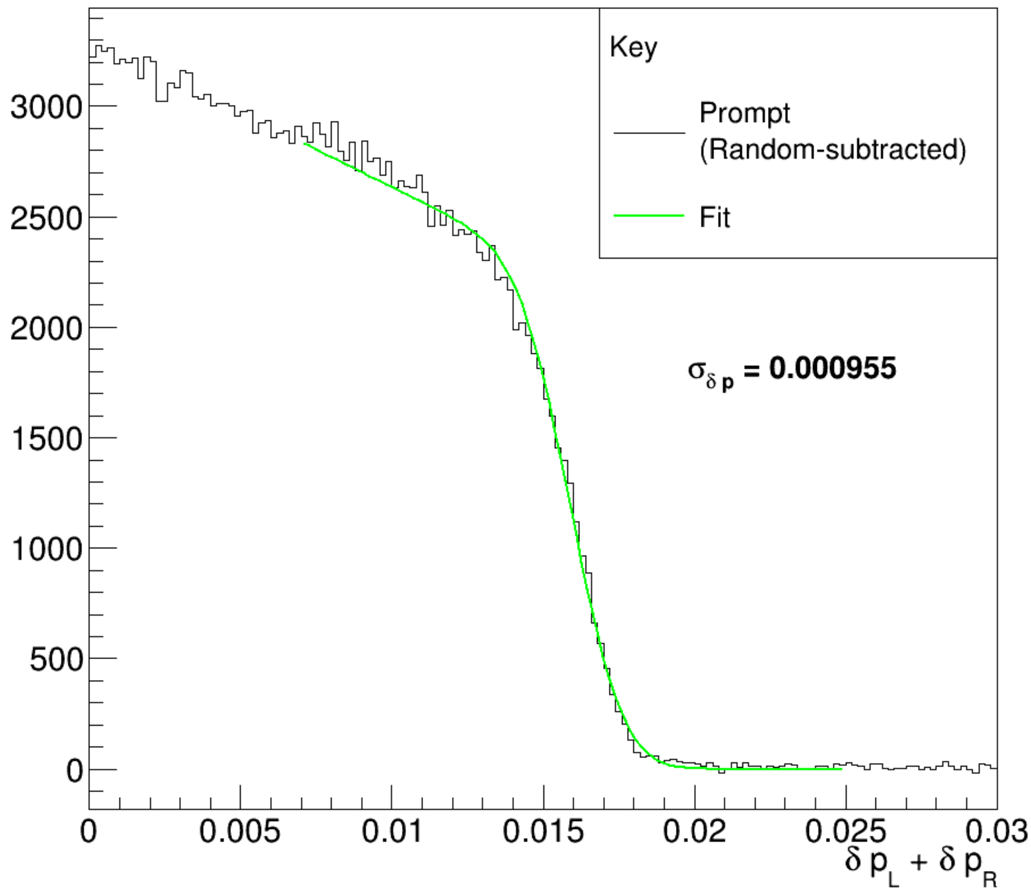

Figure 4.33: Prompt sideband-subtracted momentum deviation sum plot defined as $\delta p_L + \delta p_R$ (with additional cut of $|\delta p_{L(R)}| < 0.02$).

arms. Any improvement on this would decrease the accidental fraction, and thus improve the final reach in ϵ^2. As discussed in section 5.2, both angular resolutions contribute to the invariant mass resolution with σ_θ having a larger effect than σ_ϕ. The angular resolutions are similar to those obtained in the 2010 APEX analysis and other analyses [88] with the septum magnet installed with the HRS. This suggests that there may only be limited improvement possible for the angular resolutions, at least in the reported average value, though a different approach, as described below, could improve the consistency of this resolution across the focal plane and thus have meaningful improvements in the invariant mass resolution for a part of the invariant mass range. The momentum resolution achieved could potentially be improved though the effect this has on the invariant mass resolution is minimal.

Future work would look to construct a description of the overall optics system as a combination of two matrices in succession: a matrix to describe the septum and a matrix to describe the HRS. This second matrix should be described accurately by simulation, taking into account the particular magnetic tune used for the HRS. A matrix to describe the septum magnet could then be optimised to data.

4.6 Final Event Sample

The final event sample for the preliminary peak search was produced after applying the series of cuts described previously: PID cuts, coincidence timing cuts, track cuts, cuts on the z vertex difference, a cut on the momentum deviation sum and a trigger cut (on T6, the coincidence trigger). An additional set of cuts based on the spectrometer acceptance were used. Only regions with optimised optics (as described in section 4.5) are kept for the final event sample. This can be seen in figures 4.34 and 4.35 which illustrate the acceptance cuts for the LHRS and RHRS respectively. These two-dimensional cuts are placed on distributions of ϕ_{tg}, θ_{tg}, δp and z.

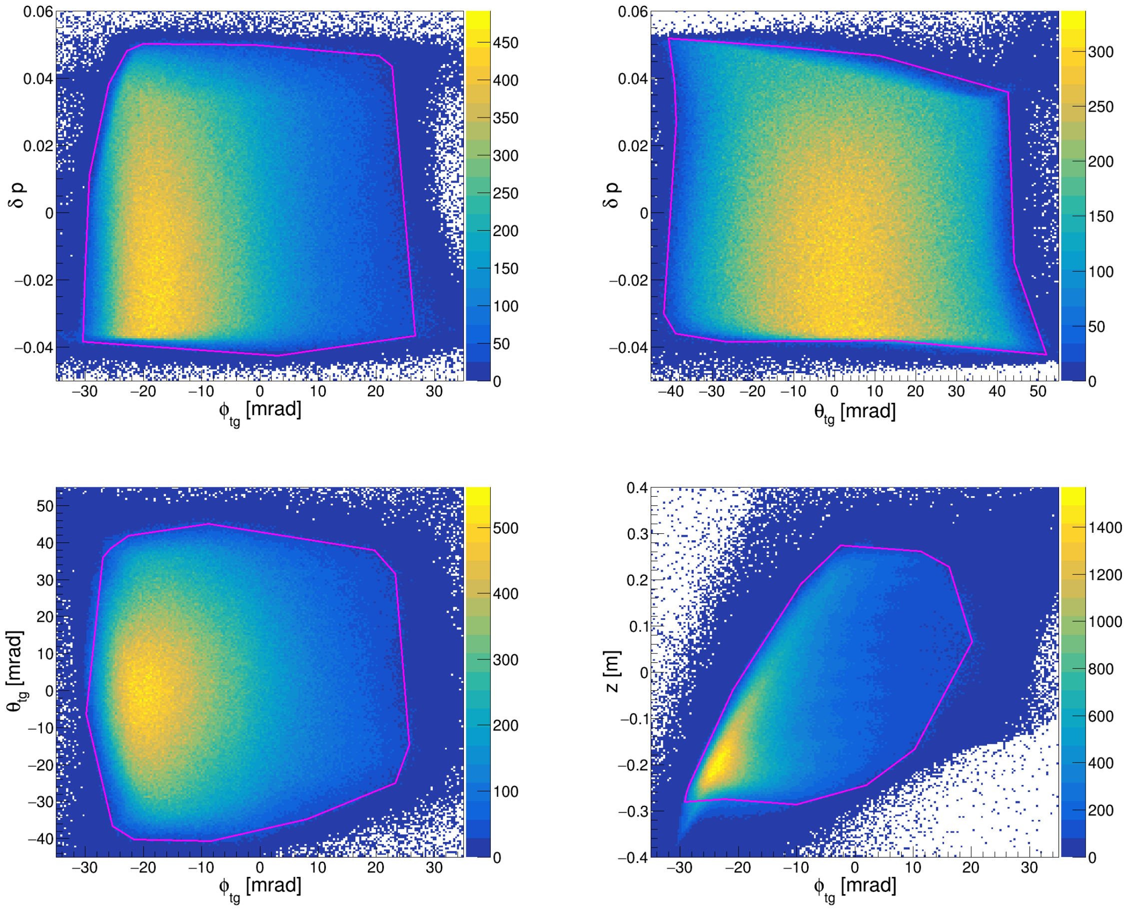

Figure 4.34: LHRS acceptance cuts. Clockwise from top-left plots show δp vs ϕ_{tg}, δp vs θ_{tg}, θ_{tg} vs ϕ_{tg}, and z vs ϕ_{tg} distributions for a production run (4668). The magenta lines illustrate the acceptance cuts. Colour scale on right corresponds to number of events in histogram bins.

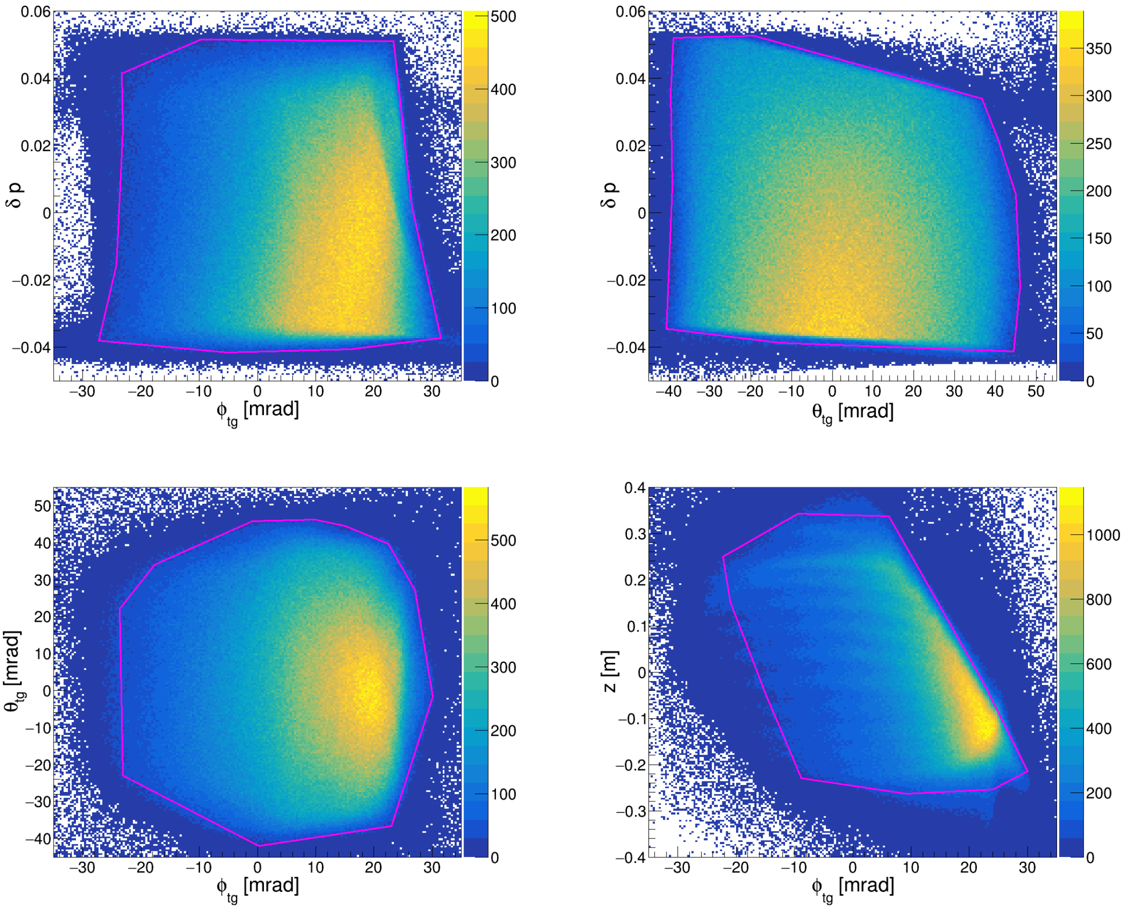

Figure 4.35: RHRS acceptance cuts. Clockwise from top-left plots show δp vs ϕ_{tg}, δp vs θ_{tg}, θ_{tg} vs ϕ_{tg}, and z vs ϕ_{tg} distributions for a production run (4668). The magenta lines illustrate the acceptance cuts. Colour scale on right corresponds to number of events in histogram bins.

Chapter 5

Peak Search

The peak search of the final invariant mass spectrum comprised several stages. After calibrations and cuts for the analysis were finalised (as described in chapter 4), the invariant mass resolution had to be determined as a function of invariant mass (this will determine the width of a potential A′ resonance in the invariant mass distribution). An updated methodology for the peak search was adopted from the HPS experiment [2] for this analysis compared to that used for the APEX 2010 test run. This is described in detail, allowing a more powerful exclusion zone to be determined and making the results more directly comparable to those from other A′ searches. The methodologies for the initial peak search to determine p-values (probability of obtaining a result at least as extreme as observed) for the presence of an A′ peak (including the Look Elsewhere Effect) and the setting of upper limits for the number of signal events are detailed. The radiative fraction, the proportion of radiative tridents to overall background, had to be determined as a function of invariant mass to translate the limit for signal events found in the peak search to a limit in ϵ^2.

Testing of the parameters used in the model for the background were performed on a blinded (10%) invariant mass spectrum. Due to time constraints the stage of 'unblinding' (moving to 100% of the data for the final result) was not reached, results for the discovery p-values (testing for presence of the resonance) and upper limits are presented for the blinded search.

5.1 Invariant Mass Distribution

The invariant mass (squared), m_0^2, of an e^+e^- pair can be expressed in terms of the energy (E_{e^+},E_{e^-}) and momentum ($\vec{p}_{e^+}$,$\vec{p}_{e^-}$) of the pair:

$$m_0^2 = (E_{e^+} + E_{e^-})^2 - (\vec{p}_{e^+} + \vec{p}_{e^-}). \tag{5.1}$$

This can be reformulated by substituting in $m_{e^\pm}^2 = E_{e^\pm}^2 - \vec{p}_{e^\pm}^2$ and taking $m_{e^\pm}$ to be negligible:

$$m_0^2 = 2E_{e^+}E_{e^-} - 2(\vec{p}_{e^+} \cdot \vec{p}_{e^-}), \tag{5.2}$$
$$m_0^2 = 2(|\vec{p}_{e^+}||\vec{p}_{e^-}| - (p_{e^+,x}p_{e^-,x} + p_{e^+,y}p_{e^-,y} + p_{e^+,z}p_{e^-,z})), \tag{5.3}$$

where $p_{e^\pm,x}, p_{e^\pm,y}, p_{e^\pm,z}$ are the components of the momentum as defined in the HCS ($\hat{z}$ in positive beam direction, $\hat{x}$ towards the left facing along $\hat{z}$ and $\hat{y}$ upwards).

The HRS records track coordinates in the focal plane which are then transferred to the target (in the TCS frame) using the optics matrix. These coordinates in the TCS, the dispersive and non-dispersive angles θ_{tg} and ϕ_{tg}, and the momentum deviation, δp, can be converted into the momentum components in the HCS:

$$p_{z,tg} = \frac{p_0(1+\delta)}{\sqrt{1 + \tan^2(\theta_{tg}) + \tan^2(\phi_{tg})}}, \tag{5.4}$$
$$p_x = p_{z,tg}(\tan(\phi_{tg})\cos(\theta_0) + \sin(\theta_0)), \tag{5.5}$$
$$p_y = p_{z,tg}\tan(\theta_{tg}), \tag{5.6}$$
$$p_z = p_{z,tg}(\cos(\theta_0) - \tan(\phi_{tg})\sin(\theta_0)), \tag{5.7}$$

where θ_0 is the central angle and p_0 the central momentum of the HRS (described in 3.5.5).

The final number of e^+e^- pairs produced, and surviving all cuts, was ~52 million in an invariant mass range of ~125-233 MeV. This represents (an expected) large increase from the 2010 APEX test run which had a final event sample of ~0.77 million pairs. A blinded (10%) invariant mass spectrum is shown in figure 5.1 (with 0.15 MeV binning).

When selecting the mass range over which the peak search was carried out, a cutoff of 1,000 events in the blinded spectrum per bin (of size 0.15 MeV) was applied. This resulted in a mass range of 120 (MeV) $\leq m_H \leq$ 230 (MeV), where m_H is a mass hypothesis, a proposed mass for the A′.

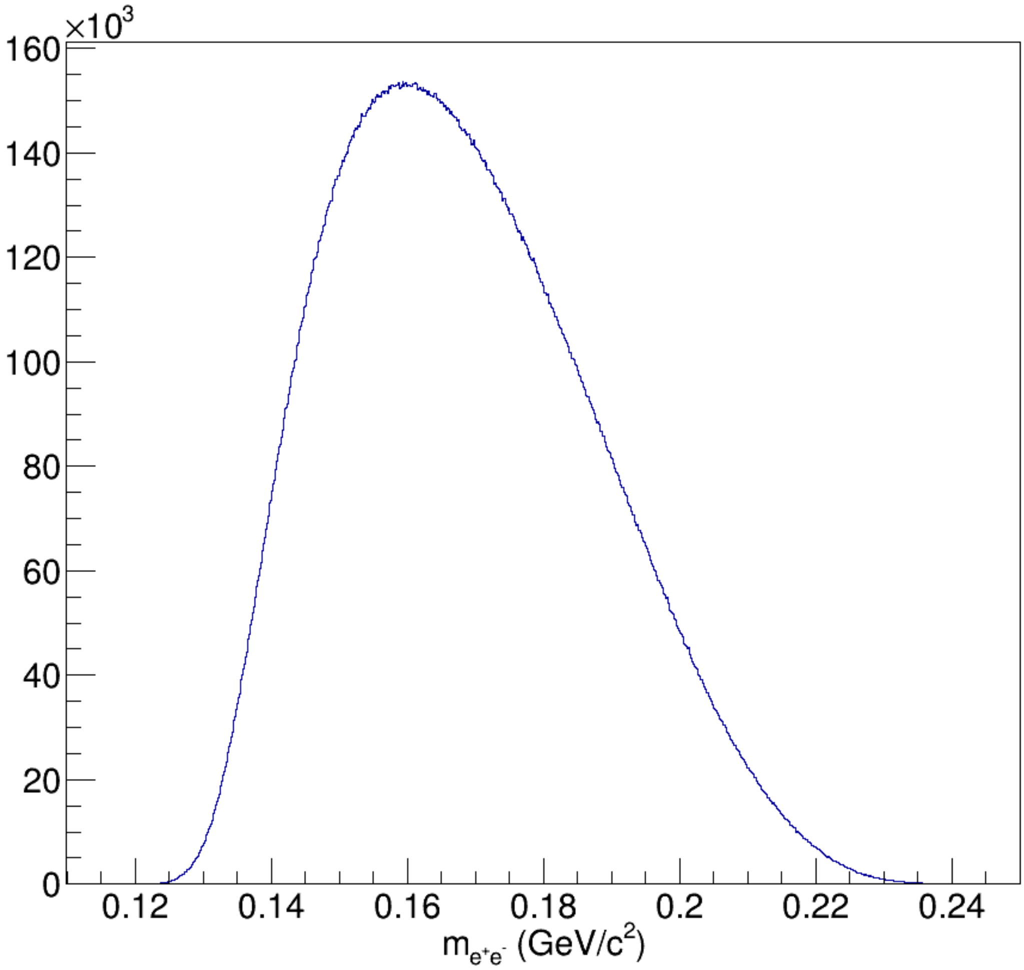

Figure 5.1: Blinded 10% invariant mass spectrum from final event sample of e^+, e^- pairs, with 0.15 MeV/c^2 bin size.

5.2 Invariant Mass Resolution

The peak search will look for a gaussian peak of A′ decays on top of a QED background. The width of a potential A′ resonance will be equal to the invariant mass resolution, as this is much larger than the A′ partial decay width for the values of ϵ^2 probed (as explained in section 2.1, with the partial decay width given by equation 2.3). The invariant mass resolution must then be determined over the invariant mass spectrum being searched.

The invariant mass resolution, σ_m, can be split into contributions [22]:

$$\left(\frac{\sigma_m}{m}\right)^2 \approx \left(\frac{\sigma_p}{p}\right)^2 + 0.5\left(\frac{\sigma_{\theta_{tg}(\phi_{tg})}}{\theta_{pair}}\right)^2, \tag{5.8}$$

where σ_p is the momentum resolution, $\sigma_{\theta_{tg}(\phi_{tg})}$ is the angular resolution (vertical or horizontal) of the HRS and θ_{pair} is the angle between the e^+ and e^-. The momentum resolution is 9.35×10^{-4} as described in section 4.5.5. To examine the significance of the momentum resolution contribution to the invariant mass resolution, it can be compared to the contribution from the angular resolution. A crude estimation can be made by taking the angular resolution used in equation 5.8 to be the mean of the vertical and horizontal angular resolutions for both arms, $\sigma_{\bar{\theta},\bar{\phi}} = 1.15$ mrad. This results in an angular contribution of $\sigma_{\bar{\theta},\bar{\phi}}/\theta_{pair} \simeq (1.15)/174.5 = 6.59 \times 10^{-3}$. Here θ_{pair} is taken to be 10° (sum of central angles for both HRS arms), expressed in mrad. As the components of the invariant mass resolution are summed in quadrature, this leaves the angular resolution to be the dominant contribution.

5.2.1 Angular Resolution

The angular resolutions can be split into two contributions:

$$\sigma^2_{\theta_{tg}(\phi_{tg})} = \sigma^2_{\theta_{tg}(\phi_{tg}),HRS} + \sigma^2_{MS}, \tag{5.9}$$

where $\sigma_{\theta_{tg}(\phi_{tg}),HRS}$ is the HRS angular resolution (from optics) and σ_{MS} is the contribution from multiple scattering. The HRS angular resolutions are discussed in section 4.5.3. The multiple scattering contribution is due to Coulomb scattering in the target, which causes small angle deflections that degrade the angular resolution. The resulting contribution is given by the formula [28]:

$$\sigma_{\theta,MS} = \frac{13.6}{p[\mathrm{MeV}]}\sqrt{\frac{t}{X_0}}\left[1 + 0.038 \ln\left(\frac{t}{X_0}\right)\right], \tag{5.10}$$

where X_0 is the radiation length (g/cm^2) of the target material, t is the target thickness in radiation lengths of the material along the particle path and p[MeV] is the momentum of the particle in MeV. The APEX production target consisted of 10 micron thick tungsten foils (as described in section 3.7). The segmented design of the target is designed to limit multiple scattering to one individual foil, giving a value for the full thickness of $\frac{t}{X_0} = 0.0028$. The assumption is made that the mean vertex position in a foil is half-way through its thickness, thus giving an effective mean thickness of $\frac{t}{X_0} = 0.0014$. With $p = 1063$ MeV, this gave a value for the multiple scattering contribution of $\sigma_{\theta,MS} = 0.36$ mrad. This was also tested with a Geant4 [89] simulation of the production foils. This resulted in a mean value of $\sigma_{\theta,MS} = 0.35$ mrad with a relatively small variation across the foils, a standard deviation of 0.007 mrad. This is consistent with the result from calculation and the small discrepancy between the two would have minimal effect on the analysis, especially as this is combined in quadrature with the angular resolutions from optics (for both θ_{tg} and ϕ_{tg}, as described in equation 5.9). It was decided to move forward with the value from calculation, $\sigma_{\theta,MS} = 0.36$ mrad, as this is slightly more cautious (though the difference between using this and the value from simulation would be negligible).

5.2.2 Invariant Mass Resolution

To perform the peak search the invariant mass resolution must be determined as a function of invariant mass. The procedure for determining the invariant mass resolution used events recorded from several production runs. The angles and momenta of these events were smeared by MC in accordance with the determined resolutions, and the initial and modified invariant masses were then compared. For each event the resolutions for both arms ($\sigma_{\theta_{tg}}$, $\sigma_{\phi_{tg}}$ and $\sigma_{\delta p}$) were sampled randomly with a gaussian, and this was used to alter the initial variables (θ_{tg}, ϕ_{tg} and δp) into modified versions (θ'_{tg}, ϕ'_{tg} and $\delta p'$):

$$\theta'_{tg,i} = \theta_{tg,i} + Gaus(\sigma_\theta), \tag{5.11}$$

$$\phi'_{tg,i} = \phi_{tg,i} + Gaus(\sigma_\phi), \tag{5.12}$$

$$\delta p' = \delta p + Gaus(\sigma_{\delta p}). \tag{5.13}$$

The modified variables were then used to calculate a new invariant mass, m'_0, using equation 5.3 which was compared with the initial invariant mass, m_0. The width of the $(m'_0 - m_0)$ distribution (assumed to be Gaussian) is then taken to be the invariant mass resolution. The angular resolutions were determined from optics data from the vertical wire targets, so for an event the correct wire to use was determined by the reconstructed z position from both arms:

$$\delta z_i = \sqrt{(z_L^r - z_i^s)^2 + (z_R^r - z_i^s)^2}, \tag{5.14}$$

where z_L^r and z_R^r are the reconstructed vertices from the LHRS and RHRS respectively and z_i^s is the position of the i$^{\text{th}}$ vertical wire (from survey). The vertical wire selected was that with minimal δz_i. An analogous process was used to determine which sieve hole to select a resolution from:

$$\delta A_i = \sqrt{(\theta_{tg}^r - \theta_i^s)^2 + (\phi_{tg}^r - \phi_i^s)^2}, \tag{5.15}$$

where for each arm θ_{tg}^r and ϕ_{tg}^r are the reconstructed target angles, and for the i$^{\text{th}}$ hole θ_i^s and ϕ_i^s are the angles in the target frame (from survey). The sieve hole with minimal δA_i was selected, and the corresponding values for σ_θ and σ_ϕ used in equations 5.12 and 5.13. The angular resolutions for each sieve hole are obtained from the process described in section 4.5.3. Note that the vertical wire is selected for both arms, then the correct sieve hole (from which σ_θ and σ_ϕ are obtained) is selected separately for each arm.

For the purposes of the peak search it is necessary to obtain the invariant mass resolution at each mass hypothesis. Equivalently the invariant mass resolution had to be found as a function of invariant mass, $\sigma_m = S_{\sigma_m}(m)$. This was achieved by the method described above, and using a large number of events the invariant mass resolution (defined as σ of an assumed Gaussian distribution of $(m_0 - m_0'))$ was plotted as function of mass, as shown in figure 5.2. The distribution of σ_m versus m was then fitted with different order polynomials to determine the optimal fit. It was found that a fourth order polynomial was most suitable, this was the highest order that passed an F-test (higher F-statistic than threshold given degrees of freedom and number of parameters). The fourth order polynomial fit, $S_{\sigma_m}(m)$, is shown as a red line on figure 5.2. This parameterises the invariant mass resolution as:

$$S_{\sigma_m}(m) = 25.849m^4 - 18.589m^3 + 4.864m^2 - 0.545m + 0.0229, \tag{5.16}$$

where the mass, m, is given in GeV.

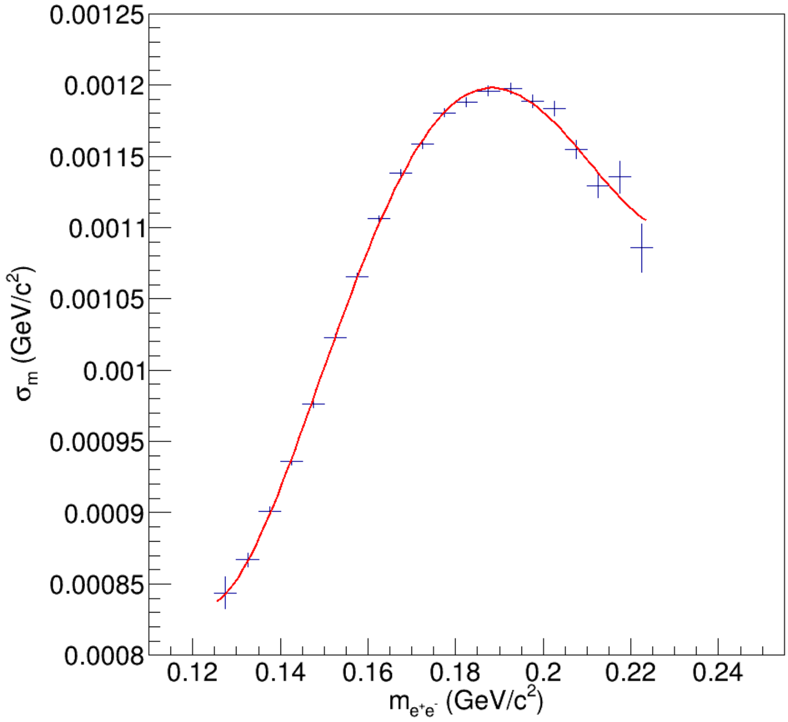

Figure 5.2: Invariant mass resolution as a function of invariant mass. Calculated using determined resolutions in θ_{tg}, ϕ_{tg} and δp. Red line shows fourth order polynomial fit, judged to be optimal.

5.3 Peak Search Overview

The final stage of the APEX analysis is the search for an A' resonance in the e^+e^- invariant mass spectrum. Firstly the A' is searched for as a Gaussian peak over the full experimental invariant mass range, with p-values determined at each mass hypothesis, m_H. 'Discovery' of the A' is established at a mass hypothesis if a p-value equivalent to 5σ in Z (deviations from the mean of a Gaussian distribution, discussed in section 5.4.2 and given by equation 5.25) is obtained. If no discovery is made then upper limits for the number of signal events at each mass are established. This is then converted into a limit in terms of ϵ^2 (as in equation 2.13, equivalent to $\frac{\alpha'}{\alpha}$) to obtain a final exclusion plot. The statistical underpinnings of these processes are discussed in the following subsections.

The model used to fit the experimental invariant mass distribution (referred to here as the background) was an exponential Legendre polynomial. The model parameters included the width of the mass window fitted over and the polynomial order. These parameters were tested on a 10% blinded spectrum to ensure set conditions were met whilst trying to optimise search sensitivity. Results for the blinded search are presented: p-values for discovery, and upper limits in number of signal events and ϵ^2.

For the APEX 2019 blinded search a step size between mass hypotheses of 0.25 MeV was used (this must be smaller than the mass resolution). The total mass range searched was 120 (MeV) $\leq m_H \leq$ 230 (MeV). The search was performed with the HPS peak search code [90].

5.4 Peak Search Methodology

The presence of an A' resonance is searched for as a Gaussian peak over the background. The potential mass of the A' is unknown so the invariant mass range is scanned, searching for a 'bump' at several mass hypotheses. At each m_H the gaussian signal is fitted along with the background (modelled by an exponential Legendre polynomial) over a mass window centred at the mass hypothesis. The size of the mass window, w_s, is equal to the invariant mass resolution at the mass hypothesis multiplied by an integer: $w_s = n_\sigma \sigma_m$. An exception to this occurs if the mass hypothesis is close to the end of the invariant mass range then the end of the window is moved to coincide with end of the mass range. The probability density function (PDF) describing the signal plus background fit is:

$$P(m_{e^+e^-}) = \mu \cdot \phi(m_{e^+e^-}|m_{A'}, \sigma_{m_{A'}}) + 10^{L_N(m_{e^+e^-}|\vec{t})}, \tag{5.17}$$

where $m_{e^+e^-}$ is the e^+e^- pair invariant mass, μ is the signal yield, $\phi(m_{e^+e^-}|m_{A'}, \sigma_{m_{A'}})$ is the gaussian PDF modelling the signal (with $\sigma = \sigma_m$) and $L_N(m_{e^+e^-}|\vec{t})$ is a Legendre polynomial of order N with parameters $\vec{t} = (t_1, t_2, ..., t_N)$ modelling the background.

5.4.1 Profile Likelihood Ratio

For discovery, an unconstrained fit described by equation 5.17 is performed (H_1) and compared to a constrained, background-only fit where $\mu = 0$ (H_0), at each mass hypothesis . In other terminology, for signal discovery, the null hypothesis, H_0, is a background-only fit which can be compared to the alternate hypothesis, H_1, of the optimal signal plus background fit. The p-value is the probability of obtaining a result at least as extreme as observed under the assumption of the null hypothesis that there is no A′ resonance at that mass and hence no signal events.

If a mass window used in fitting has N bins, $\vec{n} = (n_1, n_2, ..., n_N)$, then the expected number of events in the i$^{\text{th}}$ bin is given by [91]:

$$E[n_i] = S_i + B_i. \tag{5.18}$$

Here S_i is the number of signal events and B_i the number of background events in the bin, and they are given by [91]:

$$S_i = \mu \int_{bin,i} \phi(m_{e^+e^-} | m_{A'}, \sigma_{m_{A'}}) d(m_{e^+e^-}), \tag{5.19}$$

$$B_i = B_{tot} \int_{bin,i} 10^{L_N(m_{e^+e^-} | \vec{t})} d(m_{e^+e^-}), \tag{5.20}$$

where B_{tot} is the total number of background events. The 'nuisance parameters' (parameters of the background model not of interest) are denoted as $\vec{\theta}$. The Likelihood can then be defined, for a specific μ and $\vec{\theta}$, as the product of the Poisson probabilities for all bins [91]:

$$\mathcal{L}(\mu, \vec{\theta}) = \prod_{j=1}^{n_{bins}} \frac{(S_j + B_j)}{n_j!} e^{S_j + B_j}. \tag{5.21}$$

The likelihoods of the null (no signal) and alternative (unconstrained fit with signal) hypotheses can be compared through the profile likelihood ratio (PLR):

$$\lambda(\mu) = \frac{L(\mu, \vec{\theta}_\mu)}{L(\hat{\mu}, \vec{\theta}_{\hat{\mu}})}, \tag{5.22}$$

where $L(\mu, \vec{\theta}_\mu)$ denotes the likelihood of the null hypothesis with number of signal events, μ, and $\vec{\theta}_\mu$ the conditional maximum-likelihood estimator (MLE) of $\vec{\theta}$, and $L(\hat{\mu}, \vec{\theta}_{\hat{\mu}})$ denotes the unconditional likelihood function, with $\hat{\mu}$ and $\vec{\theta}_{\hat{\mu}}$ the unconstrained MLEs ($\hat{\mu}$ is the number of signal events found by a background plus signal fit). The PLR can itself be used as a test statistic for certain analyses (and if there are no nuisance parameters the PLR is the most powerful statistical test, as given by the Neyman-Pearson lemma [92]). The PLR is bound, $0 \leq \lambda(\mu) \leq 1$, where $\lambda(\mu)$ close to 1 indicates agreement with H_0 and $\lambda(\mu)$ close to 0 indicates disagreement.

5.4.2 Discovery Test Statistics

For the peak search a test statistic related to the PLR, as used by the ATLAS experiment [93], was employed for discovery:

$$\tilde{q}_0 = \begin{cases} -2\ln\lambda(0) & \hat{\mu} > 0, \\ +2\ln\lambda(0) & \hat{\mu} \leq 0. \end{cases} \tag{5.23}$$

This is modified compared to the formula for discovery as in [91], by changing the definition of q_0 under condition $\hat{\mu} \leq 0$ from being equal to zero. This alteration is made to probe p-values over 0.5.

A p-value (probability of obtaining a result at least as extreme as observed if H_0 is true) can be extracted from the test statistic as:

$$p = \int_{\tilde{q}_{0,obs}}^{\infty} f(\tilde{q}_0|0)dq_0, \tag{5.24}$$

where $f(q_0|0)$ is the PDF of $\tilde{q}_0$. For signal searches in physics the p-value is often converted into an equivalent measure Z that is defined by the number of standard deviations above the mean of a Gaussian distributed variable:

$$Z = \Phi^{-1}(1-p), \tag{5.25}$$

where Φ^{-1} is the inverse of the cumulative distribution function (CDF) of a Gaussian distribution. The widely established standard for discovery in particle searches is $Z = 5\sigma$, equivalent to a threshold for the p-value, termed α_{disc}, of 2.87×10^{-7} (though some argue this is an arbitrary standard to apply to all experiments [94]).

The Wald approximation can be used to show, for a single parameter of interest and for sufficiently large N (sample size), that: [95]

$$-2\ln\lambda(\mu) = \frac{(\mu-\hat{\mu})^2}{\sigma^2} + \mathcal{O}(1/\sqrt{N}), \tag{5.26}$$

where $\hat{\mu}$ is Gaussian distributed, with mean μ' and standard deviation σ (under conditions $\mu' = \mu$ then $-2\ln\lambda(\mu)$ approaches a χ^2 distribution with one degree of freedom and reduces to the Wilks theorem [91] [96]).

For the discovery test statistic, $\tilde{q}_0$ (equation 5.23), using the result from equation 5.26 with the null hypothesis having $\mu = 0$ it can be shown that:

$$\tilde{q}_0 = \begin{cases} \hat{\mu}^2/\sigma^2 & \hat{\mu} > 0, \\ -\hat{\mu}^2/\sigma^2 & \hat{\mu} \leq 0. \end{cases} \tag{5.27}$$

It can then be shown that the PDF for $\tilde{q}_0$, $f(\tilde{q}_0|0)$, takes the form:

$$f(\tilde{q}_0|0) = \begin{cases} \frac{1}{2}\delta(\tilde{q}_0) + \frac{1}{2}\frac{1}{\sqrt{2\pi}}\frac{1}{\sqrt{\tilde{q}_0}}e^{-\frac{\tilde{q}_0}{2}} & \hat{\mu} > 0, \\ \frac{1}{2}\delta(-\tilde{q}_0) + \frac{1}{2}\frac{1}{\sqrt{2\pi}}\frac{1}{\sqrt{-\tilde{q}_0}}e^{\frac{\tilde{q}_0}{2}} & \hat{\mu} \leq 0. \end{cases} \tag{5.28}$$

The PDF found in Equation 5.28 can be labelled as a 'half chi-square distribution' or $\frac{1}{2}\chi_1^2$: the sum of a delta function at zero and a chi-square PDF for one degree of freedom, each weighted by $\frac{1}{2}$ [91]. Equation 5.24 can be reinstated in terms of the CDF of $\tilde{q}_0$, $F(\tilde{q}_0)$, as:

$$p = 1 - F(\tilde{q}_0|0). \tag{5.29}$$

From equation 5.28 it can be shown that:

$$F(\tilde{q}_0|0) = \begin{cases} \Phi(\sqrt{\tilde{q}_0}) & \hat{\mu} > 0, \\ \Phi(-\sqrt{-\tilde{q}_0}) & \hat{\mu} \leq 0. \end{cases} \tag{5.30}$$

Combining the result from equation 5.29 from with 5.30, an expression for the p-value for discovery can be obtained:

$$p = \begin{cases} 1 - \Phi(\sqrt{\tilde{q}_0}) & \hat{\mu} > 0, \\ 1 - \Phi(-\sqrt{-\tilde{q}_0}) & \hat{\mu} \leq 0. \end{cases} \tag{5.31}$$

5.4.3 The Look Elsewhere Effect

For discovery the p-values obtained (given by equation 5.31) have to be corrected for the 'Look Elsewhere Effect' (LEE). The mass of the A' is not known a priori, hence mass hypotheses over the entire mass range are tested. The p-value obtained for a mass hypotheses is then compared to the threshold for discovery, $\alpha_{disc} = 2.87 \times 10^{-7}$. The more mass hypotheses searched for, however, the greater the likelihood of a statistical fluctuation resulting in a p-value meeting the threshold. This statistical effect is a well-known feature of physics searches. Labelling the p-values obtained from the search as p_{local}, then if $p_{local} \ll 1$ this effect can be corrected for by using 'global' p-values, p_{global} defined as [97]:

$$p_{global} = N_{regions} \times p_{local}, \tag{5.32}$$

where $N_{regions}$ is the number of independent regions searched. The step size used in the APEX search was 0.25 MeV, smaller that the $\sim$1 MeV mass resolution of the experiment. Adjacent search regions are thus not independent of one another and an approximation for $N_{regions}$ is used:

$$N_{regions} \approx \frac{W}{\bar{\sigma}_m}, \tag{5.33}$$

where W is the width of the entire mass range and $\bar{\sigma}_m$ is the mean invariant mass resolution across the entire mass range. This resulted in a value of $N_{regions} = 80.91$.

It is equivalent to keep the local p-values, but use the LEE correction to modify the thresholds for significance. For the threshold for $X\sigma$ significance ($Z = X\sigma$), $\alpha_{X\sigma}$:

$$\alpha_{X\sigma} \rightarrow \alpha_{X\sigma}/N_{regions}. \tag{5.34}$$

In this notation, $\alpha_{disc} = \alpha_{5\sigma}$, and with the LEE corrections becomes 3.54×10^{-9}.

5.4.4 Setting Upper Limits

If an A' resonance is not found in the peak search, upper limits for ϵ^2 are established for the invariant mass range searched: an 'exclusion zone' is established in the parameter space $P(m_{A'}, \epsilon^2)$. The limits in ϵ^2 are converted from upper limits in signal yield (conversion described in section 5.5). The first step is thus establishing upper limits in signal yield, denoted μ_{up}.

The PLRs and corresponding test statistics used in this process are different from those used in discovery (equations 5.22 and 5.23) and again follow from those described by the ATLAS collaboration [93]. The null hypothesis, H_0, is defined as there being a signal yield μ, with the alternative hypothesis, H_1, defined as having a signal yield of $\mu_{H_1} \neq \mu$. From this a PLR can be formed [91]:

$$\tilde{\lambda}(\mu) = \begin{cases} \frac{L(\mu,\vec{\theta}_{\mu})}{L(\hat{\mu},\vec{\theta}_{\hat{\mu}})} & \hat{\mu} \geq 0, \\ \frac{L(\mu,\vec{\theta}_{\mu})}{L(0,\vec{\theta}_{0})} & \hat{\mu} < 0, \end{cases} \tag{5.35}$$

with $L(\mu, \vec{\theta}_{\mu})$ as the likelihood of the null hypothesis, and either $L(\hat{\mu}, \vec{\theta}_{\hat{\mu}})$ or $L(0, \vec{\theta}_0)$ the likelihood of the alternative (depending on sign of $\hat{\mu}$). The definition of $\hat{\mu}$ here is the same as for discovery, the signal yield of an unconstrained background plus signal fit. The corresponding test statistic is then defined as:

$$\tilde{q}_{\mu} = \begin{cases} -2\ln\tilde{\lambda}(\mu) & \hat{\mu} \leq \mu, \\ +2\ln\tilde{\lambda}(\mu) & \hat{\mu} > \mu, \end{cases} \tag{5.36}$$

where $\tilde{q}_{\mu}$ has again been modified from the expression given in [91], by altering the definition under condition $\hat{\mu} > \mu$ from zero in order to probe p-values over 0.5. Assuming the Wald approximation, with $\hat{\mu}$ being gaussian distributed with a mean of μ' and standard deviation of σ, then $\tilde{q}_{\mu}$ can be restated as [91]:

$$\tilde{q}_{\mu} = \begin{cases} \frac{\hat{\mu}^2}{\sigma^2} - \frac{2\mu\hat{\mu}}{\sigma^2} & \hat{\mu} < 0, \\ \frac{(\mu-\hat{\mu})^2}{\sigma^2} & 0 \leq \hat{\mu} \leq \mu, \\ -\frac{(\mu-\hat{\mu})^2}{\sigma^2} & \hat{\mu} > \mu, \hat{\mu} \geq 0. \end{cases} \tag{5.37}$$

The associated PDF given equation 5.37 is then:

$$f(\tilde{q}_{\mu}|\mu') = \begin{cases} \Phi(\frac{\mu'-\mu}{\sigma})\delta(\tilde{q}_{\mu}) + \frac{1}{\sqrt{2\pi}(2\mu/\sigma)} e^{-\frac{1}{2}\frac{(\tilde{q}_{\mu}-(\mu^2-2\mu\mu')/\sigma^2)^2}{(2\mu/\sigma)^2}} & \tilde{q}_{\mu} > \mu^2/\sigma^2, \\ \Phi(\frac{\mu'-\mu}{\sigma})\delta(\tilde{q}_{\mu}) + \frac{1}{2}\frac{1}{\sqrt{2\pi}}\frac{1}{\sqrt{\tilde{q}_{\mu}}} e^{-\frac{(\sqrt{\tilde{q}_{\mu}}-(\mu-\mu')/\sigma)^2}{2}} & 0 \leq \tilde{q}_{\mu} < \mu^2/\sigma^2, \\ \Phi(\frac{\mu'-\mu}{\sigma})\delta(-\tilde{q}_{\mu}) + \frac{1}{2}\frac{1}{\sqrt{2\pi}}\frac{1}{\sqrt{-\tilde{q}_{\mu}}} e^{-\frac{(-\sqrt{\tilde{q}_{\mu}}-(\mu-\mu')/\sigma)^2}{2}} & \tilde{q}_{\mu} < 0. \end{cases} \tag{5.38}$$

The corresponding CDF is:

$$F(\tilde{q}_\mu|\mu') = \begin{cases} \Phi(\frac{\tilde{q}_\mu-(\mu^2-2\mu\mu')/\sigma^2}{2\mu/\sigma}) & \tilde{q}_\mu > \mu^2/\sigma^2, \\ \Phi(\sqrt{\tilde{q}_\mu} - \frac{\mu-\mu'}{\sigma}) & 0 \leq \tilde{q}_\mu < \mu^2/\sigma^2, \\ \Phi(-\sqrt{-\tilde{q}_\mu} - \frac{\mu-\mu'}{\sigma}) & \tilde{q}_\mu < 0. \end{cases} \tag{5.39}$$

One method of limit setting would be to define a p-value, p_μ, from the given null and alternative hypotheses, with signal yields of μ and $\mu_{H_1} = \hat{\mu}$ respectively. Starting with a value of $\mu > \hat{\mu}$ and iterating μ until a set p-value, 'α_{lim}', was reached. If the mass spectrum being examined, however, is consistent with little to no signal then downward statistical fluctuations of the background can, with this method, result in an upper limit of $\mu_{up} < 0$. This would then result in extreme exclusion when translated into ϵ^2. In other words, this method by itself would lack sensitivity when the signal yield is negative. The p-value described here can also be labelled as CL_{s+b}, the confidence level in the signal plus background hypothesis.

This method was used in the APEX 2010 analysis, with $\alpha_{lim} = 0.1$ (90% confidence). In the APEX 2010 analysis the potential underestimation of μ_{up} was resolved by the use of a 50% power-constrained limit [98]. For this method peak searches are carried out on a large number of pseudo-datasets, for the APEX 2010 analysis these were generated from a toy function that modelled the entire invariant mass spectrum [68]. A 'median limit', μ_{med}, at a mass hypothesis is taken as the median of signal upper limits at that mass obtained from the pseudo-datasets. The power constrained upper limit, 'μ_{pc}', is then taken as the maximum of μ_{up} and μ_{med}. For the 2019 analysis a median limit, μ_{med}, was calculated from pseudo-experiments generated from the background only fit (as described in section 5.6). This was not used to obtain the upper limits, but as a reference.

For the 2019 APEX analysis the CL_s method is used to set upper limits for the signal [99, 100]. Also known as the 'Modified Frequentist confidence level', it is calculated as:

$$CL_s(\mu) \equiv \frac{CL_{s+b}(\mu)}{CL_b(\mu)} = \frac{p_\mu}{1-p_b}, \tag{5.40}$$

where CL_{s+b} is scaled by CL_b, the confidence level in the background-only hypothesis. Starting at a value of $\mu = \hat{\mu} + 1.64\sigma$, the value of μ is increased until the target threshold confidence of $\alpha_{lim} = 0.05$ is reached. This process is continued iteratively until the $CL_s(\mu)$ value is within 0.001 of α_{lim}, with the step size dependent on the difference between $CL_s(\mu)$ and α_{lim}. The motivation for use of the CL_S is to improve sensitivity for exclusion, note that by construction upper limits set by using the CL_S must be greater than zero (if $\mu = 0$ then $CL_{s+b} = CL_b \implies CL_s = 1$). Using the CL_s to set upper limits rather than CL_{s+b} will result in more conservative upper limits.

For the case of signal plus background the null hypothesis (that there is number of signal events μ) means that $\mu' = \mu$ in equations 5.38 and 5.39. With this substitution then the resulting p-value, as related to the CDF in an analogous manner to equation 5.29, can be expressed as:

$$p_\mu = \begin{cases} 1 - \Phi(\frac{\tilde{q}_\mu + \mu^2/\sigma^2}{2\mu/\sigma}) & \tilde{q}_\mu > \mu^2/\sigma^2, \\ 1 - \Phi(\sqrt{\tilde{q}_\mu}) & 0 \leq \tilde{q}_\mu < \mu^2/\sigma^2, \\ 1 - \Phi(-\sqrt{-\tilde{q}_\mu}) & \tilde{q}_\mu < 0. \end{cases} \tag{5.41}$$

For the case of only background the null hypothesis (that there are no signal events) $\mu' = 0$ can be substituted into equations 5.38 and 5.39. The resulting p-values are then:

$$p_b = \begin{cases} 1 - \Phi(\frac{\tilde{q}_\mu - \mu^2/\sigma^2}{2\mu/\sigma}) & \tilde{q}_\mu > \mu^2/\sigma^2, \\ 1 - \Phi(\sqrt{\tilde{q}_\mu} - \mu/\sigma) & 0 \leq \tilde{q}_\mu < \mu^2/\sigma^2, \\ 1 - \Phi(-\sqrt{-\tilde{q}_\mu} - \mu/\sigma) & \tilde{q}_\mu < 0. \end{cases} \tag{5.42}$$

For calculating p_μ and p_b the value σ is taken as the uncertainty on $\hat{\mu}$ in the signal plus background fit.

5.5 Translation to ϵ^2

To obtain the final results, an exclusion region in $P(m_{A'}, \epsilon^2)$, the upper limit of number of signal events at each mass hypothesis must be translated to a limit in ϵ^2. Discussion of the background present for the APEX measurement is in section 2.4, which leads to an expression for ϵ^2 related to the ratio of the cross sections for A′ production and radiative trident events, equation 2.15. This can be re-expressed in terms of the measured outputs from the peak search:

$$\epsilon^2 = \frac{1}{f} \frac{\mu_{up}}{(B/\delta m)} \frac{2N_{eff}\alpha}{3\pi m_{A'}}, \tag{5.43}$$

where $(B/\delta m)$ is the number of background events evaluated in a 1 MeV window around the mass hypothesis being tested. With this definition $(B/\delta m)$ has units of MeV^{-1}, so the mass, $m_{A'}$, must be expressed in units of MeV such that ϵ^2 is dimensionless.

It is thus necessary to have accurate values for both f and N_{eff} in equation 5.43, in order to calculate the upper limits in ϵ^2. Equation 2.6 gives an expression for N_{eff} with two cases, for above and below the dimuon threshold ($2m_\mu \simeq 211.32$ MeV). As can be seen from figure 5.1, the mass range probed extends above the dimuon threshold (though the majority of the range is below). N_{eff} was calculated from experimental data for $R(m_{A'})$ [101, 102]. This was then used in the final extrapolation from μ_{up} to ϵ^2 for $m_H \geq 2m_\mu$.

5.5.1 Calculation of the Radiative fraction

For the calculation of the radiative fraction several background components had to be considered. As described in 2.4 there were three main EM backgrounds which resulted in the correct experimental signature (e^+e^-): Bethe-Heitler and radiative tridents and e^+e^- pair photoproduction. In addition to this the 'accidental fraction', the portion of events surviving all cuts which came from accidental coincidences of an e^- in the LHRS and e^+ in the RHRS, had to be considered. This is summarised in equation 2.14.

The value of f, as a function of the invariant mass of the e^+e^- pair, was determined through simulation. This process consisted of several steps:

- MadGraph5 [103] (a MC event generator) was used to generate a 'total trident' event sample consisting of Bethe-Heitler tridents, radiative tridents and their interference, over a phase space wider than the experimental acceptance. This gives the cross-section for total trident processes.
- MadGraph5 was also used to generate a radiative trident event sample consisting of solely radiative tridents, over the same phase space as for the total trident event sample. This gives the cross-section for radiative tridents.
- e^+e^- pair photoproduction was approached differently, and simulated with Geant4. A Geant4 simulation for the APEX target and electron beam was used to calculate the incident bremsstrahlung flux at each target foil. From the bremsstrahlung flux, e^+e^- pair production was generated, with Geant4, at each foil over the same phase space as for the trident calculations (that is, a phase space wider than the detector acceptance). The e^+e^- pair production cross-section was then parameterised as a function of production foil.

- The total trident, radiative trident and e^+e^- pair production cross-sections calculated were used to weight the generation of events at each foil. This was passed on to a full Geant4 simulation with virtual detectors located at the LHRS and RHRS septum entrance windows.
- Virtual detectors in the full simulation recorded the coordinates of e^+ and e^- from which, with the vertex position, the target positions were obtained: θ_{tg}, ϕ_{tg}, δp, y_{tg} and z_{react}. The acceptance cuts on target variables detailed in section 4.6 were applied along with the cuts on momentum sum (section 4.5.5) and z vertex difference (section 4.5.4).
- The accidental fraction was calculated from production data (as described in section 4.2.4). The ratio of real to accidental coincidences was obtained from the the final event sample after all cuts except the coincidence timing cut were applied. The resulting distribution in coincidence time was fitted for the coincidence peak and background. From this the accidental fraction could be extracted as a function of invariant mass.
- The final event samples for all relevant processes could then be plotted as a function of $m_{e^+e^-}$, as shown in the left plot of figure 5.3. Finally the radiative fraction could be obtained as the fraction of radiative trident to total background, and again plotted against invariant mass. This was then fitted to obtain an expression for the radiative fraction as a function of invariant mass, $f(m)$. This is illustrated in the right plot of figure 5.3.
- The final extracted parameterisation of the radiative fraction was:

$$f(m) = -0.000544m + 0.274, \tag{5.44}$$

where the mass, m, is given in MeV. The e^+e^- pair photoproduction contribution to the background increases with invariant mass (as can be seen in the left plot of figure 5.3), in contrast to the relative stability of the proportional contributions from the other sources. This is expected as the bremsstrahlung flux increases with each target the beam traverses, with more downstream targets having wider angles and thus e^+e^- pairs with greater invariant masses ($\theta \sim m_{A'}/E_0$). This explains the decrease in f as a function of m (which would not exist if e^+e^- pair photoproduction were not taken into account). A first order polynomial ($\propto m$) and a reciprocal function ($\propto m^{-1}$) were tested as motivated fits for $f(m)$. The first order polynomial fit (as in equation 5.44) was found to have a marginally smaller

χ^2 and was thus selected, though the difference in the value of $f(m)$ between the fits over the mass range was small.

- Wide-angle bremsstrahlung (WAB) was considered as another form of EM background. WAB events come from a two stage process: firstly beam electrons undergo bremsstrahlung in which the electron is deflected at a wide angle, followed by pair production from the emitted photon where the e^+ takes most of the energy. If the deflected e^- (from the beam) and the e^+ from pair creation of the bremsstrahlung photon are detected in coincidence then this constitutes a WAB event. The WAB contribution was tested with the same procedure as described for e^+e^- pair photoproduction, but was found to have an insignificant contribution to f ($\sim$ 1%) and was thus neglected in the final determination of the radiative fraction.

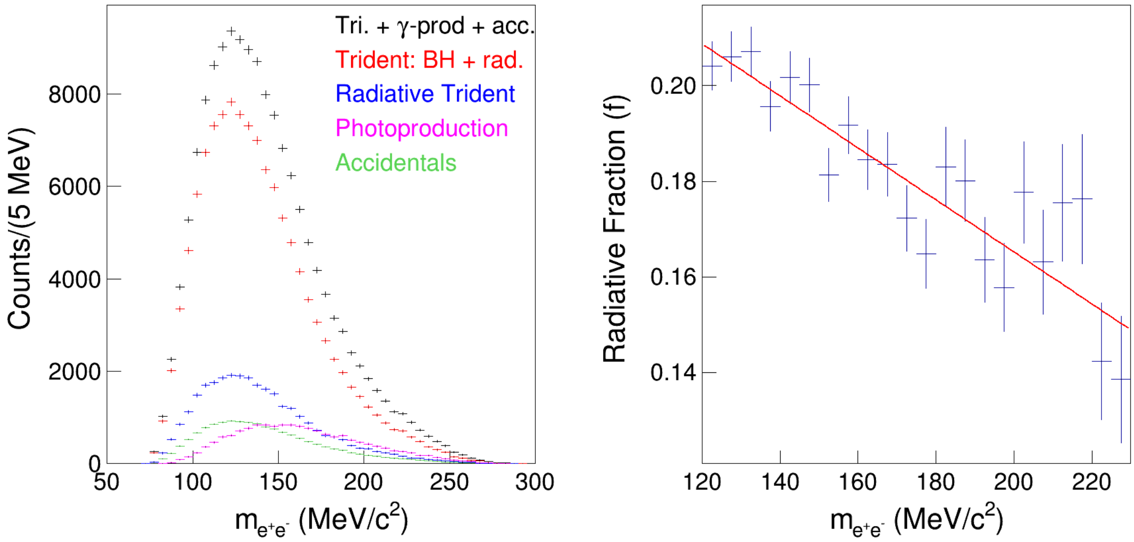

Figure 5.3: Radiative fraction plots. Left histogram shows various contributions to the background over the invariant mass range. Right plot shows the resulting value of f over the invariant mass range, with a first order fit shown in red.

5.6 Blinded Analysis

The purpose of the blinded analysis is to determine the optimal model parameters, the size of the mass window fitted over and the order of the background model, to use when obtaining the final results. As shown in figure 5.1, the blinded analysis was performed on only 10% of the initial data. This is a common procedure, used to avoid biasing choices for the final analysis [104].

The two choices for the background model at each mass hypothesis are the order of the background polynomial, $f_{bg} = 10^{L_N(m_{e^+e^-}|\vec{t})}$, and the size of the mass window, w_s, which is equivalently the choice of n_σ. Increasing n_σ decreases the model complexity and increases the sensitivity of the analysis. Increasing polynomial order, N_{bg}, for f_{bg} increases the model complexity and thus decreases its sensitivity. Both parameters must be sufficiently complex, however, or the model will not be an adequate description of the background and potentially produce false positives.

For the choice of N_{bg} only odd orders, $N_{bg} = (3,5)$, are considered. This is intended to minimise bias of the even signal Gaussian, though as the background is exponential there is still interference. For the window size, values of $n_\sigma = 5$ to $n_\sigma = 46$ were considered for $N_{bg} = 3$ for all masses and $N_{bg} = 5$ for $m_H < 0.16$ GeV, and values of $n_\sigma = 5$ to $n_\sigma = 76$ were considered for $N_{bg} = 5$ for $m_H \geq 0.16$ GeV. Combinations of the values of N_{bg} and n_σ, labelled $C(N_{bg}, n_\sigma)$, were tested at each mass hypothesis.

For each mass hypothesis and applicable $C(N_{bg}, n_\sigma)$, a peak search was performed with background only and background plus signal fits to obtain a p-value for discovery. The upper limit, obtained via the CL_s method (as described in section 5.4.4), was also extracted. An additional background fit was performed with the background order increased by two, e.g. for a background model with order 3 and window size of $n_\sigma = 15$ ($C(3,15)$) an additional background fit with order 5 was performed, $C(5,15)$. This additional background fit was used to define a toy distribution function, $\Xi_{(bg+2)}$. This function was then used to generate 10,000 Monte Carlo distributions each with statistics equal to that in the same mass window of the blinded invariant mass distribution.

Two primary test criteria were used to consider each combination, $C(N_{bg}, n_\sigma)$:

- The χ^2-probability of the background-only fit had to be greater than 10^{-2}. The test is performed on the blinded, 10% invariant mass spectrum so the background model should provide a reasonable fit.

- The 'pull' should be zero. The pull here is evaluated on peak searches performed on the Monte Carlo distributions described above, $\Xi_{(bg+2)}$, and is defined as:

$$Pull = \frac{\hat{\mu} - \mu_{inserted}}{\sigma_{\hat{\mu}}}, \tag{5.45}$$

where $\hat{\mu}$ is defined as in section 5.4.1 as the MLE of the number of signal events, $\sigma_{\hat{\mu}}$ is the error on μ and $\mu_{inserted}$ is the number of signal events inserted. If the background model underfits or overfits the background then the pull may diverge from zero (creating artificially low or high numbers of signal events). For the plots shown zero signal events were inserted into the MC sample ($\mu_{inserted} = 0$).

Plots of the background χ^2-probability and pull for a mass hypothesis of 0.18 GeV can be seen in figures 5.4 and 5.5 respectively. From figure 5.4 it can be seen that the background χ^2-probability, for both third and fifth order, only passes the set-out criteria for a limited number of mass window sizes before failing. A similar observation can be made from figure 5.5, where the condition for the pull, for both third and fifth order, is passed for a number of window sizes before diverging from zero as the window size becomes too large. This occurs as above a certain window size the background model is insufficiently complex to accurately describe the background, hence representing a poor fit of the background (failing the background χ^2-probability condition) and creating artificial numbers of signal events (and failing the condition on the pull).

Using the criteria set-out the maximum sensitivity for a given mass hypothesis and background order would tend towards the largest window size that passed both conditions, as this minimises the model complexity. The blinded search, however, is performed on only 10% of the final invariant mass distribution. When moving to the full peak search, the maximum value of n_σ that passed both conditions might result in a background model that is insufficiently complex. The choice of $C(N_{bg}, n_\sigma)$ is then set-out to be more cautious. The first step of this process is to look at what range of mass window sizes consecutivley pass both criteria for a given mass hypothesis and background order. These 'stable' ranges are shown in figures 5.4 and 5.5 as green shaded areas on the plots for background χ^2-probability and pull. If there are stable ranges for both third and fifth order backgrounds for a mass hypothesis, third order is preferred as it has superior sensitivity. Following the selection methodology used in the analysis of the HPS experiment [105], it was found that selecting the mass window size in the centre of stable ranges was not sufficiently conservative when moving to the full unblinded mass distribution. The choices of $C(N_{bg}, n_\sigma)$ were given over wider regions of the mass distribution, as choosing these for each individual mass hypothesis was found to result in artificial fluctuations. This approach, conservative selection of n_σ and defining wider mass regions for the choices of $C(N_{bg}, n_\sigma)$, was used in the APEX analysis.

An equivalent of the 'median limit', as described in section 5.4.4, was calculated at each mass hypothesis. The median limit was defined on 10,000 distributions from a toy MC generated from the background fit that can be labelled Ξ_{bg}. Peak searches were performed on the 10,000 invariant mass distributions generated, with the median limit, μ_{med}, defined as the median value of the upper limit for all searches. This is illustrated in figure 5.6, which shows the results of performing the peak search on the blinded invariant mass spectrum with $C(N_{bg}, n_\sigma) = (3, 9)$ for all mass hypotheses. For both the upper limit in signal events and the resulting value in ϵ^2, the median limit is shown as a dashed, black line with the corresponding $\pm 1\sigma$ and $\pm 2\sigma$ Confidence Intervals (CIs) around it shown as green and yellow bands respectively.

Dependent on the shape of the distribution and the invariant mass resolution, the allowed window sizes, according to the selection criteria above, vary over the range of mass hypotheses. The final choice of $C(N_{bg}, n_\sigma)$ regions for the blinded invariant mass spectrum had to pass the selection criteria as set out but were also chosen to be more cautious, due to the anticipated changes when shifting to 100% of the data. This was balanced against maximising the sensitivity of the search, which can be done by using larger mass windows. Plots of the upper limit of signals (and resulting ϵ^2) are instructive when considering the effect of increasing the window size. Figure 5.7 shows μ_{up} (solid, black line) as well as μ_{med} (dashed, back line) and its CIs (green and yellow bands for $\pm 1\sigma$ and $\pm 2\sigma$ respectively) plotted against window sizes from $n = 5\sigma$ to $n = 26\sigma$ at 0.180 GeV (blinded search). The gain in sensitivity with increasing window size is greatest at smaller window sizes and diminishes as the window size increases. This should be taken into account when selecting the final window size regions. Another factor to consider is potential discontinuities in the upper limits established when changing from one $C(N_{bg}, n_\sigma)$ region to the next. With all of these elements taken into consideration the final model parameters used for the blinded search were:

$$C(N_{bg}, n_\sigma) = \begin{cases} N_{Bg} = 3, n_\sigma = 9 & m_H < 144 \text{ (MeV)}, \\ N_{Bg} = 3, n_\sigma = 11 & 144 \leq m_H < 165 \text{ (MeV)}, \\ N_{Bg} = 3, n_\sigma = 12 & 165 \leq m_H < 216 \text{ (MeV)}, \\ N_{Bg} = 3, n_\sigma = 11 & 216 < m_H \text{ (MeV)}. \end{cases} \tag{5.46}$$

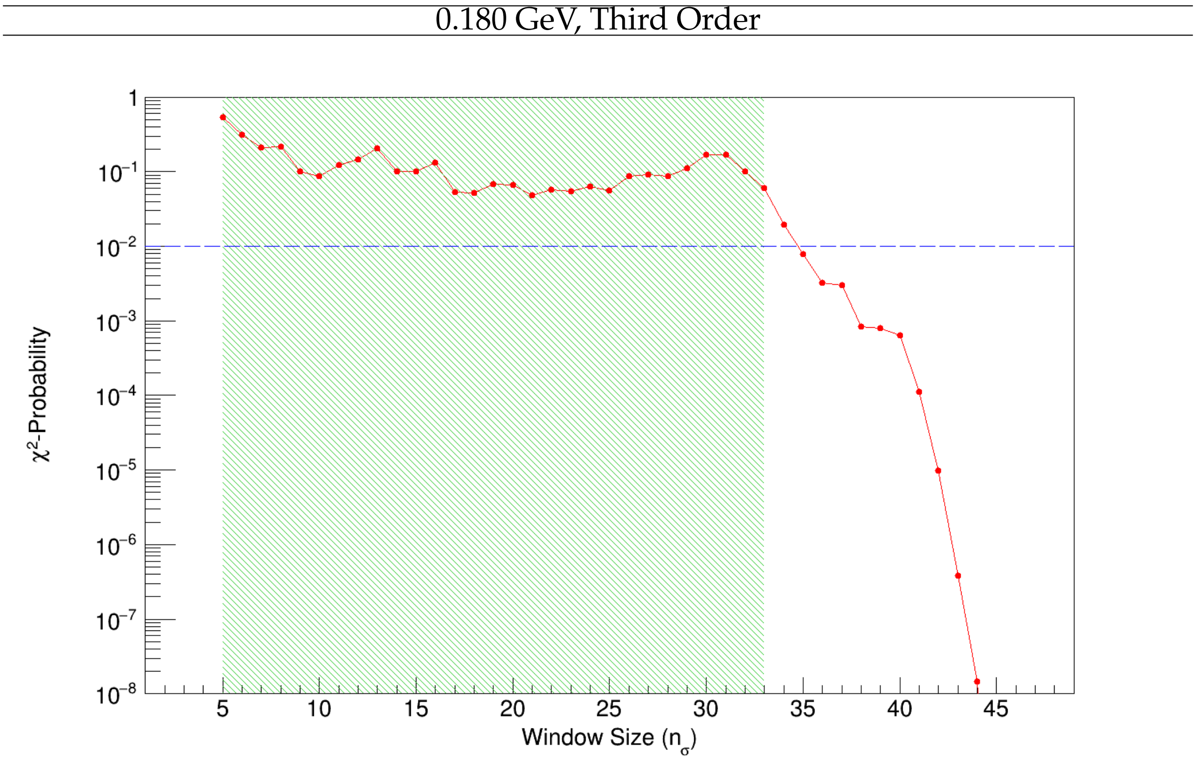

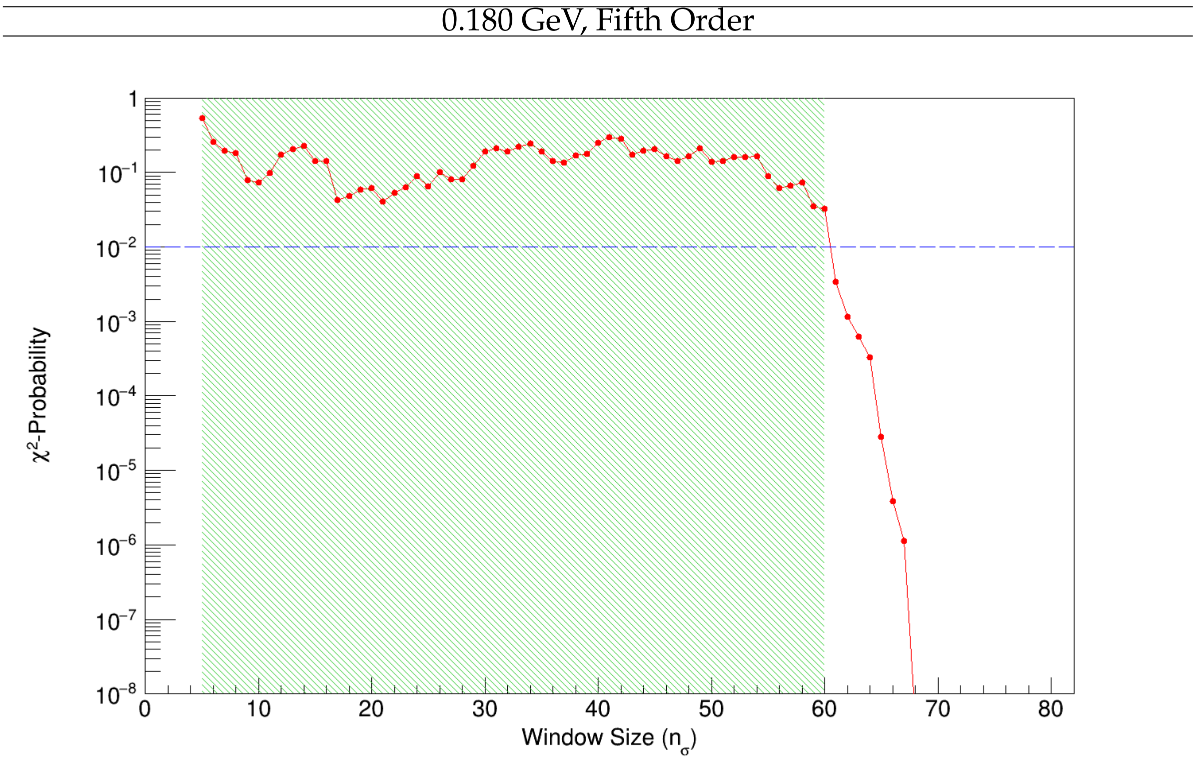

Figure 5.4: Plots of the background χ^2-probability for a mass hypothesis of 0.18 GeV, over several window sizes for both third order (top plot) and fifth order (bottom plot) background models ($f_{bg} = 10^{L_N(m_{e^+e^-}|\vec{t})}$). The blue, dashed line indicates acceptance criteria for background χ^2-probability (>10^{-2}), the green shaded area shows the region of window sizes which pass conditions (on pull and background χ^2-probability).

0.180 GeV, Third Order

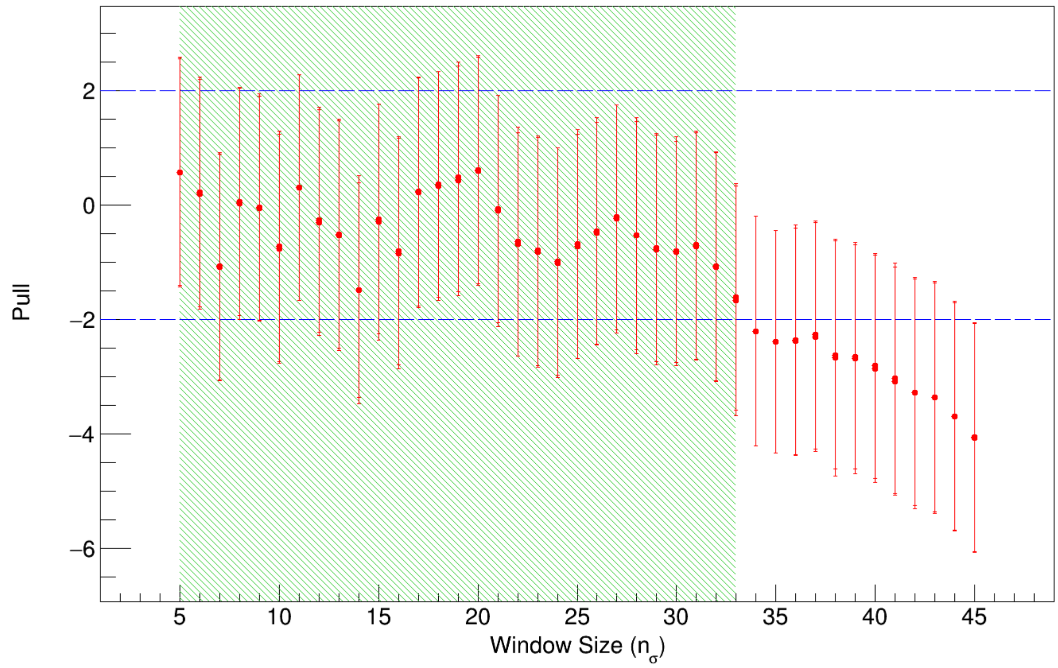

0.180 GeV, Fifth Order

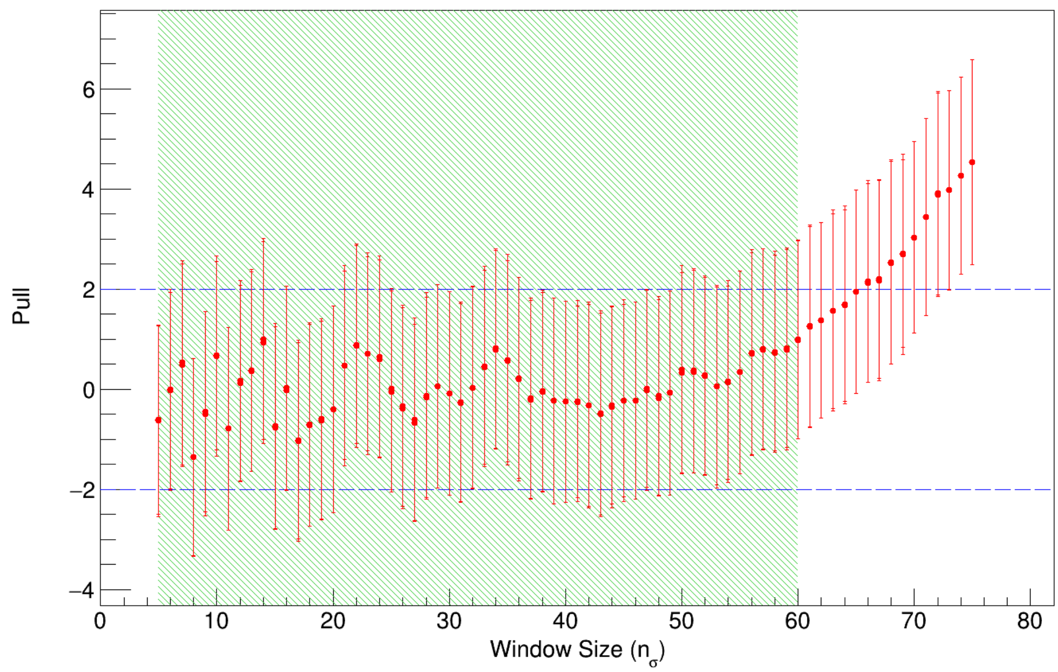

Figure 5.5: Plots of the pull for a mass hypothesis of 0.18 GeV, over several window sizes for both third order (top plot) and fifth order (bottom plot) background models ($f_{bg} = 10^{L_N(m_{e^+e^-}|\vec{t})}$). Blue, dashed lines indicate acceptance criteria for pull (0 ± 2), the green shaded area shows the region of window sizes which pass conditions (on pull and background χ^2-probability).

$n_\sigma = 9$, upper limits in signal events, μ

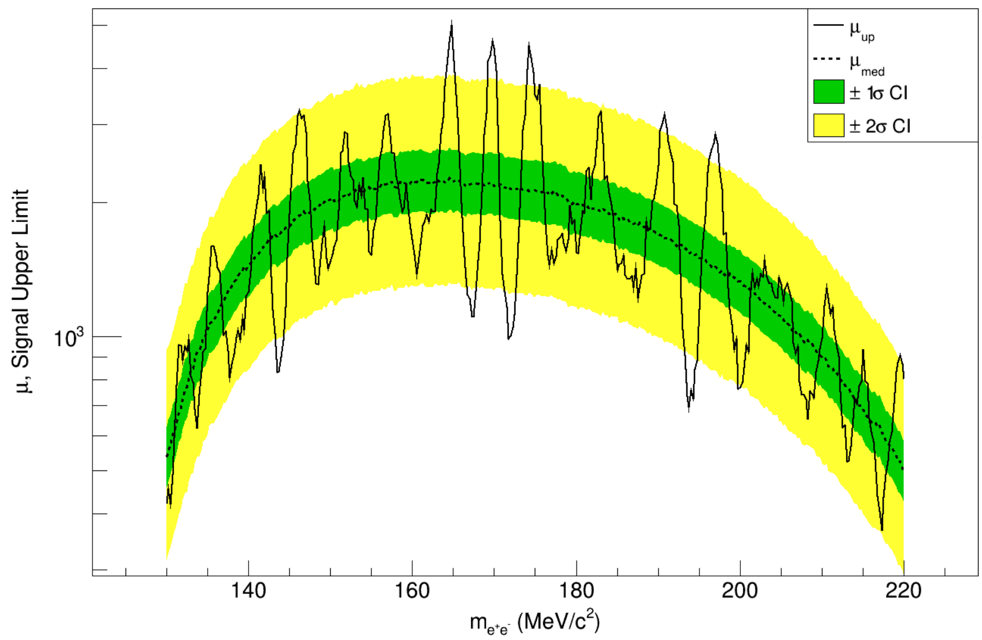

$n_\sigma = 9$, lower limits in ϵ^2

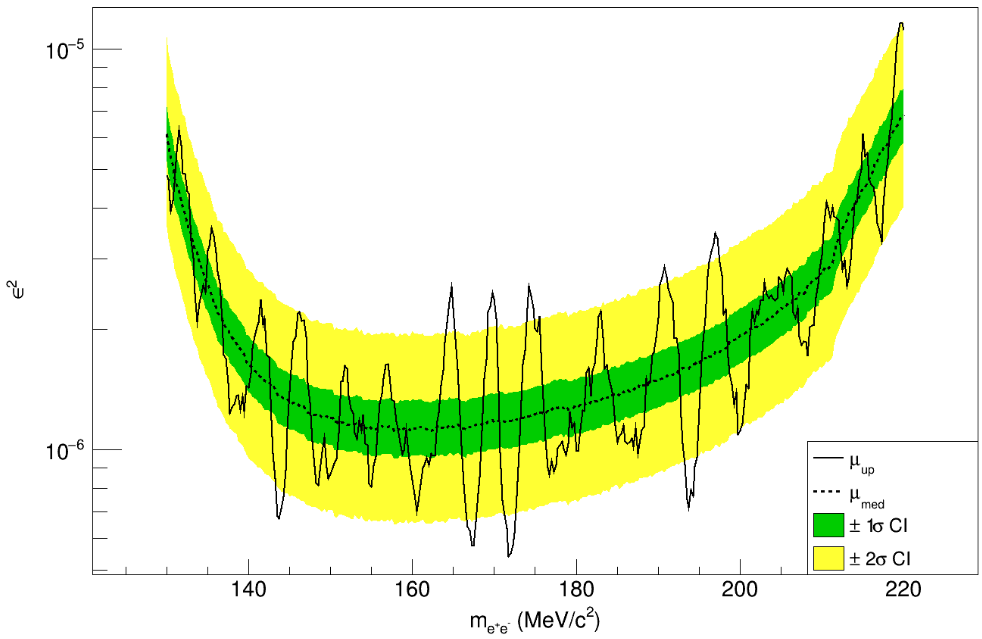

Figure 5.6: Limits in the number of signal events, μ, (top plot) and ϵ^2 (bottom plot), with a window size of $n_\sigma = 9$ and $N_{bg} = 3$ (blinded search). The solid, black line displays μ_{up} (or derived ϵ^2), the upper (or lower) limit. The dashed, black line displays the median value, μ_{med} (or derived ϵ^2), obtained from pseudo-experiments, with the green and yellow bands representing the $\pm1\sigma$ and $\pm2\sigma$ CIs respectively.

0.180 GeV, upper limits in signal events, μ

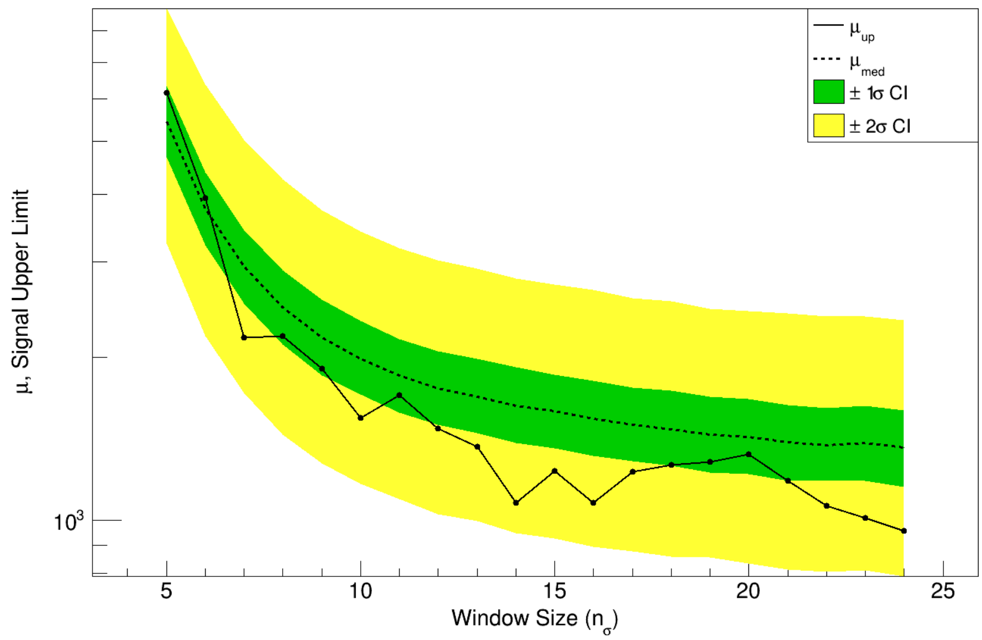

0.180 GeV, upper limits in ϵ^2

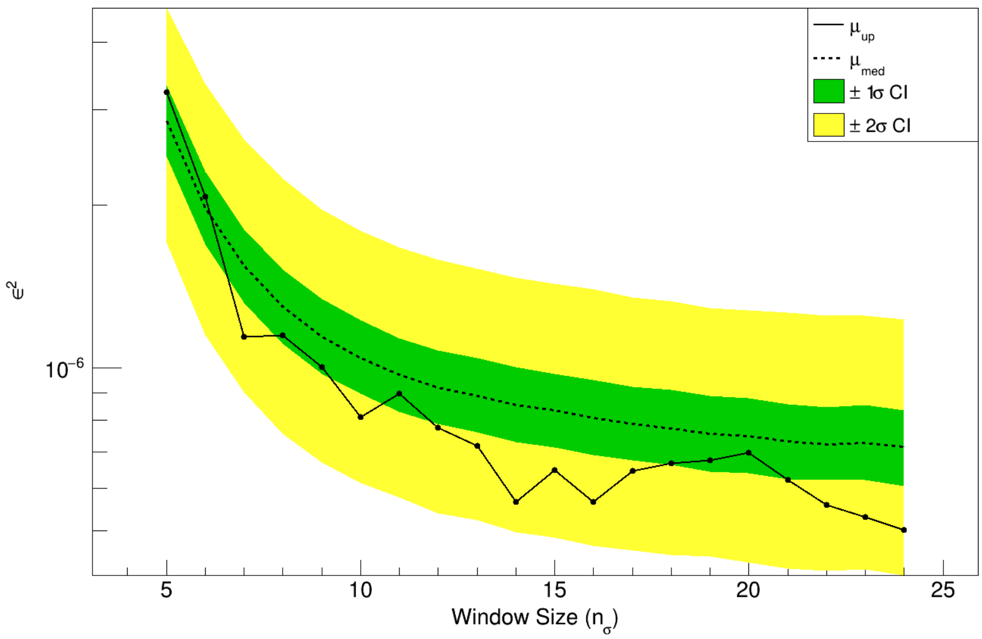

Figure 5.7: Limits in the number of signal events, μ, (top plot) and ϵ^2 (bottom plot), at $m_{e^+e^-} = 0.180$ GeV over window sizes $n_\sigma = (9, 24)$ with $N_{bg} = 3$ (blinded search). The solid, black line displays μ_{up} (or derived ϵ^2), the upper (or lower) limit. The dashed, black line displays the median value, μ_{med} (or derived ϵ^2), obtained from pseudo-experiments, with the green and yellow bands representing the $\pm 1\sigma$ and $\pm 2\sigma$ CIs respectively.

5.7 Final Results for Blinded Search

The final model choices, as in equation 5.46, were used to perform a peak search on the blinded invariant mass distribution. The mass hypotheses were separated by 0.25 MeV and covered the range 120 MeV $\leq m_H \leq$ 230 MeV.

The first stage of the peak search was to search for an A′ resonance, the 'discovery' stage as set out in section 5.4.2. The resulting p-values for discovery can be seen in figure 5.8. No significant p-value is obtained from the blinded search. Note that the p-values for figure 5.8 are the local p-values, with the thresholds for significance converted into global equivalents with the LEE correction (as described in section 5.4.4).

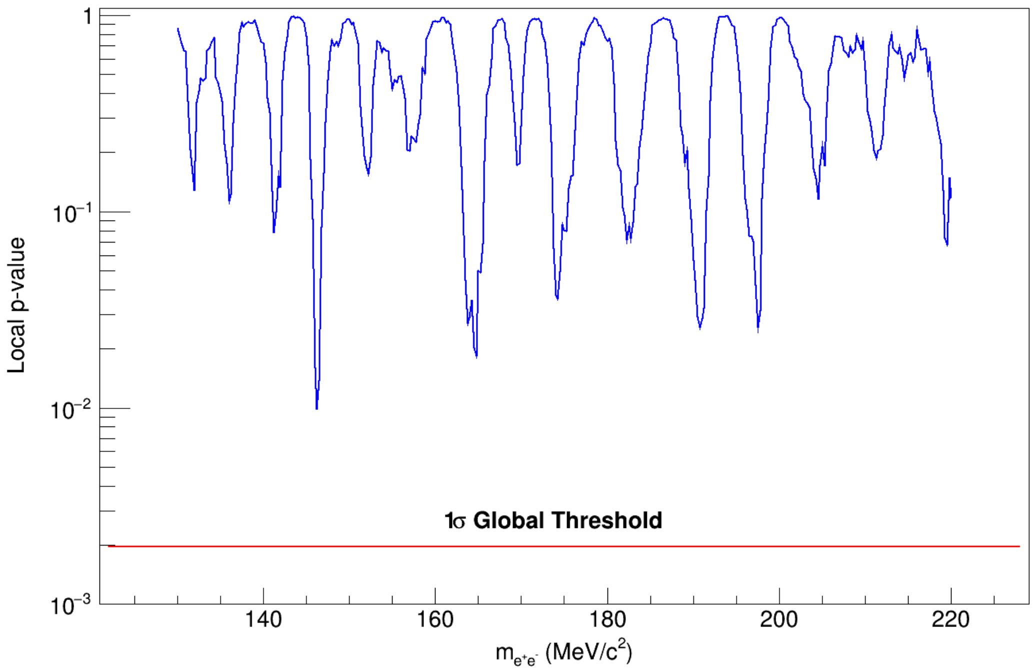

Figure 5.8: Local p-values from blinded search for A′ resonance. The red line shows the 1σ global threshold. Mass hypotheses are separated by 0.25 MeV, and tested over 120 MeV $\leq m_H \leq$ 230 MeV.

The second stage of the peak search was to establish upper limits for the number of signal events (as described in section 5.4.4) which can then be translated to limits in ϵ^2 (detailed in section 5.5). For the final model choices for the blinded search figure 5.9 gives the upper limits in signal events, μ_{up} and the subsequent value of ϵ^2. Figure 5.10 shows the final exclusion plot in $P(m_{A'}, \epsilon^2)$ for the blinded search, with results for other experiments displayed for reference.

Final $C(N_{bg}, n_\sigma)$, upper limits in signal events, μ

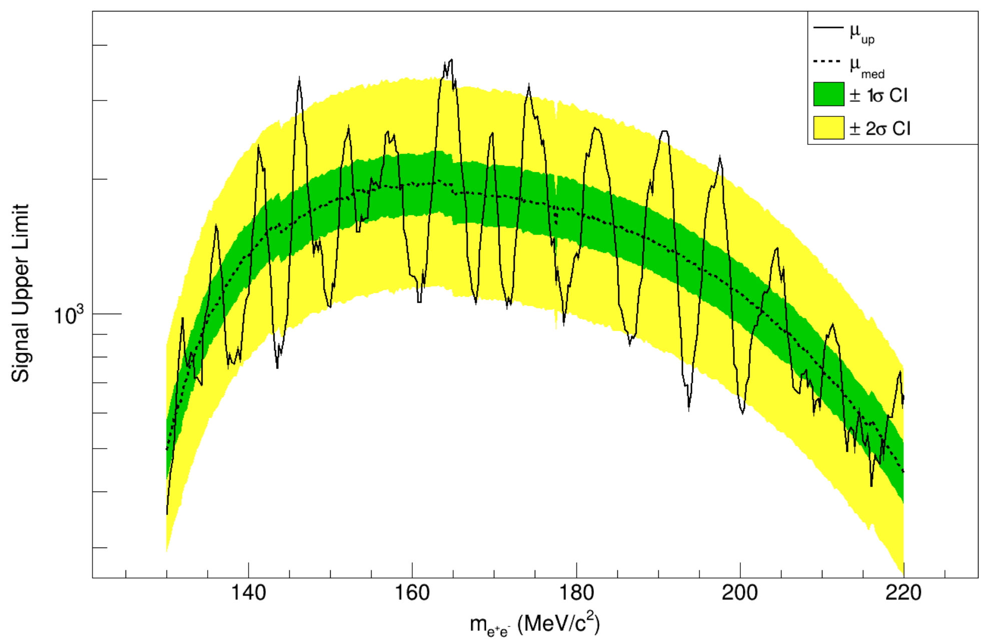

Final $C(N_{bg}, n_\sigma)$, upper limits in ϵ^2

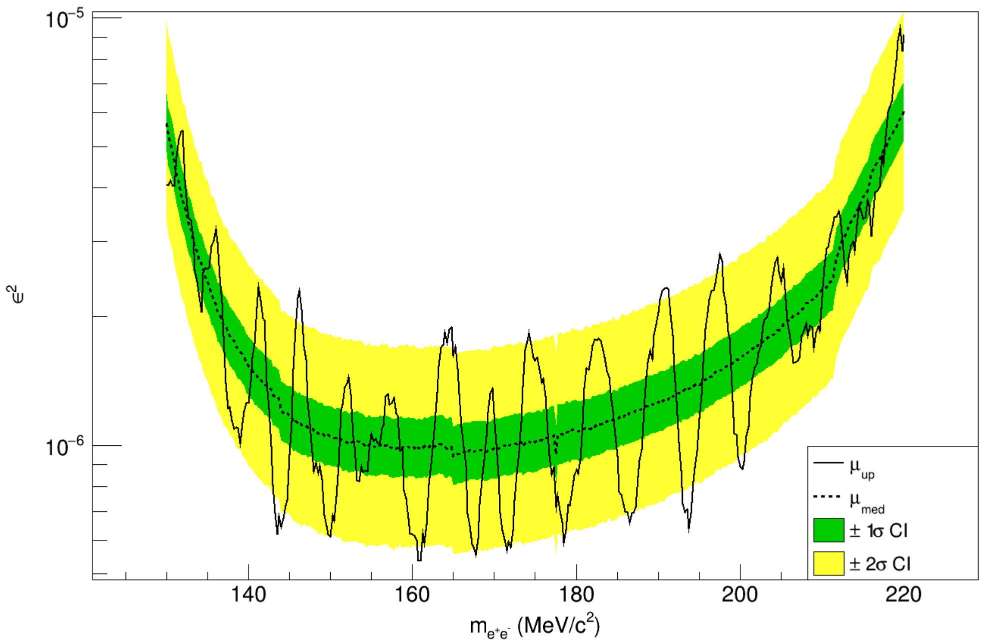

Figure 5.9: Limits in the number of signal events, μ, (top plot) and ϵ^2 (bottom plot), with final model parameters $C(N_{bg}, n_\sigma)$ (blinded search). The solid, black line displays μ_{up} (or derived ϵ^2), the upper (or lower) limit. The dashed, black line displays the median value, μ_{med} (or derived ϵ^2), obtained from pseudo-experiments, with the green and yellow bands representing the $\pm 1\sigma$ and $\pm 2\sigma$ CIs respectively.

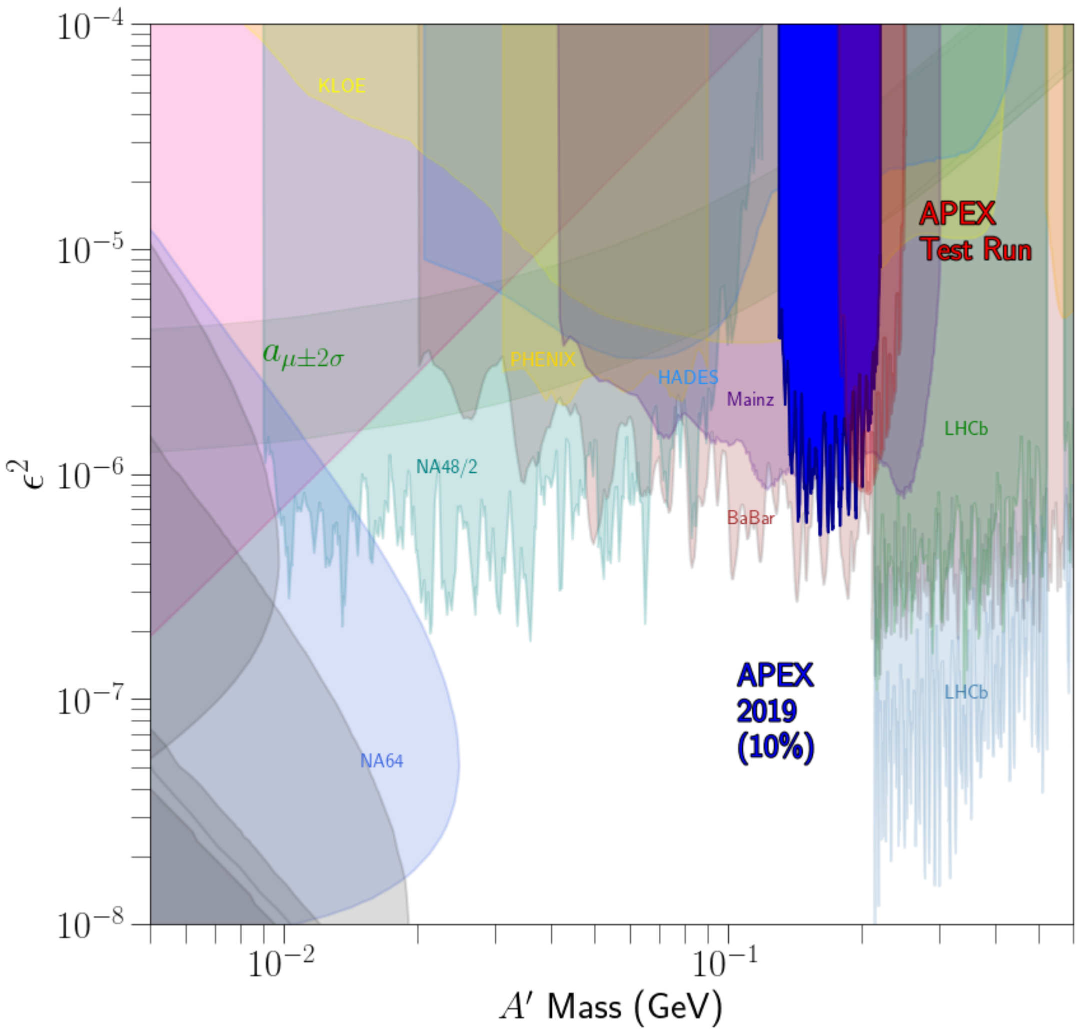

Figure 5.10: Exclusion plot in ϵ^2 versus $m_{A'}$. The results for the blinded (10%) search on APEX 2019 data are shown in solid blue, the results from the APEX 2010 test run are shown in red. Exclusion zones established by other experiments are also displayed.

Chapter 6

Conclusion

An APEX production run period took place in 2019, in Hall A of Jefferson Lab with the e^+e^- final state recorded by the HRSs. Ten tungsten foil targets were used with a 2.138 GeV electron beam. In order to obtain a final e^+e^- invariant mass spectrum, and to optimise the invariant mass resolution a series of calibration and analysis steps were carried out. Standard detector calibrations were performed after which the PID, coincidence timing, beam position measurement, VDC tracking and magnetic optics reconstruction were all examined and optimised for the experiment. This resulted in a final event sample of $\sim$52 million e^+e^- pairs.

The preparations for the experimental run and the subsequent data taking formed the initial work contributed to this thesis. The data-taking proceeded relatively smoothly, with some minor delays at the beginning of the run period that are expected when altering the experimental set-up in Hall A (the septum was installed, and HRS angles altered accordingly). Optics runs used for spectrometer optics optimisation, and pedestal runs for detector calibration were taken. A harp scan was performed to calibrate the beam position. For production runs, the total amount of charge on target was 25 C. The LHRS VDC was found to have low efficiency during the run period due to an unconnected control cable which resulted in the VDC HV tripping. This was fixed and the LHRS VDC efficiency was restored for the remainder of the run period.

The analysis of the experiment then progressed in stages. The beam position was calibrated during the run period, after which the beam raster could then be calibrated. Standard detector calibrations (gain and pedestal setting) were carried out for the various detector systems for both HRS arms. The PID cuts were then determined for APEX data, adapting existing PID methods for the HRSs. The analysis for the coincidence timing, VDC tracking and optics reconstruction required more extensive work for the APEX analysis.

Coincidence timing resolution was important to reduce the accidental fraction of the final event sample. Different methods for determining timing offsets for each S2 paddle and path length corrections were considered. Optimal timing resolution, $\sigma_{ct} \sim 0.62$ ns, was achieved with the 'adjacent paddle' method for timing offsets, along with corrections for jitter and path length from θ_{FP} and ϕ_{FP}.

The analysis of the VDC was modified to account for high event rates in the LHRS for APEX running. The VDC algorithm was altered to include a timing offset when forming hit clusters in VDC planes, used to account for accidental tracks bearing no time relation to the trigger. The differences in timing offsets between VDC planes were used as a component of a goodness of fit measure, along with spatial projections between VDC chambers, to rank potential tracks. An updated procedure used multiple cuts to ensure reliable track construction with high rates.

The spectrometer optics were crucial for the APEX analysis, both for the contribution to the invariant mass resolution and for forming cuts to reduce the accidental fraction. Optimisation of the matrix elements corresponding to the angular and vertex reconstruction were first carried out on optics data taken with the vertical wire targets before moving on to optics runs taken with the optics targets. This calibration was time-consuming, and took multiple iterations to achieve the final obtained optics matrices. The final vertex and momentum resolutions were determined from production data. Cuts based on the sum of the momentum deviations from both arms (which has an upper limit for true coincidences) and the difference in z vertex between arms were determined. These cuts served to reduce the accidental fraction.

After applying the final determined cuts a blinded peak search was carried out on 10% of the final e^+e^- invariant mass data in the mass range of ~130-220 MeV. The purpose of this was to optimise the choice of background parameters used in the resonance search, without biasing a final measurement. The angular and momentum resolutions obtained were used to determine the invariant mass resolution as function of invariant mass. An exponential Legendre polynomial was employed to describe the invariant mass distribution in a fixed mass window around the mass hypothesis, with the A′ resonance modelled as Gaussian peak (with width given by the invariant mass resolution). At each mass hypothesis, seperated by 0.25 MeV, the pull and χ^2-probability of the background fit were tested for third and fifth order backgrounds and multiple mass window sizes. The final choices for mass window size and background order were made requiring conditions for the pull and background χ^2-probability to be met (and considering changes when moving to 100% of the data), whilst trying to maximise the reach of the measurement.

The p-values obtained for discovery had to be modified to account for the Look Elsewhere Effect. The blinded search found no evidence for the dark photon, in the mass range ∼130-220 MeV. Upper limits in the number of signal events were then established across the mass range. To translate this into a lower limit on ϵ^2, the radiative fraction had to be determined. Simulations were used to obtain contributions from radiative and Bethe-Heitler tridents and e^+e^- photoproduction as a function of invariant mass. The accidental fraction was determined from experimental data. The radiative fraction was then parameterised as a function of invariant mass. Finally, an exclusion zone in $P(m_{A'}, \epsilon^2)$ was established, down to values of $\epsilon^2 \simeq 6 \times 10^{-7}$.

6.1 Outlook

Future work on the APEX 2019 analysis will move towards performing the peak search for the 100%, unblinded spectrum. Possible improvements made to the spectrometer optics (discussed in section 4.5.6) could affect the radiative fraction or the invariant mass resolution (by improving the angular or momentum resolutions). This would need to be taken into account by updating either or both quantities, for the peak search.

Further work will investigate and incorporate systematics in the final result. The 'ratio method' used for calculating ϵ^2 from the upper limit in signal events minimises systematic errors from acceptance and trigger effects by normalising A' signal events to QED trident events [1]. Sources of systematic error that will be considered are from fiducial cut levels, the invariant mass resolution and the radiative fraction. Different fiducial cut levels will be tested to determine the effect on p-values and signal upper limits (which will translate to ϵ^2). The determined invariant mass resolution has an uncertainty dependent on the invariant mass (as can be seen in figure 5.2). The invariant mass resolution will be varied according to its uncertainty over many peak searches to determine the effects on resulting p-values and signal upper limits (and hence ϵ^2). The radiative fraction will have a systematic deriving from the uncertainty in the cross-section of each contributing process, which can be determined through simulation. This will not affect the peak search but will add a systematic to ϵ^2.

Once these stages are completed a final peak search on 100% of the final invariant mass data will be performed. The median limit in ϵ^2 (denoted as μ_{med} in figure 5.9 for the blinded search) can be expected to decrease by a factor of $\sqrt{10}$ for the unblinded search. This comes from taking the null hypothesis of no signal events ($S = 0$). The number of background events, B, is then proportional to the overall number of recorded events, N: $B \propto N$. With a large N, the number of events in a bin can be taken to be Gaussian distributed and from this the $X\sigma$ limit on the number of signal events is given by $S = X\sqrt{B} \propto X\sqrt{N}$ (as used for projected 2σ limits in the APEX proposal [22]). Unblinding the peak search results in $N_u = 10N_b \implies B_u = 10B_b, \quad S_u = \sqrt{10}S_b$ (where the subscripts u and b denote unblinded and blinded respectively). Translating this to a limit in ϵ^2 (as in equation 5.43) thus gives an expected decrease (improvement) by a factor of $\sqrt{10}$ in the median ϵ^2 limit. This would give median limits down to $\epsilon^2 \sim 3 \times 10^{-7}$ for the unblinded search and thus allow APEX to probe new parameter space in $P(m_{A'}, \epsilon^2)$.

Bibliography

[1] S. Abrahamyan, et al. Search for a New Gauge Boson in Electron-Nucleus Fixed-Target Scattering by the APEX Experiment. *Phys. Rev. Lett.*, 2011. 107(19):191804.

[2] HPS collaboration et al. The HPS Experiment at JLab. *EPJ Web Conf.*, 2017. 142:01011.

[3] R. H. Parker, et al. Measurement of the Fine-Structure Constant as a Test of the Standard Model. *Science*, 2018. 360(6385):191–195.

[4] L. Morel, et al. Determination of the Fine-Structure Constant with an Accuracy of 81 Parts per Trillion. *Nature*, 2020. 588(7836):61–65.

[5] D. Hanneke, et al. New Measurement of the Electron Magnetic Moment and the Fine Structure Constant. *Phys. Rev. Lett.*, 2008. 100(12):120801.

[6] F. Zwicky. Die Rotverschiebung von Extragalaktischen Nebeln. *Helv. Phys. Acta*, 1933. 6:110–127.

[7] F. Iocco, et al. Evidence for Dark Matter in the Inner Milky Way. *Nature Physics*, 2015. 11(3):245–248.

[8] T. S. van Albada, et al. Distribution of Dark Matter in the Spiral Galaxy NGC 3198. *The Astrophysical Journal*, 1985. 295:305–313.

[9] J. E. Gunn et al. On the Infall of Matter into Clusters of Galaxies and Some Effects on Their Evolution. *Astrophys. J.*, 1972. 176:1–19.

[10] M. Markevitch, et al. A High Resolution Picture of the Intracluster Gas. *arXiv:astro-ph/0208208*, 2002.

[11] M. Markevitch. Chandra Observation of the Most Interesting Cluster in the Universe. *arXiv:astro-ph/0511345*, 2005.

[12] D. Clowe, et al. A Direct Empirical Proof of the Existence of Dark Matter. *The Astrophysical Journal*, 2006. 648(2):L109–L113.

[13] 1E 0657-56 with Scale Bar. NASA/CXC/CfA. https://chandra.harvard.edu/photo/2006/1e0657/more.html, 2006.

[14] N. Jarosik, et al. Seven-Year Wilkinson Microwave Anisotropy Probe (WMAP) Observations: Sky Maps, Systematic Errors, and Basic Results. *The Astrophysical Journal Supplement Series*, 2011. 192(2):14.

[15] N. Aghanim, et al. Planck 2015 Results. I. Overview of Products and Scientific Results. *Astronomy & Astrophysics*, 2016. 594:A1.

[16] N. Aghanim, et al. Planck 2018 Results. VI. Cosmological Parameters. *Astronomy & Astrophysics*, 2020. 641:A6.

[17] M. Kamionkowski. WIMP and Axion Dark Matter. *arXiv:hep-ph/9710467*, 1997.

[18] J. Alexander et al. Dark Sectors 2016 Workshop: Community Report. 2016 .

[19] B. Holdom. Two U(1)'s and Epsilon Charge Shifts. *Phys. Lett. B*, 1986. 166:196–198.

[20] J. D. Bjorken, et al. New Fixed-Target Experiments to Search for Dark Gauge Forces. *Phys. Rev. D*, 2009. 80(7).

[21] M. Baumgart, et al. Non-Abelian Dark Sectors and Their Collider Signatures. *Journal of High Energy Physics*, 2009. 2009(04):014–014.

[22] J. D. Bjorken, et al. The A' Experiment (APEX): Search for a New Vector Boson A' Decaying to e^+e^-. *JLab proposal PR-10-009*, 2010.

[23] M. Goodsell, et al. Naturally Light Hidden Photons in LARGE Volume String Compactifications. *Journal of High Energy Physics*, 2009. 2009(11):027–027.

[24] M. Cicoli, et al. Testing String Vacua in the Lab: From a Hidden CMB to Dark Forces in Flux Compactifications. *Journal of High Energy Physics*, 2011. 2011(7):114.

[25] S. Andreas, et al. New Limits on Hidden Photons from Past Electron Beam Dumps. *Phys. Rev. D*, 2012. 86(9):095019.

[26] M. Raggi et al. Results and Perspectives in Dark Photon Physics. *Riv. Nuovo Cim.*, 2015. 38(10):449–505.

[27] E. Graverini. SHiP Sensitivity to Dark Photons. https://cds.cern.ch/record/2214092/files/ship-note-dark-photons.pdf, 2016.

[28] C. Amsler, et al. Review of Particle Physics. *Phys. Lett. B*, 2008. 667(1):1–6.

[29] H. Merkel, et al. Search for Light Massive Gauge Bosons as an Explanation of the $(g-2)_\mu$ Anomaly at MAMI. *Phys. Rev. Lett.*, 2014. 112(22):221802.

[30] P. H. Adrian, et al. Search for a Dark Photon in Electroproduced e^+e^- Pairs with the Heavy Photon Search Experiment at JLab. *Phys. Rev. D*, 2018. 98(9):091101.

[31] J. Balewski, et al. The DarkLight Experiment: A Precision Search for New Physics at Low Energies. *arXiv:1412.4717*, 2014.

[32] L. Doria, et al. Search for Light Dark Matter with the MESA Accelerator. *arXiv:1809.07168*, 2018.

[33] G. Agakishiev et al. Searching a Dark Photon with HADES. *Phys. Lett. B*, 2014. 731:265–271.

[34] J. R. Batley et al. Search for the Dark Photon in π^0 Decays. *Phys. Lett. B*, 2015. 746:178–185.

[35] B. Wojtsekhowski, et al. Searching for a New Force at VEPP-3. *arXiv:1207.5089*, 2012.

[36] M. Raggi, et al. The PADME Experiment at LNF. *EPJ Web Conf.*, 2015. 96:01025.

[37] D. Babusci, et al. Limit on the Production of a Light Vector Gauge Boson in ϕ Meson Decays with the KLOE Detector. *Phys. Lett. B*, 2013. 720(1-3):111–115.

[38] G. Mandaglio. KLOE/KLOE-2 Results and Perspectives on Dark Force Search. *PoS*, 2017. EPS-HEP2017:073.

[39] B. Aubert et al. Search for Dimuon Decays of a Light Scalar Boson in Radiative Transitions $\Upsilon \to \gamma A^0$. *Phys. Rev. Lett.*, 2009. 103(8):081803.

[40] G. De Pietro. First Data at Belle II and Dark Sector Physics. *PoS*, 2018. Beauty 2018:034.

[41] G. Inguglia. Dark Sector Physics at the Belle II Experiment. *Nuovo Cim. C*, 2020. 42(6):257.

[42] P. Ilten, et al. Dark Photons from Charm Mesons at LHCb. *Phys. Rev. D*, 2015. 92(11):115017.

[43] P. Ilten, et al. Inclusive Dark Photon Search at LHCb. *Phys. Rev. Lett.*, 2016. 116(25):251803.

[44] R. Aaij, et al. Search for Dark Photons Produced in 13 TeV pp Collisions. *Phys. Rev. Lett.*, 2018. 120(6):061801.

[45] R. Aaij, et al. Search for $A' \to \mu^+\mu^-$ Decays. *Phys. Rev. Lett.*, 2020. 124(4):041801.

[46] H. El Jarrari. SISSA : Dark Photon Searches with the ATLAS Detector at the LHC. *PoS*, 2021. LHCP2020:220.

[47] A. Sirunyan et al. Search for Dark Photons in Decays of Higgs Bosons Produced in Association with Z Bosons in Proton-Proton Collisions at $\sqrt{s} = 13$ TeV. *Journal of High Energy Physics*, 2019. 2019(10):139.

[48] A. Adare et al. Search for Dark Photons from Neutral Meson Decays in $p + p$ and d + Au Collisions at $\sqrt{s_{NN}}$ = 200 GeV. *Phys. Rev. C*, 2015. 91(3):031901.

[49] A. Bross, et al. A Search for Shortlived Particles Produced in an Electron Beam Dump. *Phys. Rev. Lett.*, 1991. 67:2942–2945.

[50] J. D. Bjorken, et al. Search for Neutral Metastable Penetrating Particles Produced in the SLAC Beam Dump. *Phys. Rev. D*, 1988. 38:3375.

[51] M. Davier et al. An Unambiguous Search for a Light Higgs Boson. *Phys. Lett. B*, 1989. 229:150–155.

[52] D. Banerjee, et al. Dark Matter Search in Missing Energy Events with NA64. *Phys. Rev. Lett.*, 2019. 123(12):121801.

[53] P. deNiverville, et al. Light New Physics in Coherent Neutrino-Nucleus Scattering Experiments. *Phys. Rev. D*, 2015. 92(9):095005.

[54] S. Alekhin, et al. A Facility to Search for Hidden Particles at the CERN SPS: The SHiP Physics Case. *Reports on Progress in Physics*, 2016. 79(12):124201.

[55] S. Gardner, et al. New Prospects in Fixed Target Searches for Dark Forces with the SeaQuest Experiment at Fermilab. *Phys. Rev. D*, 2016. 93(11):115015.

[56] R. Essig, et al. Probing Dark Forces and Light Hidden Sectors at Low-Energy e^+e^- Colliders. *Phys. Rev. D*, 2009. 80(1):015003.

[57] Y.-S. Tsai. Pair Production and Bremsstrahlung of Charged Leptons. *Reviews of Modern Physics*, 1974. 46(4):815–851.

[58] K. J. Kim et al. Improved Weizsäcker-Williams Method and Its Application to Lepton and W-Boson Pair Production. *Phys. Rev. D*, 1973. 8(9):3109–3125.

[59] Y. S. Tsai. Axion Bremsstrahlung by an Electron Beam. *Phys. Rev. D*, 1986. 34(5):1326–1331.

[60] J. D. Bjorken, et al. New Fixed-Target Experiments to Search for Dark Gauge Forces. *Phys. Rev. D*, 2009. 80(7):075018.

[61] R. Essig, et al. An Electron Fixed Target Experiment to Search for a New Vector Boson A' Decaying to e^+e^-. *Journal of High Energy Physics*, 2011. 2011(2):1–35.

[62] F. Gross. Making the Case for Jefferson Lab. *Journal of Physics: Conference Series*, 2011. 299:012001.

[63] J. Dudek, et al. Physics Opportunities with the 12 GeV Upgrade at Jefferson Lab. *The European Physical Journal A*, 2012. 48(12):187.

[64] Jefferson Lab. CEBAF at 12 GeV Schematic. https://www.flickr.com/photos/jeffersonlab/12599705145/, 2014.

[65] J. Alcorn, et al. Basic Instrumentation for Hall A at Jefferson Lab. *Nucl. Instrum. Meth. A*, 2004. 522:294–346.

[66] P. Zhu et al. Beam Position Reconstruction for g_2^p Experiment in Hall A at Jefferson Lab. *Nucl. Instrum. Meth. A*, 2016. 808:1–10.

[67] T. Powers, et al. Design, Commissioning and Operational Results of Wide Dynamic Range BPM Switched Electrode Electronics. *AIP Conference Proceedings*, 1997. 390(1):257–265.

[68] E. L. Jensen. *A Search for a New Gauge Boson A'*. Ph.D. thesis, College of William & Mary, 2013.

[69] K. G. Fissum, et al. Vertical Drift Chambers for the Hall A High-Resolution Spectrometers at Jefferson Lab. *Nucl. Instrum. Meth. A*, 2001. 474:108–131.

[70] M. Iodice, et al. The CO_2 Gas Cherenkov Detectors for the Jefferson Lab Hall-A Spectrometers. *Nucl. Instrum. Meth. A*, 1998. 411:223–237.

[71] N. Liyanage. Optics Calibration of the Hall A High Resolution Spectrometers Using the New Optimizer. Technical Report JLAB-TN-02-012, 2002.

[72] C. Gu. *The Spin Structure of the Proton at Low Q^2: A Measurement of the Structure Function g_2^p*. Ph.D. thesis, University of Virginia, 2016.

[73] CODA. https://coda.jlab.org/drupal/.

[74] EPICS. https://epics.anl.gov/.

[75] V. Sulkosky. Data Acquisition for the Hall A High Resolution Spectrometers During 12 GeV. 2014 .

[76] E. Jastrzembski. Trigger Supervisor. Jefferson Lab - Data Acquisition Group, 2009 .

[77] O. Hansen. Hall A Analyzer. https://redmine.jlab.org/projects/podd/wiki/Documentation.

[78] R. Brun et al. ROOT: An Object Oriented Data Analysis Framework. *Nucl. Instrum. Meth. A*, 1997. 389:81–86.

[79] M. Hatlo, et al. Developments of Mathematical Software Libraries for the LHC Experiments. *IEEE Trans.Nucl.Sci.*, 2005. 52:2818–2822.

[80] T. T. Kutz. *Deep Inelastic Scattering from A = 3 Nuclei: Nucleon Structure and the EMC Effect*. Ph.D. thesis, Stony Brook University, 2020.

[81] B. B. A. . Schmookler. *Nucleon Structure and Its Modification in Nuclei*. Ph.D. thesis, Massachusetts Institute of Technology, 2018.

[82] L. Ou. *Precision Measurements of Electron-Proton Elastic Scattering Cross Sections at Large* Q^2. Ph.D. thesis, Massachusetts Institute of Technology, 2019.

[83] R. H. Wechsler. *Drift-Time Properties of CEBAF Hall A Vertical Drift Chambers*. B.S., Massachusetts Institute of Technology, 1996.

[84] D. J. Linthorne. *On the Hunt for Dark Photons : Improving the Tracking of Vertical Drift Chambers*. B.S, Halifax, N.S. : Saint Mary's University, 2016.

[85] P. R. Bevington, et al. Data Reduction and Error Analysis for the Physical Sciences. *Computers in Physics*, 1993. 7(4):415–416.

[86] VDC Relay Box Control (Left HRS) | Jefferson Lab Electronic Logbook. https://logbooks.jlab.org/entry/3663545, 2019.

[87] C. Gu. Spectrometer Optics Study for E08-027. Technical Report JLAB-TN-16-018, 2016.

[88] Y. Qiang. *Search for Pentaquark Partners* Θ^{++}, Σ^0 *and* N^0 *in* $H(e,e'K(\pi))X$ *Reactions at Jefferson Lab Hall A*. Ph.D. thesis, Massachusetts Institute of Technology, 2007.

[89] S. Agostinelli et al. GEANT4–a Simulation Toolkit. *Nucl. Instrum. Meth. A*, 2003. 506:250–303.

[90] Heavy Photon Search Toolkit for Reconstruction. https://github.com/JeffersonLab/hpstr, 2022.

[91] G. Cowan, et al. Asymptotic Formulae for Likelihood-Based Tests of New Physics. *The European Physical Journal C*, 2011. 71(2):1554.

[92] J. Neyman et al. On the Problem of the Most Efficient Tests of Statistical Hypotheses. *Phil. Trans. Roy. Soc. Lond. A*, 1933. 231(694-706):289–337.

[93] G. Aad, et al. Combined Search for the Standard Model Higgs Boson in pp Collisions at $\sqrt{s} = 7$ TeV with the ATLAS Detector. *Phys. Rev. D*, 2012. 86(3):032003.

[94] L. Lyons. Discovering the Significance of 5 Sigma. *arXiv:1310.1284*, 2013.

[95] A. Wald. Tests of Statistical Hypotheses Concerning Several Parameters When the Number of Observations Is Large. *Transactions of the American Mathematical Society*, 1943. 54(3):426–482.

[96] S. S. Wilks. The Large-Sample Distribution of the Likelihood Ratio for Testing Composite Hypotheses. *Annals Math. Statist.*, 1938. 9(1):60–62.

[97] E. Gross et al. Trial Factors for the Look Elsewhere Effect in High Energy Physics. *The European Physical Journal C*, 2010. 70(1-2):525–530.

[98] G. Cowan, et al. Power-Constrained Limits. *arXiv:1105.3166*, 2011.

[99] A. L. Read. Modified Frequentist Analysis of Search Results (The CL(s) Method). IN *Workshop on Confidence Limits*. 2000 pages 81–101.

[100] A. L. Read. Presentation of Search Results: The CL(s) Technique. *J. Phys. G*, 2002. 28:2693–2704.

[101] D. Curtin, et al. Illuminating Dark Photons with High-Energy Colliders. *Journal of High Energy Physics*, 2015. 2015(2):157.

[102] K. Olive. Review of Particle Physics. *Chinese Physics C*, 2014. 38(9):090001.

[103] J. Alwall, et al. MadGraph 5 : Going Beyond. *Journal of High Energy Physics*, 2011. 06:128.

[104] A. Roodman. Blind Analysis in Particle Physics. *eConf*, 2003. C030908:TUIT001.

[105] S. McCarty. *Search for an A' Resonance in the Heavy Photon Search 2.3 GeV Data Set*. Ph.D. thesis, University of New Hampshire, Durham, 2020.

List of figures

List of tables